Demonstration of a New and Innovative Ozone Lidar's Capability to Measure Vertical Profiles of Ozone Concentration and Aerosol in the Lower Troposphere

Final Report

Contract No. 92-328

Prepared for:

California Air Resources Board
Research Division
2020 L Street
Sacramento, California 95814

Prepared by:

Yanzeng Zhao, R. Michael Hardesty and John E. Gaynor

Department of Commerce
National Oceanic and Atmospheric Administration
Environmental Technology Laboratory
Atmospheric Lidar Division
325 Broadway
Boulder, Colorado 80303

December 1994

Disclaimer

The statements and conclusions in this report are those of the NOAA/ERL/ETL and not necessarily those of the California Air Resources Board. The mention of commercial products, their source, and their use in connection with material reported herein is not to be construed as actual or implied endorsement of such products.

Acknowledgements

Mr. James N. Howell, electronics engineer, was an important member of the crew in the Davis intercomparison experiment. He participated in the remodification of the sea-container, hardware preparation, monitoring site selection, packing and shipping, setting up the ozone lidar on the site, and assisted in trouble-shooting, re-alignment, horizontal calibrations and vertical observations of the lidar. After the Davis experiment, he made significant efforts to eliminate laser spikes in the vertical observations and to strengthen the lidar supporting system. He also participated in the site selection and hardware preparation for the *Los Angeles Atmospheric Free Radical Study* experiment in Claremont. Mrs. Ann M. Weickmann, computer analyst, and Mr. Ronald A. Richter, computer engineer, developed the data-taking program. Ann was also one of the crew in the Davis experiment and improved the data-taking program. Mr. Richard E. Cupp, contracting lidar engineer (a physicist prior to his retirement from NOAA), joined the Los Angeles experiment. He participated in the preparation of the hardware, packed and shipped the lidar, and set up the lidar at the site. He also assisted lidar trouble-shooting, realignment, calibration, and operation. Mr. Cupp's findings and suggestions resulted in significant improvements to the mechanical stability of the lidar and thus greatly improved the quality of the lidar data. Mrs. Judy Schroeder, former mathematician of NOAA, was contracted as the airplane spotter to address the eye-safety concern during lidar operation. She also assisted with refinements to the lidar data-taking software. Mr. Ronald J. Willis, professional research assistant of the Cooperative Institute for Research in Environmental Sciences (CIRES), expended considerable effort remodifying the sea-container. Mr. Tom Glaess, student assistant, developed graphics programs for checking raw data and displaying the results from data processing. Mr. Hutch Johnson, student assistant, processed the surface ozone data collected at Claremont, and helped with the sea-container remodification. Mr. Brian Tompkins, student assistant, developed graphics programs that display time-height charts of the data collected at Claremont, and the three-dimensional airplane trajectories in the Davis experiment.

Mr. Spencer Ung, graduate student working for the California Air Resources Board (CARB), launched pilot balloons to determine winds aloft during the Davis experiment.

The Mobile Profiler System (MPS) participated in the Los Angeles experiment. The meteorological data collected by MPS crew (headed by Dr. B. L. Weber of ETL's System Demonstration and Integration Division) contributed greatly to the analysis of the ozone lidar data. Mr. D. E. Wolfe, meteorologist, from the same division of ETL, also contributed significantly to the effort.

The valuable contributions of the technical team mentioned above are gratefully acknowledged.

This report was submitted in fulfillment of Contract #92-328 entitled "Demonstration of a New and Innovative Ozone Lidar's Capability to Measure Vertical Profiles of Ozone Concentration and Aerosol in the Lower Troposphere " by the National Oceanic and Atmospheric Administration's Environmental Technology Laboratory under the partial sponsorship of the California Air Resources Board. We are grateful to CARB personnel, especially Bart Croes, Leon Dolislager, Lowell Ashbough, and Ash Lashgari, for their constant help and encouragement. Special thanks is given to Leon for his valuable help in preparing this final report; his critical review of the manuscript and many helpful suggestions made the report easier to read. Work was completed as of December 28, 1994.

ABSTRACT

This report describes the ozone lidar experiments conducted by NOAA's Environmental Technology Laboratory (ETL) in California in 1993. These experiments were sponsored by the California Air Resources Board. The main objectives of the experiments were: (1) to verify the capability of the ETL ozone lidar for remotely sensing ozone and aerosol profiles in the lower troposphere, (2) to test the integrity of the lidar system and the mobile laboratory for further system improvements, (3) to improve the data retrieval algorithm and processing techniques for better accuracy of ozone observations, and (4) to test the performance of this lidar in a very polluted environment like the Los Angeles air basin, and obtain first-hand information about ozone and aerosol vertical distribution in this region. The two experiments using NOAA's lidar demonstrate that the ozone lidar can be a powerful tool for air quality monitoring and research.

The intercomparison experiment in Davis showed that the lidar and airborne DASIBI measurements of ozone mixing ratio agreed with each other within 10 parts per billion (ppb) from near the surface up to 3 km in most cases. This good agreement occurred even though the lidar was installed in a mobile laboratory just prior to its shipment. This late installation prevented any significant test of the lidar's performance in its new environment (thus some hardware problems were initially found during the field experiments and later during the data processing; the problems were corrected through data processing).

The experiment in Los Angeles (Claremont) included the day with the highest ozone concentration of the year. The lidar observations revealed large amounts of ozone trapped in the marine boundary layer below 400 m during the high ozone episode. The polluted air mass arrived at the site like a front, with a sudden increase in concentrations at all heights in the boundary layer. Aerosol profiles revealed two layers of aerosol-laden air (the boundary layer and the layer from about 1 km to 4.5 km) separated by a thin layer of clean air just above the

top of an inversion. The lidar provided unique information on the vertical distribution of the pollution and allowed data analysts to better interpret the processes involved.

TABLE OF CONTENTS

LIST OF FIGURES

LIST OF APPENDICES

1. INTRODUCTION

Lidar systems measuring ozone concentration profiles (and, when combined with a radar wind profiler system or a Doppler lidar system, flux profiles) in the lower troposphere can make significant contributions to the understanding of regional air quality and chemical/transport processes involved. At the NOAA/ERL/Environmental Technology Laboratory (ETL), formerly Wave Propagation Laboratory (WPL), a transportable differential absorption lidar (DIAL) for ozone and aerosol measurements has been developed, tested, and employed in two field experiments[1-4] sponsored by the California Air Resources Board. This ozone lidar is specifically designed for measuring ozone in the boundary layer and the lower free troposphere. It has unique features of compact size, high efficiency, high range resolution (varying from about 50 meters (m) at lower boundary layer, to 200-300 m at 3 kilometers (km) altitude above ground level), and range coverage from near surface to about 3 km. The maximum detection range depends on the amount of ozone along the observation path.

The first field campaign was an intercomparison experiment of ozone measurements by the ETL ozone lidar and by a DASIBI UV ozone analyzer on-board a Cessna 172 airplane operated by staff of the University of California - Davis. The experiment was conducted between July 9 and July 23, 1993, near Davis, California. The objectives of the experiment were: (1) to verify the capability of the ETL ozone lidar for remotely sensing ozone distributions (as well as aerosol distributions) in the lower troposphere, and to evaluate the accuracy of the ozone lidar measurements, and (2) to test the integrity of the lidar system and the mobile laboratory following long distance transport and to test its operation in a different field environment for the purpose of making further system improvements.

The Los Angeles Atmospheric Free Radical Study (LAFRS) (3 Sept.- 22 Sept. 1993) was co-sponsored by the US Environmental Protection Agency (EPA) and the California Air Resources Board (CARB) to study the formation of ozone in the Los Angeles basin. During the

experiment, the multi-wavelength ETL ozone lidar monitored ozone and aerosol profiles, while the Mobile Profiler System (MPS)[5-7] provided meteorological support for the air chemistry portion of the LARFS and meteorological data to support analyses of the air quality data collected. Operations were conducted in Claremont, California, located 5 km south of the San Gabriel Mountains and 20 km east of downtown Los Angeles, a major source region of ozone precursors. The experiment site was located on the eastern edge of the Los Angeles County, some 60 km from the coast.

2. THE ETL OZONE LIDAR

2.1 THE PRINCIPLE OF A DIAL SYSTEM

A DIAL system transmits laser pulses at two wavelengths in an absorption band (or around a narrow absorption line) of the gas species under measurement. The wavelength with a higher absorption coefficient, α_2, is called the "on-line" wavelength and the wavelength characterized by a lower absorption coefficient, α_1, is called the "off-line" wavelength. Range resolution of a DIAL system depends mainly on the differential absorption coefficient $\Delta\alpha$ (= α_2 - α_1) of the wavelength-pair. Thus, proper selection of a wavelength pair is important to the range resolution and the maximum detection range of a DIAL system.

Most ozone lidars use wavelength pairs in one of the ultraviolet (UV) ozone absorption bands: the Hartley band, or the Huggins band (see the figures in Appendix A). The Hartley band extends from about 200 to 300 nanometers (nm), centered at 250 nm, and has high absorption cross-sections. The Huggins band lies between about 300 nm and 350 nm, with much lower and more variable absorption cross-sections than in the Hartley band. Different wavelength pairs are chosen for different maximum detection range and different range resolution (there is a trade-off between the two specifications).

The corresponding DIAL ozone lidar equations at the two wavelengths take the form:

$$P_i(z) = C_{Ai}\frac{\eta_i(z)}{z^2}\beta_i(z)T_i^2(z), \qquad (1)$$

where the subscript i for various parameters in the equation stands for off-line (i = 1) and on-line (i = 2) wavelength, respectively; $P(z)$ is the detector-received power of the atmosphere-backscattered radiation (in watts) from range z (in m), C_A is the instrument constant (in W m^3 sr), $\eta(z)$ is

the overlap function, and $\beta(z)$ is the atmospheric volume backscattering coefficient (in m^{-1} sr^{-1}). $T^2(z)$ is the two-way atmospheric transmission, taking into account attenuation by molecular scattering, aerosol scattering, and ozone absorption,

$$T^2(z) = \exp[-2\int_0^z \sigma_m(z')dz']\exp[-2\int_0^z \sigma_a(z')dz']\exp[-2\int_0^z \alpha_{o3}\rho_{o3}(z')dz'], \quad (2)$$

where σ_m and σ_a are the extinction coefficients of molecules and aerosols, respectively; α_{o3} is the absorption coefficient of ozone, and ρ_{o3} is the ozone density.

Let $F(z) = P_1(z)/P_2(z)$, the off-line-to-on-line ratio of the lidar signals. Taking the logarithm and differentiating $ln[F(z)]$, we have

$$\frac{d}{dz}[\ln F(z)] = 2\Delta\alpha_{o3}(z)\rho_{o3}(z) + A(z), \quad (3)$$

where $\Delta\alpha_{o3}$ is the differential absorption coefficient of ozone, and

$$A(z) = \frac{d}{dz}\left\{\ln\left[\frac{\beta_1(z)}{\beta_2(z)}\right]\right\} + 2\Delta\sigma_m(z) + 2\Delta\sigma_a(z), \quad (4)$$

where $\Delta\sigma_m$ and $\Delta\sigma_a$ are respectively the differential extinction coefficients of molecules and aerosols. If the three terms in A(z) are properly estimated through aerosol data analysis, we can derive the ozone concentration ρ_{o3}

$$\rho_{o3} = \frac{\frac{dlnF(z)}{dz} - A(z)}{2\Delta\alpha_{o3}}. \quad (5)$$

In the above discussions we have assumed that $\eta(z)$ is stable, and has been accurately corrected, and the signals are free from other hardware interferences. In a real lidar system, however, the complexity of the hardware may introduce imperfections in many ways, especially

in a newly developed system. Thus the signals can be contaminated or distorted at different ranges due to different sources. It is crucial to carefully examine the signals and find out the sources of interference. Proper corrections need to be implemented in the software to obtain the desired accuracy of ozone measurements (see Section 2.5).

2.2 DESIGN CONSIDERATIONS

(1) Range resolution consideration and wavelengths and laser selection

Equation (5) shows that the ozone concentration is proportional to the first derivative (slope) of the natural logarithm of the ratio of the off-line-to-on-line signal, $ln[F(z)]$; i.e., numerical differentiation is involved in calculating ozone concentrations. For the same accuracy of the numerical differentiation, steeper slopes permit the use of a smaller differential range, Δz, and, thus, better range resolution. Because the slope is proportional to the differential absorption coefficient $\Delta\alpha_{o3}$, the range resolution of an ozone lidar is very dependent on $\Delta\alpha_{o3}$. As a result, a wavelength pair with high differential absorption coefficient has been selected in the Hartley band of ozone absorption spectrum in the UV. The on-line wavelength is 266 nm, close to the center of the Hartley band, and the off-line wavelength is 289 nm. This wavelength-pair has a two-way differential absorption coefficient of about 1.3 km^{-1} at the surface in a clean atmosphere with an ozone mixing ratio of about 30 ppb.

With such a wavelength-pair and a proper numerical filter, the ETL system can potentially measure ozone profiles with a range-resolution on the order of several tens of meters in the lower boundary layer, to about 200-300 m at 3 km, depending on the signal-to-noise ratio. Although the strong absorption of ozone at 266 nm limits the maximum detection range to about 3 km, this maximum detection height is adequate for boundary layer and lower free troposphere ozone monitoring. Both numerical simulations and field observations have shown that ozone profiles up to 3 km can be obtained under normal conditions (surface ozone mixing ratio < 150 ppb) with a multibeam transmitter (see next section). Even with extremely high surface ozone

concentrations (>300 ppb), ozone profiles up to 2 km can still be observed. The 266 and 289 nm pair is also insensitive to SO_2 and NO_2 interferences. In addition, both wavelengths are in the so-called "solar-blind" region where background solar radiation can be neglected.

Another important consideration in choosing 266 nm as the on-line wavelength is present laser technology. This wavelength is the fourth harmonic of Nd:YAG lasers. A frequency-quadrupled Nd:YAG is compact, solid-state, technically mature, and relatively inexpensive. Using an Nd:YAG laser instead of the excimer or dye lasers used in other ozone lidars significantly reduces the size of the lidar system. Additional wavelengths, i.e., 532 nm and 1064 nm, which are useful for aerosol backscatter profiling, are also available from a YAG laser. (For eye-safety, the remaining laser energy at 532 and 1064 nm can be transferred to 355 nm through use of a nonlinear optical device. This will be done in our next step of lidar improvement.)

The off-line wavelength at 289 nm is chosen because it can be obtained by Raman shifting the YAG laser wavelength through a deuterium Raman cell. This wavelength has several advantages: it is not too far from the on-line wavelength; as with 266 nm, it is in the solar-blind region, so that wide-band solar-blind optics with high transmission can be applied to both wavelengths to reject background radiation at longer wavelengths. In addition, because both the on-line and off-line wavelengths are fixed, and the ozone absorption band is broad, the uncertainty of absorption coefficients associated with wavelength stability of tunable lasers can be avoided.

(2) Range-Coverage Considerations

For a lower troposphere ozone lidar, good near-range coverage is required. It is most interesting and important to observe the ozone distributions in the lower boundary layer. This can be achieved by using a coaxial lidar configuration, i.e., the transmitted laser beam is coaxial with the receiving telescope, or, a biaxial configuration with the laser beam very close to the

receiver. However, these configurations will result in a very high peak in the backscattered signal at near ranges, and an enormous dynamic range in the signal. This dynamic range will make the lidar "short-sighted", i.e., restrict useful lidar signals to within very limited ranges. On the other hand, if the transmitted laser beam is located farther off-axis from the receiver, the far-range coverage will be improved, but the near-range signals will be lost. To solve this problem, we have designed a multibeam transmitter[8], which divides the laser pulse energy among several laterally displaced but parallel beams.

Compared with a single-beam transmitter, a multibeam transmitter in a monostatic incoherent lidar system provides the flexibility of changing the distances between the beams and the receiver axis and changing the allocations of laser energy among the beams, thus changing the overall overlap function and the range response function of the lidar system. A nearly flat near-range response and very close near-range coverage can be achieved simultaneously, even under different atmospheric conditions. Such a significant improvement in range response will solve the problem of detector overexposure by near-range back-scattered radiation (which leads to nonlinear response, saturation, or even damage of the detector), and will significantly reduce the dynamic range of the detector output signal, thus reducing the quantization error in the following digitizer. Consequently, the accuracy of lidar measurements, especially that of the DIAL measurements, is improved. The multibeam transmitter also helps to increase the system efficiency and thus to reduce the size of the lidar, due to the fact that the detector gain can be fully utilized because of the much smaller dynamic range of the signal. It is worth noting, however, that making use of near-range signals requires a very stable system and careful calibration of the overlap functions.

(3) Lidar Size Minimization

For a transportable system, small size is very desirable. This requires a system with high optical efficiency. Besides a multibeam transmitter, the primary methodologies for increasing the system efficiency of our lidar are: (a) improving the optical efficiency of the detector package

at UV wavelengths, (b) optimizing the Raman shift optical configuration, and (c) improving signal processing techniques, especially numerical differentiation.

The optical transmission of the detector package for the UV wavelength is often an unseen bottleneck that reduces the total efficiency of the system. In terms of signal-to-noise ratio (SNR), an increase in receiver transmission by a factor of Q is equivalent to an increase by the same factor in laser energy, laser repetition rate, or telescope receiving area. This is particularly important in the UV region where energy absorption by optical elements is significant. The optical transmission in a system operating at 266 and 289 nm will be only 5-10%, if typical narrow-band (about 1 nm) interference filters are used. This implies that over 90% of the backscattered radiation collected by the telescope is wasted. For special UV spectrometers, the transmission can be on the order of 25%. The optical transmission in our system is made much higher by using a solar-blind interference filter and a series of dichroic mirrors to separate the two wavelengths while maintaining high transmission. Thus the major theoretical limit for this filtering technique is the transmission of the solar-blind filter, typically 70-75%. This is equivalent to an increase of laser energy or telescope size by a factor of at least 3.

The Raman shift configuration is also an important factor in system efficiency with respect to proper utilization of the laser energy. In other ozone lidars using 266 nm as the online wavelength, UV energy at 266 nm is also converted to the off-line wavelength by Raman shift. Although this is a straightforward optical layout, it is inefficient due to the energy loss (reflection and conversion) at the on-line wavelength in the Raman optical branch. Transmitted laser energy at 266 nm needs to be much greater than that at the off-line wavelength because of the much stronger attenuation in the atmosphere. If only ozone absorption is considered and the signals at the two wavelengths are the same at the maximum detection range, then the energy ratio $E_{off}/E_{on} \approx \exp[-2(\alpha_{on} - \alpha_{off})\rho_{o3}z_{max}]$, where α_{on} and α_{off} are absorption coefficients of ozone at on-line and off-line wavelength, respectively. For an ozone mixing ratio of 30 ppb and z_{max} of 3 km, the energy ratio is only 0.03. At higher ozone concentrations, the ratio would be even less. Based on this consideration, we chose a Raman-shift and sum-frequency-mixing configuration[9].

Instead of using 266 nm as the pumping wavelength, the Raman cell is pumped by the residual energy of the second harmonic of the YAG laser at 532 nm. The pumping wavelength is Raman-shifted to 632.5 nm. The off-line wavelength 289 nm is then generated by sum-frequency-mixing the 632.5 and 532 nm wavelengths through a nonlinear crystal. This not only saves the energy at 266 nm, but also makes good use of the residual energy at 532 nm. In addition, it is much easier to utilize standard optics in the Raman branch because the wavelengths are in the visible region.

Numerical differentiation is required to calculate ozone concentrations; however, it is very sensitive to noise and errors. For a given SNR, the accuracy and range resolution of the retrieved ozone concentrations depend very much on the differentiation technique. In other words, a sophisticated numerical differentiation technique can produce the same accuracy and resolution with a smaller SNR (or equivalently, a smaller lidar system), as can be obtained from a simple differentiation technique with a larger SNR (or larger lidar system). Thus, the philosophy is: the better the algorithm in the software, the smaller the size in the hardware. Numerical differentiation methods[10] have been designed to improve the accuracy, range resolution, and temporal resolution in ozone concentration estimation from lidar signals. Our method includes two steps: first, a least-square polynomial fitting for the slowly varying part of the differential absorption optical depth, and second, a subsequent non-stationary Wiener filtering for the fluctuating components. Numerical simulations have shown that these signal processing techniques produce high resolution ozone profiles with much better accuracy than the conventional numerical differentiation method. As a result, the hardware can be less expensive and more compact. However, the version of the lidar that was employed in the two field campaigns described in this report encountered some engineering problems which caused the SNR to be much lower than ideal, and the method described above could not be applied. The low SNR forced us to use other temporary methods that are appropriate for lower range-resolution (i.e., larger range intervals).

2.3 LIDAR SYSTEM DESCRIPTION

A block diagram of the ETL's ozone lidar is shown in Fig. 1. The transmitter and the receiver are assembled side-by-side on an optical breadboard 1.65 m long and 0.75 m wide. The height of the transmitter and receiver are about 0.6 m. Thus the lidar is very compact in size (about 0.75 m^3). There are four beams output from the transmitter, three two-color beams at 266 and 289 nm (with energy allocation of 8%, 18%, and 74% among beams #1, 2, and 3), and one two-color beam at 532 and 1064 nm. A steering mirror set directs the laser beams into the atmosphere in the vertical direction and turns the backscattered radiation into the receiving telescope.

The optical layout of the transmitter is shown in Fig. 2. An Nd:YAG laser is used in the transmitter. The Nd:YAG laser has a second harmonic generator (SHG) and a fourth harmonic generator (FHG) to convert a portion of the laser energy at the fundamental wavelength (1064 nm) to frequency-doubled (532 nm) and quadrupled (266 nm) laser energy which exits the output aperture as a single, three-color beam. The maximum output pulse energy at 1064 nm before SHG, at 532 nm before FHG, and at 266 nm after FHG are 650, 320, and 90 millijoules (mJ), respectively. The maximum energy in the final exiting laser beam at 1064, 532, and 266 nm are 200, 125, and 90 mJ, respectively. The pulsewidth of the laser is on the order of 5-7 nanoseconds (ns). The beamwidth is on the order of 6 millimeters (mm). The laser is not run at maximum energies because the dielectric coatings of the downstream optics have been found to exhibit signs of damage at UV wavelengths when pulse energy exceeds about 60 mJ. Thus the output energy at 266 nm is adjusted much lower than the maximum output, usually within the range of 20 to 40 mJ. (The output energy can be easily adjusted from near zero to the maximum by changing the Q-switch delay of the laser.) The laser can operate at a maximum repetition rate of 10 pulses per second (10 Hz). However, to make the UV laser optics last longer, we operated the laser at 2 Hz during the two field campaigns.

After exiting the Nd:YAG laser, the three-color beam passes through a dichroic mirror,

which totally reflects the 266 nm energy to the UV branch and transmits about 70% of the energy at 1064 nm and about 85% of the energy at 532 nm. The 1064-532 nm pair then propagates to another dichroic mirror which totally reflects the 1064 nm light and partially reflects (about 30%) the 532 nm light. This combination is directed by two harmonic mirrors to pass through an achromatic beam expander with a magnification factor of 3, and finally transmitted into the atmosphere for aerosol profiling. The remaining 532 nm light is transmitted through a lens of 1-m focal length, steered by three dichroic mirrors into a high pressure (about 750-800 psi), 1-m long Raman cell containing deuterium, helium, and xenon, and focused at the center of the cell. The laser pulse exiting the Raman cell consists of the first Stokes line of Raman-shifted energy at 632.5 nm and the residual energy at the pumping wavelength of 532 nm. The gas mixing ratio is optimized to produce a 1:1 photon ratio at 532 and 632.5 nm for a total output pulse energy of about 15 mJ. The two-color beam is then recollimated by a lens of 0.5-m focal length and frequency-summed by a β-Barium Borate (BBO) crystal to generate the off-line wavelength of 289 nm, with an adjustable pulse energy in the range of 0.5-4 mJ. The 289 nm beam is then directed by two UV mirrors to pass through a beam expander to match the divergence of the 289 nm beam to that of the 266 nm beam. After this beam expander, the 289 nm beam is reflected by another UV mirror and transmitted through a dichroic mirror with high reflectivity at 266 nm and high transmission at 289 nm to combine with the 266 nm beam. The two beams are adjusted to be collinear with an angle difference less than 50 μrad. The pair is then directed to an achromatic UV beam expander with a magnification factor of 3, reflected by another two UV mirrors to get closer to the receiver, and then split by two broadband, partially reflecting, UV mirrors and reflected by one totally reflecting UV mirror into three parallel beams, and finally directed by the steering mirror set into the atmosphere.

The receiver consists of a well-baffled Newtonian telescope with an 8 inch diameter off-axis parabolic primary mirror and a field of view of 1.0 mrad. The output beam of the telescope is then directed into a four-wavelength detector package shown in Fig. 3. The UV beam, consisting of two wavelengths, is reflected by a dichroic mirror (high reflectance for wavelengths less than 308 nm) into the UV chamber through a solar-blind filter. The two wavelengths are

then separated through a series of dichroic mirrors with high transmission at 266 nm (>99%) and high reflectance at 289 nm (>99%). Narrow band interference filters are used for the visible and infrared (IR) wavelengths. Atmospheric backscattered radiation at 532, 266, and 289 nm collected by the telescope are detected by photomultipliers. Backscattered radiation at 1064 nm is detected by an avalanche photodiode (APD).

At present, a temporary data acquisition and processing system based on an IBM-486 pc is employed. Lidar output signal at 532 and 1064 nm are digitized by a two-channel, 8-bit, 64 MHz digitizer, and the UV signals are digitized by a two-channel, 12-bit, 10 MHz digitizer. Pulse-to-pulse raw data are written on DAT tapes. The data files are first processed by a raw data averaging and display program. The output ASCII files are then processed with a sophisticated signal retrieval program to obtain aerosol and ozone profiles.

The lidar is installed in a 20-foot sea-container, modified to be a well-insulated, temperature-controlled laboratory with air-bag cushioned floor. Thus, the lidar is transportable. The mobile laboratory has two compartments. The lidar is in the aft compartment; the computer and other instruments, cabinets and counters are in the forward compartment. There is an opening in the top of the laboratory to allow lidar vertical profiling. A movable, temporary scanning mirror set can be installed on top of the opening to steer the beams in the horizontal direction (with a $\pm 15°$ manually adjusting capability) for horizontal and low-elevation observations and system calibrations.

2.4 Horizontal calibration

The lidar was calibrated at all wavelengths in the horizontal direction when the atmosphere was assumed to be horizontally homogeneous. The logarithm of the range-normalized signals, $N(r) = \ln[P(r)]$, were least-square (LSQ) fit by a curve $L(r)$, beyond the full overlap range. The LSQ curve was then extended to the near-range. Thus, we have the overlap

function $\eta(r) = \exp[N(r) - L(r)]$. When the lidar was located at a site with complex terrain (such as the Claremont site, where the lidar was in a gravel pit on the foothills of the San Gabriel Mountains), we calibrated the lidar when the atmosphere was well-mixed. In the future, when the lidar system is ruggedized and stable, the overlap function will also be stable. Then re-calibration after each relocation may not be required. Only a precise alignment of the transmitter and receiver will be needed.

2.5 Data processing

If the lidar signals are free from interferences and distortion, data processing should be straightforward, although not trivial, using the algorithm described in Section 2.1. However, because of the delay in the delivery of the modified sea-container and the subsequent remodification of the sea-container, we did not have time to test the lidar after it was installed in the mobile laboratory and before it was shipped to the field site. Hardware problems related to the new mobile laboratory environment surfaced and affected the lidar signals in the field experiments. The major problems were as follows:

1. **Mechanical instability related to the supporting frames of the lidar**

   When the lidar was in a building, the concrete floor was rigid and the alignment was thus stable. In a mobile laboratory, however, the floor was not rigid, and the supporting frame twisted differently as people stood at different positions. This problem was exacerbated in Davis, because one of the four air-bags underneath the optical table had a slow leak and the pressure kept changing after it was pumped up. In the Los Angeles experiment, we carefully examined and solved this problem by detaching the optical system and the supporting frame, and employing a temporary solution to make the lidar optical table mechanically stable.

(A new supporting structure has recently been designed, manufactured, and assembled that has removed the instability. In addition, a new, much more rigid optical table has replaced the old optical table. These modifications will make the system more stable.)

2. Thermal instability related to temperature control in the mobile laboratory

Because the thermostat in the lidar compartment was installed on the wall, the thermometer sensed the wall temperature instead of the room temperature. In early mornings, the room temperature was warmer than desired, while in the afternoon when the wall was heated by sunshine, the room temperature was much lower than the set temperature. This diurnal variation caused thermal instability in the lidar alignment. In the Los Angeles experiment, we carefully examined the diurnal variation of the lidar alignment, set a thermometer on the lidar, and manually adjusted the air-conditioner to keep the temperature under control. (The new optical table has invar surfaces which are 100 times less sensitive to temperature change than the old one. In addition, the thermostat will be relocated inside the room to improve temperature stability.)

3. Mechanical instability of the horizontal-steering mirror set

This set consists of two separate mirrors. The relative orientation of the two mirrors is not very stable, sometimes causing misalignment during calibrations in the Davis experiment. (A single steering mirror set has been designed, manufactured, and assembled to replace the two-mirror set.)

4. Laser spikes at the beginning of the signals (both in vertical and horizontal signals in Davis and in horizontal signals in Claremont)

The transmitted beams are steered to the vertical direction by a set of dielectrically-coated mirrors and pass through the opening on the top of the mobile laboratory. These mirrors

also scatter laser pulse radiation and reflect stray laser light (mostly at 532 nm) up to the opening. The walls of the opening again scattered the stray light back to different directions. The scattered stray light bounces around in the room and can find its way to the receiver and the detectors, resulting in sharp laser spikes in the beginning of the signals.

In the Davis experiment, the steering mirror set was not covered, and the ceiling surrounding the roof opening was made of white styrofoam. Thus the spikes were very high, especially in the 532 nm channel. The severity of the spikes was not fully realized until the data were analyzed. In the Davis data, the spikes made the 532-nm data of little use, because the signals were seriously distorted in most cases down to the end of the record (1024 points, 9.5 km). The spikes in the UV were less severe, but still had a ringing effect down to about 40 sample points (about 600 m), distorting the near-range signals. The scattering from the horizontal-steering mirror caused additional scattering and higher spikes in the horizontal calibrations.

In the Claremont experiment the roof opening was blackened, and the vertical-steering mirror set was shielded by a black enclosure with small holes on the top to let only the laser beams pass through. These measures eliminated the spikes in the vertical signals but were still not sufficient to remove spikes in the horizontal measurements when the scattering from the horizontal-steering mirror on top of the mobile laboratory was not obscured. These spikes were mostly removed by utilizing vertical signals at the first few points (assuming a well-mixed condition). However, uncertainties in overlap function calibrations at ranges less than 300 m still exist because the possible ringing effect down stream cannot be separated from the signal. (We will install pipe-like baffles to block the scattering from all the steering mirrors in future experiments.)

5. Background noise in the UV channels

The UV wavelengths in our lidar are in the "solar-blind" region. There should be no background noise at all. We knew that the background noise found in the UV signals must be due to visible light leakage inside the detector package, but not until recently did we discover that the location of the leakage was on the baffle (see the dashed line in Fig. 3) between the UV channels and the visible channel. The baffle has holes cut in it to accommodate some optical mounts. These holes allow the visible stray light to enter the UV channels, particularly at 266 nm because more holes existed on the baffle on the back of the 266 nm channel. The background noise at 266 nm was very high when sunlight would shine through the roof opening onto the lidar (early days in Davis experiment before we put a sun shield on the roof), or when the sky was very bright (e.g., sunny afternoons on smoggy days in Claremont). In the worst cases, the noise reached about 10% of the peak of the signal. The background noise causes two problems. First, it causes distortion of the signal after the peak of the signal. Recently, by comparison with airborne ozone measurements in Davis, we found the high signal level of the tail in the 266 nm signal was closely related to the direct current (dc) noise level and the magnification of the photomultiplier tube (PMT). The greater the noise level, the higher the signal level at the tail, resulting in a large negative error in ozone concentration. Second, the background noise causes additional quantum noise (shot noise) in the output signal of the PMT. This noise is induced by the background radiation and is proportional to the square root of the dc noise (see Fig. 4a, an early morning measurement at 7:34 on 9/10/93, with dc noise level at 30, and Fig. 4b, an afternoon measurement at 14:29 pm on 9/9/93, with dc noise level at 1506, in Claremont). This causes a reduced SNR and thus larger range-interval smoothing at far ranges is necessary. The result is lower range resolution. (This problem is being fixed with a modified optical layout and re-machined baffles in the detector package. We are also investigating other potential sources of stray light to fully address the light seal problem. If the noise level is essentially eliminated in the UV, the number of laser shots for one file can be significantly reduced, resulting in

much higher time resolution. Or, if the same number of laser shots is used, a higher accuracy or finer range resolution can be obtained.)

6. The scattering effect of the horizontal-steering mirrors

The horizontal-steering mirrors have aluminum coatings which scatter more light than dielectric coatings. In addition, these mirrors attract dust due to static electricity, causing even more light scattering. The scattering can cause near-field and far-field changes in the transmitted beams. Any changes would result in different overlap functions for the horizontal and vertical directions, because the horizontal-steering mirror set was removed during vertical measurements. We have compared horizontal measurements with vertical measurements taken just before or after the horizontal measurements and discovered that systematic and almost identical changes occur at both wavelengths (thus, the log-ratio of the UV signals remains about the same). In future experiments, two steering mirrors will be used for two-dimensional scanning. Thus the situation will be the same for both horizontal and vertical cases.

The six major hardware problems described above were found during the field experiments and during data processing. Enormous effort was expended to correct the problems by developing algorithms and implementing them in the data processing software. In addition to the hardware-related software developments, aerosol retrieval is another challenging task in data processing because the aerosol optical properties at UV wavelengths in the 266-289 nm region and their vertical variations were mostly unknown. The software developments are summarized below:

1. The system instability problems made processing the Davis data extremely difficult. The system situation changed several times during the experiment, with each instance requiring special treatment to correct the calibration. Because the overlap functions needed correction, sometimes twice per day, processing the Davis data took a long time. To make the correction,

the calibrated overlap functions were compared with the range-normalized vertical signals. A program was developed to modify the overlap function to match the peaks and dips in the vertical signals in order to correct the misalignment in calibration. For minor beam wandering, the overlap function was shifted back or forth a little (±1-2 range gates, i.e., 15-30 m). This was implemented in the main program. In the Claremont experiment, since the system was much more stable and the horizontal calibration was more accurate, we needed only a minor shift (±1 range gate) in some cases to compensate for the residual of the thermal instability.

2. For noise induced signal distortion, we first used a linear least-square fit, $G(r)$, in the far range (from 3.75 to 7.5 km) and extended the linear curve to the near-range. Then, $G(r)$ was subtracted from the signal. During the data processing of the 7/15/93 Davis data, we found that ozone concentrations calculated from lidar measurements were much lower than those from the airborne *in situ* measurements between about 1000 and 3000 m. The differences between the lidar and aircraft measurements increased from mid-morning to early afternoon as the noise level at 266 nm increased significantly. In addition, the error of the estimated ozone concentration increased almost linearly with height. The subtraction method did not work because the linear $G(r)$ was too small compared to the signal in most ranges. According to the positive correlation of the error and the noise level, we developed an empirical formula to correct the noise effect:

$$C_n(i) = \exp[-a\sqrt{n_{dc}/n_0}\ \frac{i(i-M_p)}{200}] \ , \tag{6}$$

where C_n is the correction factor for dc noise level n_{dc} (digits), a is a constant, M_p is the location of the signal peak, and n_0 is a reference dc noise, which is proportional to the PMT gain, g(V), where V is the voltage applied on the PMT. The corrected signal $P(i)$ will be the product of C_n and the uncorrected signal $P'(i)$:

$$P(i) = P'(i)C_n(i), \qquad i \geq M_p. \tag{7}$$

Although it is a crude correction, we found it improved the comparison from a negative difference of about 30 ppb to less than 10 ppb between 2 and 3 km in the Davis intercomparison.

This correction has been applied to the 266 and 289 nm signals, but the impact is much lower at 289 nm. The same correction was implemented in the Claremont data processing program. This correction improves the accuracy of ozone concentration retrieval above 1000 m to within 10 ppb.

Because the correction depends on the dc noise level, very careful examinations of the data were conducted to separate the background radiation noise from the electro-magnetic interference (EMI) and the baseline shift which might be caused by either the digitizer or the preamplifier.

Based on a previous observation in Boulder when the background radiation was very low, we found that an additional correction (depends on integrated signal output of the PMT) needs to be implemented, but this is a minor correction in most cases.

3. For the interference resulting from laser spikes and the resultant uncertainty of the overlap function in the near-range, the distorted range-normalized and overlap function removed signal $S(z)$ should be:

$$S(z) = \frac{P'(z)z^2}{\eta(z)} = \frac{S_p(z)}{\eta(z)} + [1+\delta\eta(z)]C_A\beta(z)T^2(z), \tag{8}$$

where $S_p(z)$ is the broadened laser spike, and $\delta\eta(z)$ is the relative uncertainty of the overlap function. To avoid the near-range problem, three steps of ozone concentration retrieval were used:

a) The first-order ozone retrieval

The result of the first-order (initial) ozone retrieval must be reasonable and close to the true values because we need to remove the ozone transmission term in both UV wavelengths (266 and 289 nm) for further correction. In the lowest few hundred meters, we do not differentiate the log-ratio, $ln[F(z)]$, to retrieve ozone concentrations.

Differentiation of the distorted near-range $ln[F(z)]$ could produce absurd results (e.g., a negative ozone mixing ratio), that would lead to an unrealistic value of the ozone transmission and subsequently a poor estimate of the ozone-transmission-removed "aerosol backscattered signal". Since the only available information is the surface ozone concentration (ρ_0), in the first-order retrieval ozone concentrations in the first few hundred meters are assumed constant ($\rho_{o3}(z) = \rho_0$). This assumption yields a much better estimate of the ozone transmission and the ozone-removed aerosol backscattered signal in the near range. The difference between the true profile of ozone concentrations and the surface ozone concentration [i.e., $\Delta\rho_{o3} = \rho_{o3}(z)-\rho_0$] can essentially be corrected by the "aerosol correction" discussed in the following section. However, within the first 100 m, the results depend mainly on the surface value.

b) The aerosol retrieval

In reality, interference and uncertainty terms, such as $S_p(z)$, $[1 + \delta\eta(z)]$, and $\Delta\rho_{o3} = \rho_{o3}(z)-\rho_0$, were also included in the "aerosol profiles" from the Davis data. An example of the Davis data is shown in Fig. 5a, where the extinction coefficient is unreasonably high below 500 m. To the trained observer, ringing of the laser pulse down stream is obviously superimposed on real aerosol profile. The aerosol retrieval began at 120 m. If the retrieval started at 30 m, the peak "extinction coefficient" would have been 10 times higher. The peak can be seen in Fig. 5b, the log-normalized signal in the UV. Although there are no physical reasons to include $S_p(z)$ and $[1 + \delta\eta(z)]$ in aerosol retrieval, their inclusion yielded much more realistic ozone concentration than without.

c) The final ozone concentration retrieval

To determine the final ozone concentration profile, the log-ratio of the "aerosol profiles" (289 nm to 266 nm) is subtracted from the original $ln[F(z)]$. This step correct most of the spike's impact, the uncertainty of the overlap function, the difference $\Delta\rho_{3,}$, and the

acrosol effect. Next, the corrected $ln[F(z)]$ is extrapolated to the surface using least-square fit and differentiated. The final ozone profile beginning 15 m above ground level is obtained.

4. The effect of the horizontal-steering mirror (problem No. 6) was roughly corrected by using the ratio of the horizontal signals and vertical signals measured alternatively in the same time period in Claremont when the atmosphere was assumed to be well-mixed. This ratio was also applied to the Davis data because the mirror is the same, and the data quality is much better for Claremont than for Davis.

5. Because the impact of the high spikes in the Davis experiment cannot be fully removed by the software remedy, the near range resolution is much poorer than theoretical values (< 100 m). The resolution was about 300 m below 1000 m. The resolution was highest in the middle range (1000 to 2000 m), about 150 - 200 m, and become worse again at far ranges (above 2000 m), about 400 m, because of the low signals and high background noise. In the Claremont experiment, however, the resolution was close to the theoretical prediction (i.e., about 50 to 100 m at near ranges below 1000 m, increases to about 200-300 m at 3000 m if the signal at 266 nm is still processable). If the sky is bright and the ozone concentration is high, the low SNR necessitates a broader range interval to smooth both the raw signals and the ozone retrieval.

6. In a complicated aerosol environment (like Los Angeles) where aerosol properties change significantly with altitude, we need a model to assign the values of parameters in the aerosol backscatter coefficient and aerosol extinction coefficient retrieval. The most important parameter for aerosol retrieval is the backscatter-to-extinction ratio, k. This ratio depends both on the chemical composition as well as the size distribution of the aerosol. Besides the aerosol model, the iteration algorithm developed in recent years (for example, Kovalev[11]) also needed to be modified. We developed a different algorithm that does not need to obtain the aerosol extinction coefficient by subtracting the molecular extinction coefficient from the total extinction coefficient. Thus, the new algorithm prevents negative values of aerosol extinction coefficient.

A series of tests showed that this algorithm is not very sensitive to aerosol models. Because of the complexity of aerosol retrieval from lidar signals, a detailed description of the mathematics will not be included in this report.

3. THE INTERCOMPARISON EXPERIMENT IN DAVIS

The first field campaign was an intercomparison experiment between the ETL ozone lidar and the UC-Davis DASIBI UV ozone analyzer on board a Cessna 172 airplane. The experiment was carried out during the period of July 9 to July 23, 1993, near Davis, California.

This marked the first long distance trip of the ozone lidar system in the modified sea-container (seatainer), and was the first time that the lidar system made measurements from the seatainer. Mechanical difficulties caused by vibrations during the transport were discovered (e.g., screws fell out or loosened, causing serious laser misalignment). A decrease in gas pressure of the Raman cell was also discovered. These mechanical problems, and the difficulties with power supply were solved in just three days after very hard work by the lidar crew and help of CARB personnel.

The observation site was on private property, about 200 m west of Yolo County Airport and 30 km west of the city of Sacramento. The lidar was surrounded by tall trees. Horizontal observations for calibrations were made on the southern side where there was a small clearance. The airplane spiraled up and down a crudely defined square column with each side varying from 4 to 7 km. The airplane spirals were centered about 2-4 km northwest of the lidar. (See examples of the flight path in Appendix F.) Thus, the lidar was close to the southeast side of the flight column.

We began the intercomparison experiment on July 14 and about 200 data files were collected during seven week days. During each of those days, one to three aircraft flights were made; each flight consisted approximately of a 30-minute ascent and 30-minute descent. The flights took place at various times of the day between early or mid-morning and mid-afternoon. The lidar operated continuously during the flights, and usually gathered additional data before and after the flights.

As mentioned in Section 2.5, hardware problems existed in the newly completed mobile lidar in the Davis experiment. The large amount of insects below 20 m might have also contributed to the beginning spikes. However, the software remedies alleviated the problems. Most of the data that were affected by minor system instability and PMT distortion were recovered. These data exhibited a generally good agreement between the airborne *in situ* ozone measurements and the ozone lidar measurements. Only a small portion (about 20%) of the Davis data that had either severe misalignment due to the twisted optical table or severe signal distortions were not recoverable.

It is worth noting the methodological differences between the airborne *in situ* measurements and the lidar measurements before discussing the results of the intercomparison. The lidar was pointed vertically and operated at 2 Hz. Each file contains 900 records, and each record contains the lidar signals at three wavelengths in a single laser ignition. Thus, each vertical ozone profile was an average over 450 seconds (7.5 minutes) at a fixed location. Depending on wind speed which can vary with altitude, this 7.5-minute average could be equivalent to an averaged profile over wind trajectories of path lengths ranging from 0 to 10 km. (The number of records in one lidar file was determined by the signal-to-noise ratio in the far ranges. Once the UV background noise is eliminated, this number can be significantly reduced. Or, if the lidar is operating at 10 Hz, the time period for each file will also be greatly reduced.) However, the airplane spiraled up and down with a vertical axis not centered over the lidar and projecting a large horizontal square, each side of which was much greater than the altitude range. The airborne DASIBI data are 10-second averages and correspond to averages over 0.3 to 0.5 km of the flight path which was horizontally 0 to 8 km away from the lidar. In addition, the airborne measurements have an altitude resolution of 20-30 meters; as noted earlier, hardware problems caused the lidar measurements in Davis to have a much lower resolution (200-300 m below 1000 m and above 2000 m). (The fine variations shown in the profiles measured by lidar are the result of a moving average process over 200-300 m.) Temporal variations of ozone can be significant as shown in both the airborne measurements and lidar measurements (see Figs. 6a

and 6b). Horizontal variations may also be significant in certain circumstances, especially at higher altitudes. Consequently, temporal and spatial variation, range resolution, and lidar errors are all included in the differences between the aircraft and lidar measurements.

Considering the above methodological differences, each ozone profile measured by the airplane in one spiral (about a half hour) is matched with one to four contemporaneous lidar-measured profiles to perform as accurate an intercomparison as possible. In each lidar-measured ozone profile only the one altitude section that matches the time of the airplane measurement is used. Thus, figures show discontinuities in the lidar-measured profiles. Examples of ten intercomparisons from July 15, July 19, and July 22 are shown in Figs. 7a-7j. When the atmospheric conditions were stable and the ozone profiles exhibited small variations, the agreement between the lidar measurements and the airborne measurements were good (e. g., the morning to noon observations like Figs. 7a, 7b, and 7e). When atmospheric ozone concentration varied rapidly (e. g., the afternoon observations in Fig. 7g, 7h, and 7j), greater differences between the aircraft-measured and lidar-measured ozone profiles were observed. In the afternoon, convective activities might have caused cells or columns that led to greater horizontal variations. It is interesting to note that when ozone concentrations fluctuated in higher altitudes as measured by DASIBI, the lidar measured profiles go straight through the middle of the fluctuations like vertically averaged profiles. A reasonable explanation is that the lidar has a lower range resolution in the altitude range from 2500 to 3500 m. If the aircraft-measured profiles were smoothed with a resolution similar to the lidar's, the results might have been closer. In fact, a running smoothing of the airplane profiles (the averaging interval was ±20 points, equivalent to 500 to 600 m) at higher altitudes was carried out in Figs. 7h and 7j. The smoothed airplane profiles have less fluctuations and are much closer to the lidar profiles.

Statistical calculations for the intercomparisons were carried out for three altitude intervals (i.e., 0 to 1000 m, 1000 to 2000 m, and 2000 m to 3500 m). Twenty comparisons of the ozone profiles are included in the calculation for each layer as the differences in the ozone measurements ($\Delta O_3 = O_{3lidar} - O_{3air}$) are calculated with a 50-m interval. Then the average value of

ΔO_3, $a_{\Delta o3}$, defined as

$$a_{\Delta o3} = \frac{1}{N}\sum_{i-1}^{N} \Delta O_{3i} \ , \tag{9}$$

and the root-mean-square of (ΔO_3 - $a_{\Delta o3}$), which represents the random fluctuation around $a_{\Delta o3}$, defined as

$$\sigma_{\Delta O3} = \sqrt{\frac{1}{N}\sum_{i-1}^{N} (\Delta O_{3i} - a_{\Delta o3})^2} \ , \tag{10}$$

are calculated. A total number of 611 and 392 points were used for the statistical calculations in the morning and afternoon, respectively. The results are listed in Table 1. The statistics show that the absolute values of the bias between the lidar and the airborne measurements were less than 3 ppb for both morning and afternoon, except for the 2000 - 3500 m interval in the morning, when the bias is -3.7 ppb. The root-mean-square (r.m.s) of the random differences were less than 10 ppb, except for the highest altitude interval. The r.m.s of ΔO_3 increased with altitude, and were greater in the afternoon above the boundary layer than those in the morning. This might indicate that the atmospheric ozone concentrations were more horizontally inhomogeneous in the afternoon as mentioned above.

Table 1. Intercomparison of Ozone Vertical Profiles

	Morning to Noon		Afternoon	
Altitude (m)	Average of ΔO_3 (ppb)	r.m.s of (ΔO_3 - $a_{\Delta o3}$) (ppb)	Average of ΔO_3 (ppb)	r.m.s of (ΔO_3 - $a_{\Delta o3}$) (ppb)
0 - 1000	1.4	5.9	0.9	5.5
1000 - 2000	0.1	7.5	-2.8	8.3
2000 - 3500	-3.7	10.5	1.5	14.7

In additional to the vertical intercomparisons in Davis, a horizontal intercomparison

between the lidar and a TECO UV ozone analyzer were carried out using data collected in Boulder, Colorado, Davis, CA, and Claremont, CA, as a by-product of horizontal calibrations. The ozone analyzer was always at the lidar site. Because the lidar measured ozone concentrations at the site were obtained by extrapolation from 1 km away from the lidar, this was not a good location for horizonal intercomparisons. However, the results are still interesting. They are summarized and shown in Fig. 8. The following relationship between the lidar and the TECO measured ozone mixing ratios was obtained through linear regression:

$$y = 1.088x - 0.215 \ (ppb), \tag{11}$$

where y is the lidar measured ozone mixing ratio (in ppb), and x is the TECO reading (in ppb). Ozone lidar results were systematically higher than those of the TECO's by 8.8%. The standard deviation of the statistical difference is 5 ppb. The systematic difference was most likely caused by the TECO measurements in Davis. As mentioned earlier, the lidar site was surrounded by tall trees. The TECO reading was always lower (about 5 to 15 ppb) than the reading of the DASIBI when the airplane was landing at the Yolo County Airport, only 200 m away from the lidar. To show the bias of TECO readings, a straight line (y = x) is plotted in Fig. 8. One can see that all the Davis points are on the left side of this line. The x distances from the line to these points are in the range of -2 to -15 ppb, similar to the differences between the TECO and the airplane DASIBI readings. If the TECO ozone analyzer had been set up at a distance (e.g., 1 km) away from the lidar, the results would likely have been much better.

Even if all the differences are due to errors in lidar measurements, the above intercomparisons have shown that the overall error bar for the ozone lidar measurement is acceptable, less than ±10 ppb below 2000 m, and is slightly higher from 2000 to 3500 m. When current improvement to the system are completed, the accuracy will be improved more.

4. OZONE LIDAR OBSERVATIONS IN CLAREMONT

The second field experiment involving the ozone lidar was the Los Angeles Atmospheric Free Radical Study, carried out in Claremont during September of 1993. The lidar arrived at the Claremont site on August 27. During the first few days, we had some power supply and mechanical problems. More serious problems were associated with the mechanical supporting system for the optical breadboard, and the optical breadboard itself. We had added a rigid frame after the Davis experiment to strengthen the optical breadboard. However, the configuration induced stronger stresses which caused the optical breadboard to twist even more (tearing the undersurface apart from the core of the optical table) and significantly affected the stability of the optical system. After discovering the problem, we unscrewed the breadboard from the frame and used a temporary remedy. This worked well and resulted in a stable alignment and good data sets. The system had also been improved to eliminate spikes in the beginning of signals at all three wavelengths in the vertical direction. Although spikes still existed in horizontal signals (obtained during calibrations) because of scattering by the horizontal-steering mirror, the problem was not as severe as in the Davis experiment.

The ozone lidar started taking data on September 4 at the Claremont site. We gathered a complete data set throughout the highest ozone episode in 1993, from the building up period (September 4 through 8, 1993), the climax period (September 9, the peak surface ozone concentration was 341 ppb!), and the fading period (September 10 and 11). We also obtained data during the relatively clean period from September 12 through 14. Low clouds on the clean days, however, prevented lidar observations until afternoon. For lidar systems with wavelength shorter than 2 microns (μm), low clouds with dense concentrations of micron-sized water droplets can seldom be penetrated by laser beams beyond few tens of meters. This is a limitation to lidar observations. Later (September 18 and 19), a second ozone episode with peak ozone concentration of about 200 ppb was observed.

Contoured time-height charts of ozone mixing ratios during the four days (September 8-11, 1993) associated with the highest ozone episode are shown in Figs. 9a-9f. In theses charts, the detailed temporal and spatial structures of the ozone mixing ratio below 1000 m are shown. Figs. 9c and 9d show the ozone variation in more detail on 9/09/93 in the morning and in the afternoon, respectively, with finer resolution (15 ppb for the morning and 20 ppb for the afternoon). A brief description of the temporal evolution of the ozone vertical profiles follows. In the early morning there was a shallow layer of low ozone concentrations from the ground level to about 100 m. The ozone concentrations increased with height and peaked around 400-500 m. An additional ozone peak at 150-350 m appeared a little later and disappeared in the mid-morning on 9/09/93. The afternoon high peak of ozone arrived at the site around 2 pm (see Figs. 9b, 9d, and 9f). The charts show a very rapid increase in ozone concentrations upon arrival of the polluted air mass and a strong concentration gradient at the top of the inversion, indicating the high concentrations of ozone were trapped in the marine boundary layer.

Examples of individual ozone profiles and atmospheric backscatter (including aerosol and molecular backscatter) profiles at 532 nm on 9/09/93 are shown in Figs. 10a-10f and 11a-11f, respectively. Balloon soundings of temperature and relative humidity at 7:56 and 11:00 are shown in Figs. 12 and 13, respectively. The derived absolute humidity profiles are shown in Figs. 14a-14b. Two inversion layers can be seen in Figs. 12a-13b: a strong one (3-7° C temperature increase in 200-300 m) near ground level (between the surface and 500 m at 8:00 am and between 200 and 500 m at 11:00 am); a weaker one at about 4000 to 4500 m. The relative humidity had a maximum at the surface in the early morning and rose with the base of the inversion to 200 m by late morning. It decreased rapidly to a minimum of 5-10% at 500 - 1000 m, and then gradually increased to 30-40% around 4000 m. There was a sharp decrease between about 4000 and 4500 m. Above 5000 m the relative humidity was almost constant at 5-10%.

The aerosol profiles (Figs. 11a-11e) show four distinctively different layers. The surface layer below 200 m was very smoggy, especially in the afternoon. A layer between 500 to 900 m was very clean. A second layer with abundant aerosols was between 1000 to 4500 m. Above

5000 m the air was very clean. The structure of aerosol distribution was very closely associated with the humidity and temperature structures.

The low-level aerosol content had a temporal variation similar to that of the surface ozone in the afternoon. The second aerosol layer, however, behaved differently. Although the temperature and humidity (both relative and absolute) did not have any significant increase, the aerosol backscatter increased steadily from early morning till late afternoon. In the late afternoon, the middle part of this layer, between 2000 to 4000 m, the growth of the backscatter coefficient was particularly vigorous. This might be an indication that the aerosols in this layer were transported aloft by the chimney effect of the San Gabriel Mountains.

The lidar observations confirm that both ozone and aerosol distributions are significantly affected by the meteorological conditions.

Keith[13] (1980) describes climatological conditions typically found within the Los Angeles basin. The basin is characterized by a marine air influence and temperature inversion, especially during the hot summer months. Strong diurnal heating generates a consistent land/sea breeze. On-shore flow from the Pacific ocean is modified as it moves inland toward the experiment site. Therefore, the strength of the marine inversion is highly dependent on the strength and duration of the westerly winds. The westerly sea breeze increases in strength toward mid-afternoon to around 4-6 ms^{-1}.

Previous studies[14] (Roberts and Main, 1993) have shown that high concentrations of ozone often exist aloft. Mechanisms for this include undercutting of the mixed layer by the sea breeze, slope flows along the mountains and their resulting return flow back toward and over the LA basin, and penetration of low-level polluted air into the inversion layer. Urban Airshed Models (UAM) have experienced difficulty in modeling these conditions due to the complexity of these patterns. The MPS and the ozone lidar presented a unique opportunity to observe the atmospheric structure and ozone profile simultaneously, with temporal and spatial resolution

providing a better description of these processes than was possible in the past.

Shown in Figs. 15a - 15h are time series of vertical profiles of wind direction and speed during September 8 to 12, 1993, measured by the wind profiler in the MPS system. Each profile is an hourly average. Figs. 16a - 16d show the time series of temperature profile measured by RASS during September 8 to 11. The temperature measurements by both balloon and RASS confirm that during the highest ozone episode there was a persistent shallow inversion layer with the top at about 500 - 600 m (AGL), equivalent to about 900 to 1000 m ASL. The inversion was very strong on the 9th and 10th, and weaker on the 8th and 11th of September. The ozone profiles match the temperature profiles very closely. When the top of the inversion layer was lower (about 500 m AGL) on 9/09/93, the highest ozone concentrations were trapped below 400 m, and the maximum was at ground. When the top was a little higher (about 700 m) and the inversion was weaker, the layer of high ozone concentrations was about 500 m deep, and the maximum of ozone concentration appeared at about 250 m.

Fig. 17 is a time series of 30-min average wind directions at three heights observed during a high pollution day as part of LAFRS (9 September 1993). Not shown is the height of the marine inversion or the mixing depth. The inversion, as monitored continuously by profiler/RASS and confirmed by balloon launches, was shallow and surface-based, extending to a height of about 600 m. Surface heating lifts the base of the inversion, but is not able to completely break through the shallow but strong inversion. Early morning surface winds are from the north-northeast, consistent with a drainage off the San Gabriel mountains. As local heating begins, the winds first shift to the southeast before becoming westerly. Wind speeds are light during this transition period. Winds above the surface (200 m), but below the inversion, exhibit a more easterly component corresponding to the larger scale land breeze. This air appears to be riding over the colder local drainage off the mountains. Wind directions above the inversion (500 m) are consistent with those at 200 m, except for an earlier and more rapid shift from the easterly land breeze to a westerly sea breeze.

In Figs. 9a- 9c we see that there is a low-level peak in ozone which varied in height from 150 m to 350 m beginning just after sunrise. This peak has an early morning maximum corresponding in time with the sudden change of the winds below the inversion, in response to the inland heating. This maximum is believed to be transported ozone trapped within the inversion layer. Surface ozone is also increasing at this time, but in a slower and steadier fashion consistent with local production. Fig. 18 is the time series of the measured surface ozone for the same time period as Fig. 17. About 10 am the light winds shifted from an easterly (from the east) to a westerly (from the west) directions. Later, as wind speeds increased with the inland penetration of the modified sea-breeze, ozone concentrations increased rapidly in the lowest 300 m (see Fig. 9d). As heating increased the mixing depth over Los Angeles, ozone is carried aloft and advects downwind. This would explain why the variation in ozone concentrations aloft so closely followed the trend in ozone concentrations at the surface. This analysis is for a day with a very strong inversion and a well defined land/sea breeze, but similar data sets can be used to examine other days during LAFRS with different wind patterns and vertical mixing. For example, Fig. 9e exhibits a less organized pattern with lower concentrations wile Fig. 9f (for September 11) exhibits a pattern similar to the September 9 episode except that the inversion was not as strong and some polluted air was able to mix above 500 m.

Temporal variations of the ozone concentration profile on September 5 ,7, 13-14, 18-19, 1993 are also shown in time-height charts in Appendix G. Usually lidar observations started at 7-8 am and stopped before 6 pm. However, on September 7 (the day after Labor Day) lidar observations began very early, two hours before dawn, and on September 19 the measurements continued after sunset until 9 pm. The early morning (before 10 am) patterns on September 5 and 7 showed medium ozone concentrations without high peaks, which were different from the morning patterns on September 8-11. The afternoon pattern on September 19 was similar to, but weaker than, that of September 11. In the evening of September 19, ozone concentrations in the lowest few hundred meters decreased rapidly with time, while above 500 m concentrations remained approximately the same and exhibited a peak (about 100 ppb) at around 700 to 1000 m.

5. SUMMARY AND CONCLUSIONS

The ETL ozone lidar was employed in two field experiments sponsored by the California Air Resource Board in 1993. The first experiment was an intercomparison experiment involving the ETL ozone lidar and a UC-Davis airborne DASIBI ozone analyzer near Davis, California, during July. The purpose of the experiment was to verify the capability of the ETL ozone lidar, test the integrity of the system for further improvements, and to improve the data retrieval algorithm and processing techniques for better accuracy of ozone observations. The ETL ozone lidar later participated in the second experiment, the Los Angeles Atmospheric Free Radical Study, to test the performance of this lidar in a very polluted environment like the Los Angeles basin, and to obtain a first-hand information about ozone and aerosol vertical distributions at one location in such an environment. As part of the LAFRS, ETL staff made vertical observations of ozone with the lidar and of the temperature and humidity with the Mobile Profiler System (MPS) during September 1993 in Claremont (eastern Los Angeles County). The highest ozone episode of the year was encountered during this field experiment. After the experiments, enormous effort was put into the data processing techniques and corresponding software. Data were processed and interesting results were obtained.

The major conclusions of the project are summarized as follows:

1. The ETL transportable ground-based lower troposphere ozone lidar has been deployed and tested in two field experiments, which demonstrated that this ozone lidar can:

    - Measure ozone mixing ratio vertical profiles from near the surface up to 3 km in medium-high ozone concentrations (surface ozone less than 150 ppb), and up to 2 km in very smoggy conditions (ozone concentrations more than 200-300 ppb). The near-range coverage is unique among similar ozone lidars, and the maximum detection range is the same or longer than much more powerful ozone lidar

systems (see Reference 12). The range covers the total boundary layer and the lower free troposphere.

- Measure ozone mixing ratios in the whole detectable range with an accuracy of better than 10 ppb up to 2 km, and with an accuracy better than 15 ppb from 2 to 3.5 km (in the present status of the hardware), and with potentially higher accuracy when the system is improved.

- Measure aerosol backscatter and extinction coefficient profiles at 532 nm from near the surface up to 9 km on a sunny day, even when the surface layer was very smoggy and the visibility was very low. (The aerosol backscatter at UV wavelengths can reach to about 3 km.)

2. Because of the unique capability of the ETL ozone lidar, it is a powerful tool for air quality monitoring and research. Concurrent and co-located measurements by the ozone lidar and other meteorological remote sensing instruments (e.g., the MPS) provide temporal and spatial variations of both ozone concentrations and meteorological parameters and provide unique and new insights into the vertical and horizontal processes affecting ozone concentrations. The aerosol profiling capability provides more information about the chemical and physical processes affection aerosols.

   The ETL lidar is ground-based and can monitor ozone and aerosol profiles continuously during an experiment. A two-dimensional elevation-scanning system is being built to monitor the distributions of ozone with an area of 5×3 km^2, and the aerosol distribution with an area of 10×8 km^2 in a vertical plane. When co-located with a wind profiler or a Doppler lidar, very useful measurements of ozone and aerosol flux are possible to perform.

3. Important experience has been gained about how to improve the lidar hardware in the

future. Improvements have been done or are under way to correct engineering imperfections, to ruggedize and optimize the lidar, and to minimize stray light and electromagnetic interference.

4. Interesting and important information about vertical distributions and temporal variations of ozone and aerosol in the very complex environment of the Los Angeles basin was obtained in the LAFRS experiment in Claremont, where the highest ozone episode in 1993 was observed. The ozone and temperature profiles and their temporal evolution clearly show that high ozone concentrations were trapped under the top of the marine boundary layer. The aerosol profiles had four distinctively different layers, which were closely associated with temperature and humidity structures. The lidar observations confirm that both ozone and aerosol distributions are significantly affected by the meteorological conditions.

BLOCK DIAGRAM OF THE OZONE LIDAR

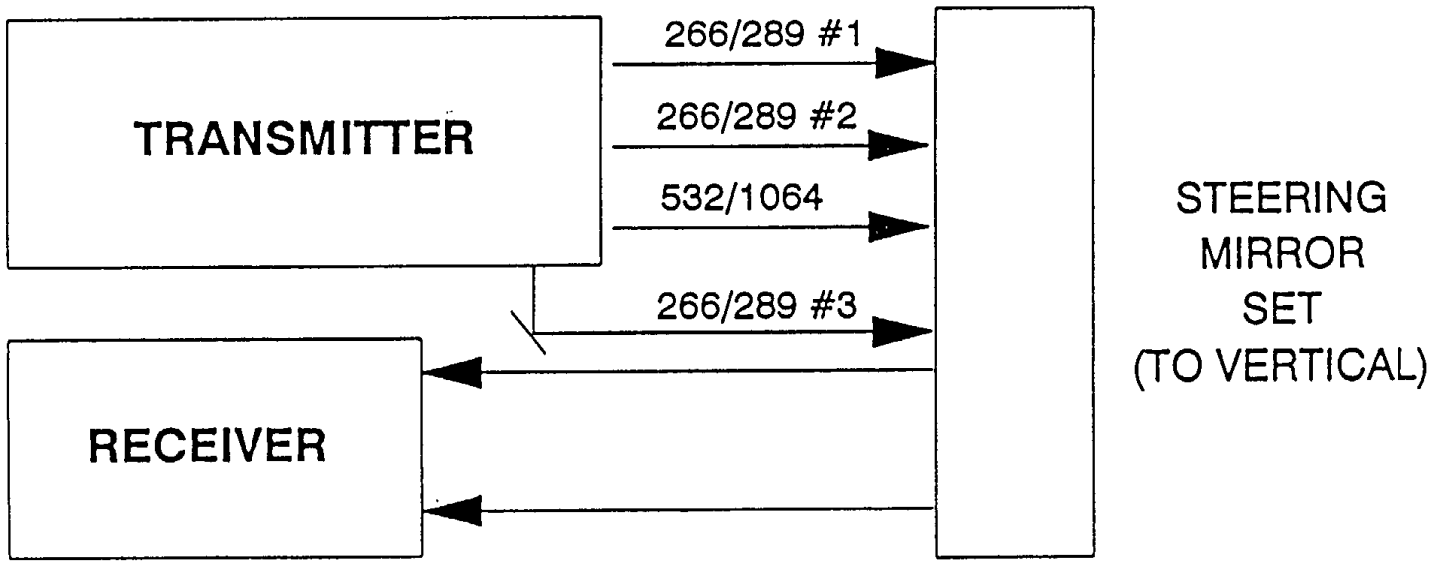

Fig. 1

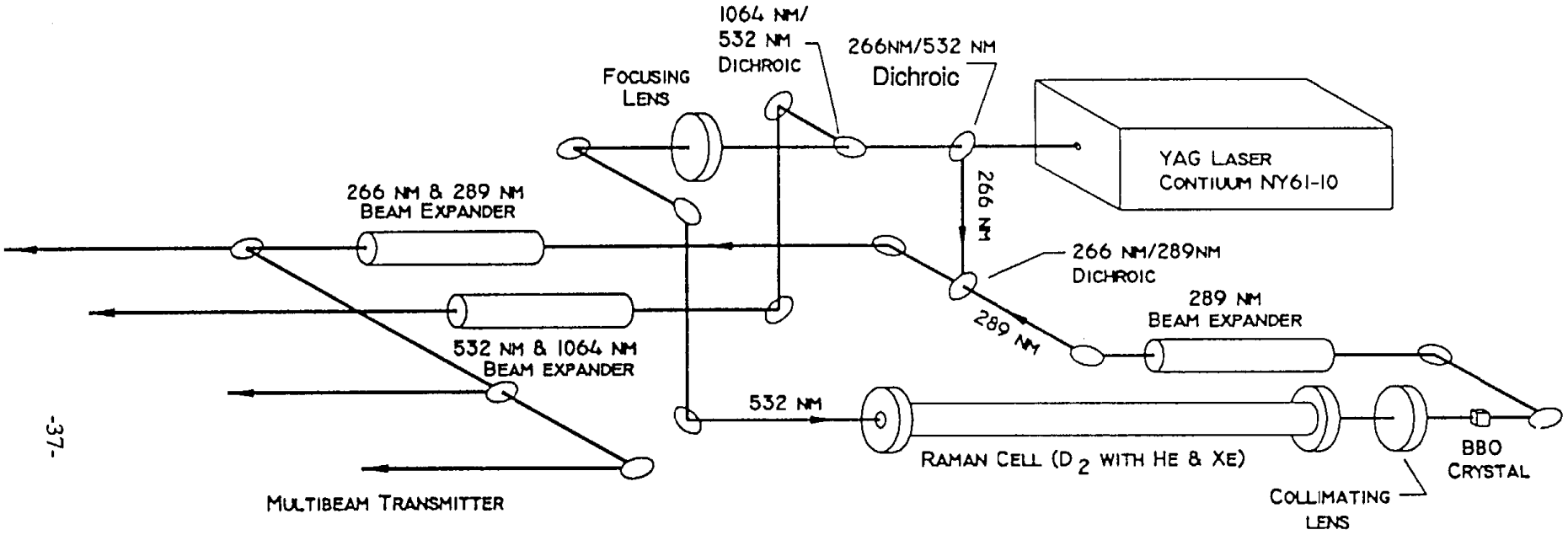
OPTICAL LAYOUT OF THE OZONE LIDAR TRANSMITTER
1064 NM/
532 NM
DICHROIC
266NM/532 NM
Dichroic
FOCUSING
LENS
YAG LASER
CONTIUUM NY61-10
266 NM & 289 NM
BEAM EXPANDER
266 NM
266 NM/289NM
DICHROIC
289 NM
BEAM EXPANDER
289 NM
532 NM & 1064 NM
BEAM EXPANDER
532 NM
RAMAN CELL (D 2 WITH HE & XE)
BBO
CRYSTAL
COLLIMATING
LENS
MULTIBEAM TRANSMITTER

Fig. 2

TOP VIEW OF DETECTOR PACKAGE

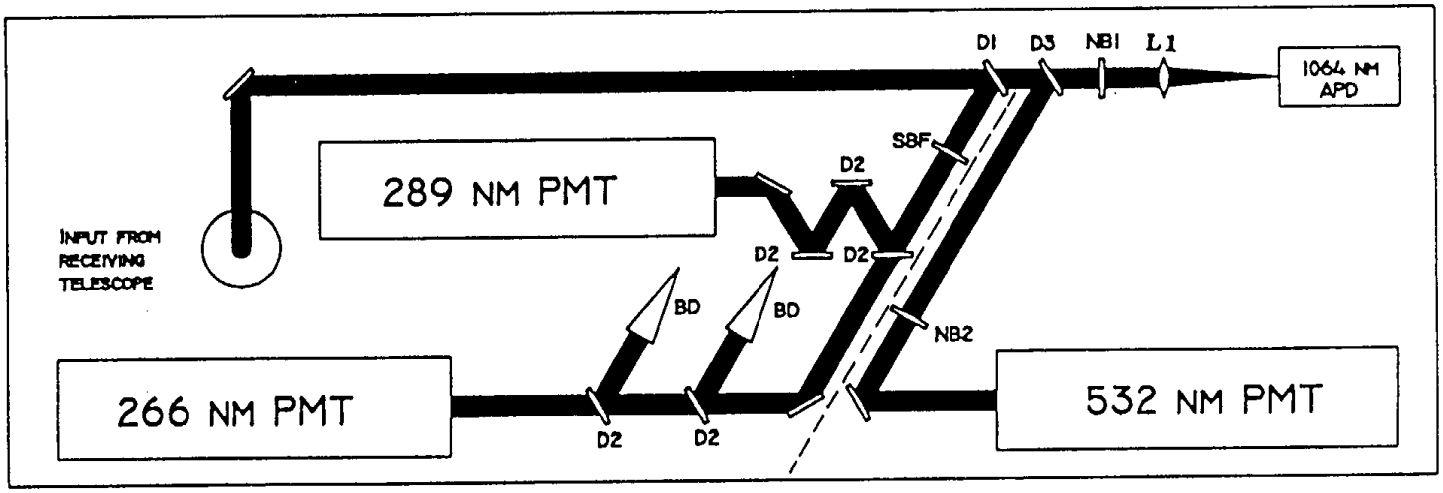

D1:	DICHROIC BEAMSPLITTER, T>308 NM, R<308 NM	T - Transmitted R - Reflected
D2:	DICHROIC BEAMSPLITTER, T=266 NM, R=289 NM	
D3:	DICHROIC BEAMSPLITTER, T=1060 NM, R=532 NM	
SBF:	SOLAR BLIND FILTER	
NB1:	NARROW BAND FILTER, 1060 NM, 1 NM BANDWIDTH	
NB2:	NARROW BAND FILTER, 532 NM, 1 NM BANDWIDTH	
L1:	LENS, PLANO-CONCAVE, 25 MM focal length	
BD:	BEAM DUMP	

Fig.3

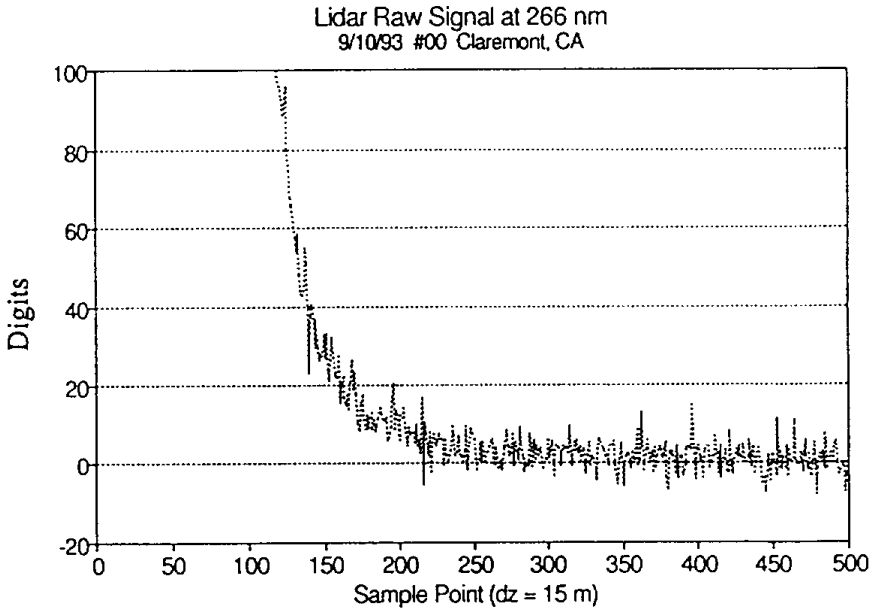
Lidar Raw Signal at 266 nm
9/10/93 #00 Claremont, CA
Digits
100
80
60
40
20
0
-20
0
50
100
150
200
250
300
350
400
450
500
Sample Point (dz = 15 m)

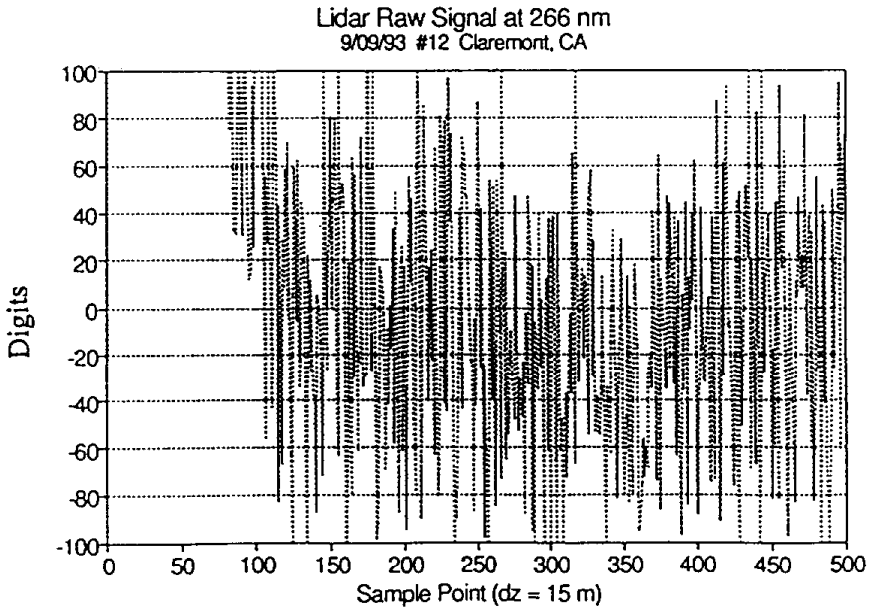
Lidar Raw Signal at 266 nm
9/09/93 #12 Claremont, CA
Digits
100
80
60
40
20
0
-20
-40
-60
-80
-100
0
50
100
150
200
250
300
350
400
450
500
Sample Point (dz = 15 m)

Fig.4

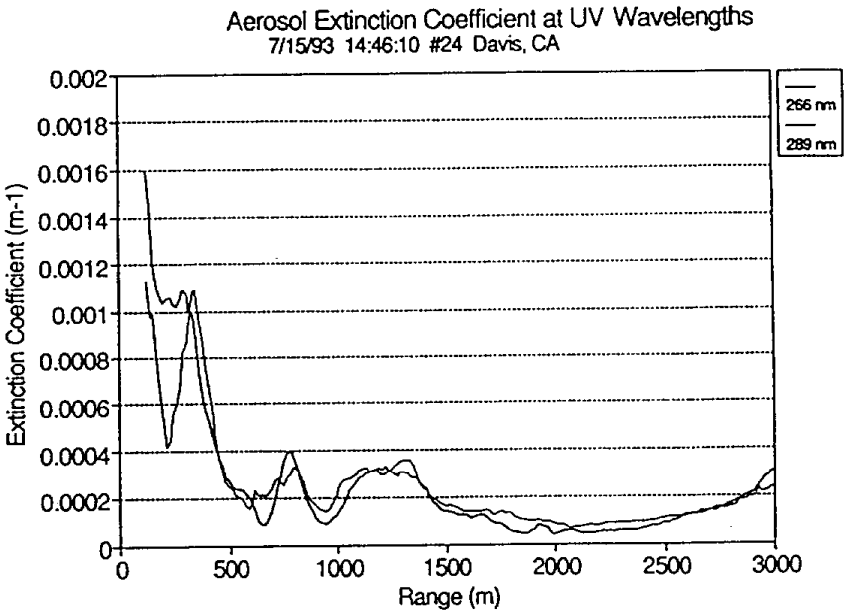
Aerosol Extinction Coefficient at UV Wavelengths
7/15/93 14:46:10 #24 Davis, CA
Extinction Coefficient (m-1)
0.002
0.0018
0.0016
0.0014
0.0012
0.001
0.0008
0.0006
0.0004
0.0002
0
0
500
1000
1500
2000
2500
3000
Range (m)
266 nm
289 nm

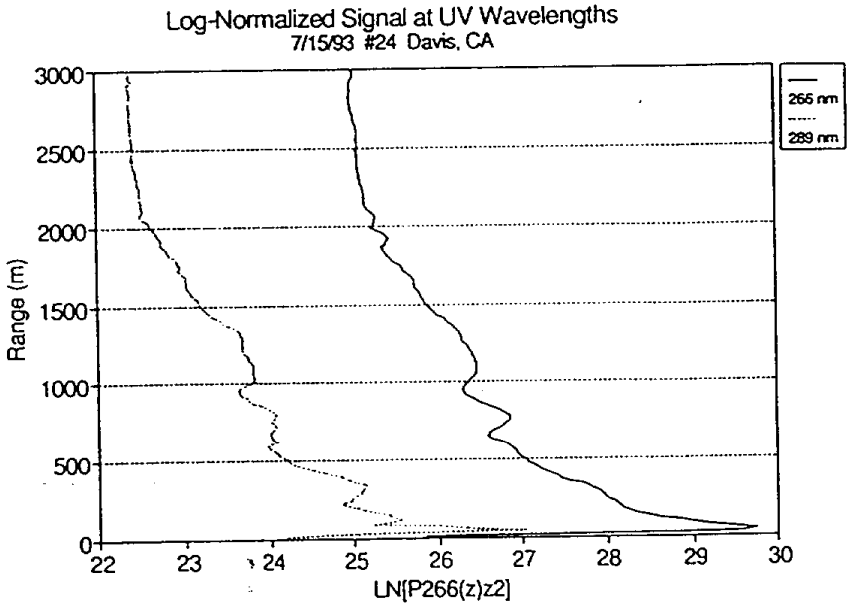
Log-Normalized Signal at UV Wavelengths
7/15/93 #24 Davis, CA
Range (m)
3000
2500
2000
1500
1000
500
0
22
23
24
25
26
27
28
29
30
LN[P266(z)z2]
266 nm
289 nm

Fig.5

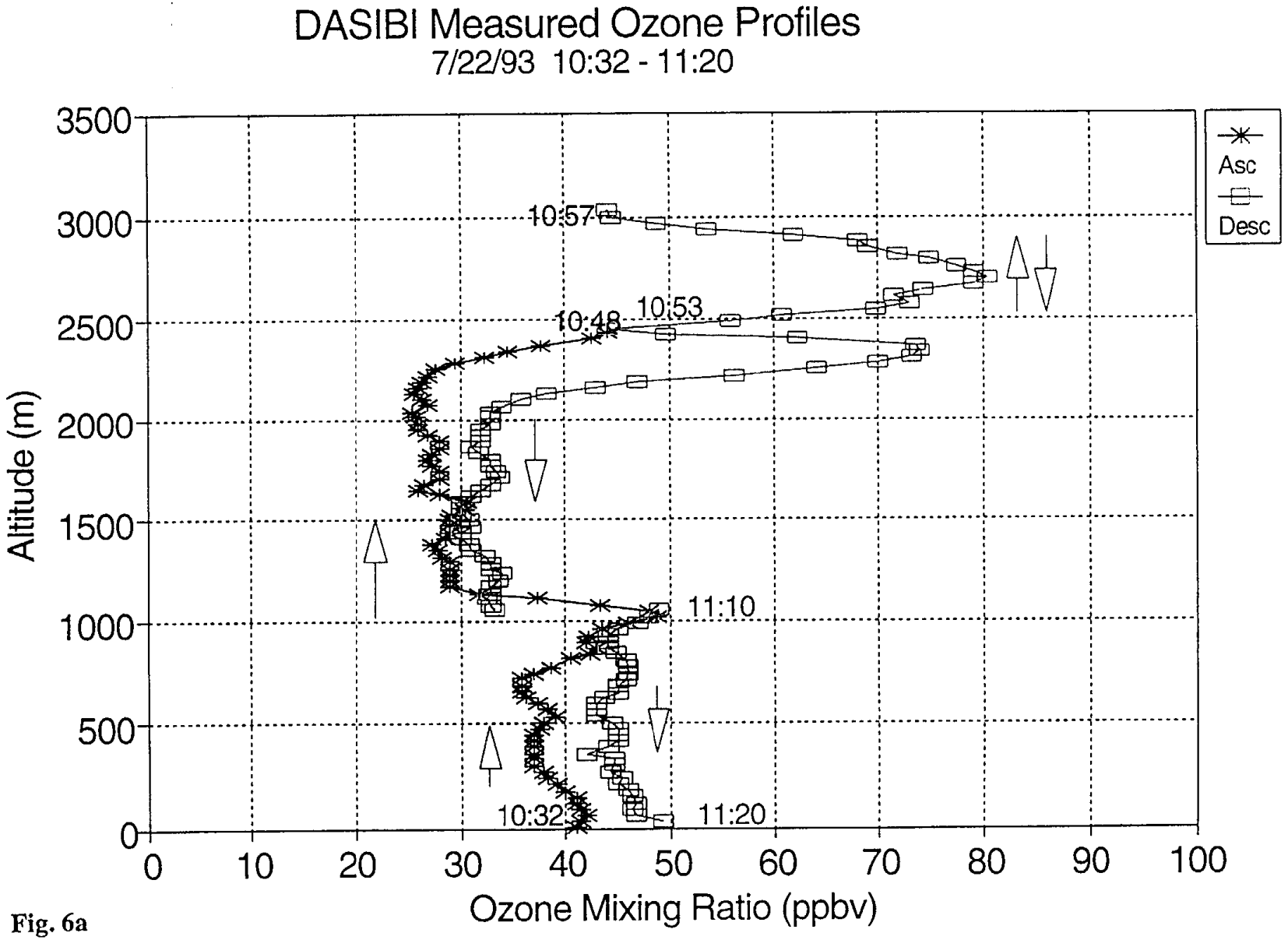
DASIBI Measured Ozone Profiles
7/22/93 10:32 - 11:20
Altitude (m)
Ozone Mixing Ratio (ppbv)
Asc
Desc
10:57
10:53
10:48
11:10
10:32
11:20
0
500
1000
1500
2000
2500
3000
3500
0
10
20
30
40
50
60
70
80
90
100

Fig. 6a

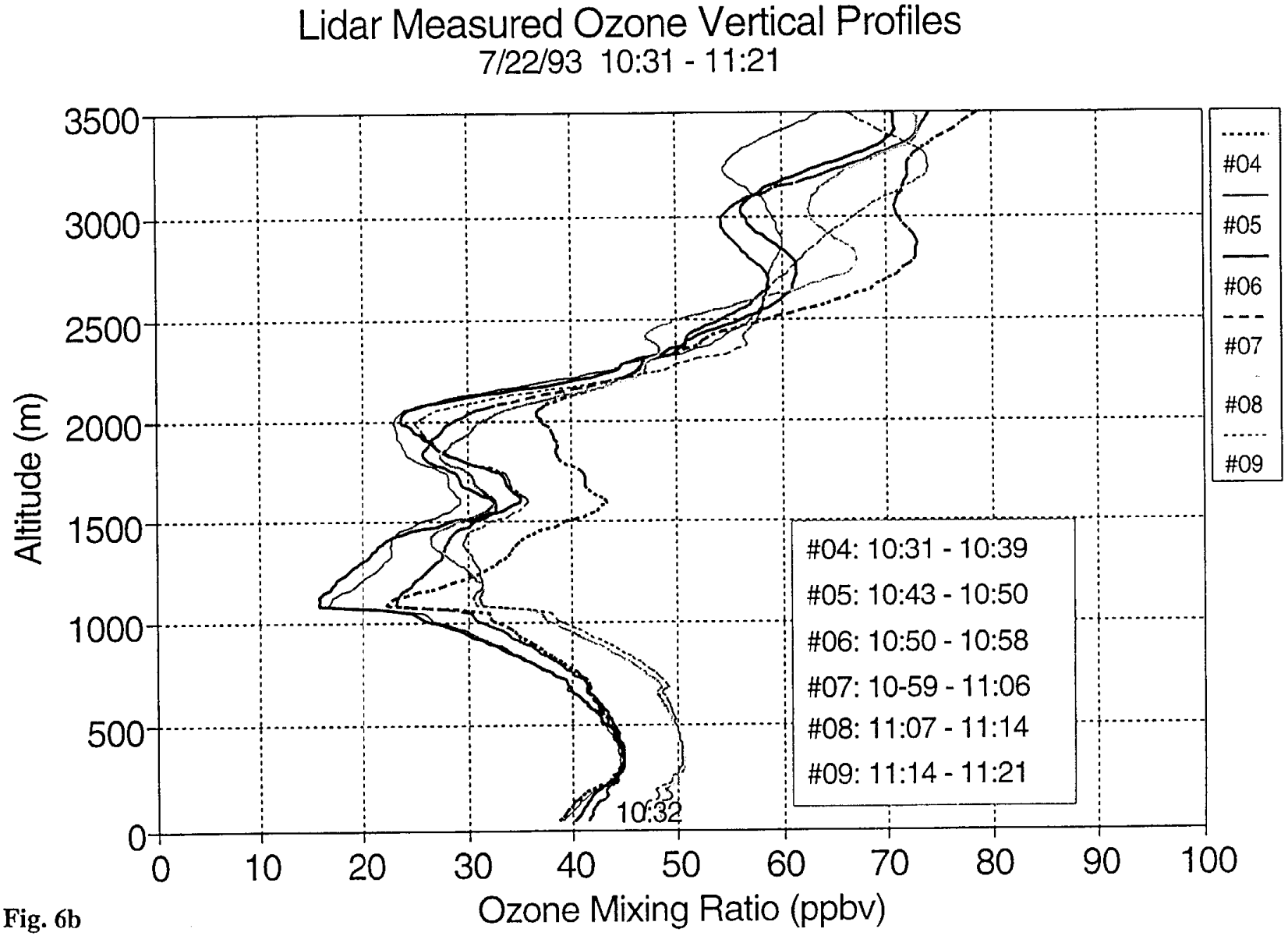
Lidar Measured Ozone Vertical Profiles
7/22/93 10:31 - 11:21
Altitude (m)
3500
3000
2500
2000
1500
1000
500
0
0
10
20
30
40
50
60
70
80
90
100
Ozone Mixing Ratio (ppbv)
#04
#05
#06
#07
#08
#09
#04: 10:31 - 10:39
#05: 10:43 - 10:50
#06: 10:50 - 10:58
#07: 10-59 - 11:06
#08: 11:07 - 11:14
#09: 11:14 - 11:21
10:32

Fig. 6b

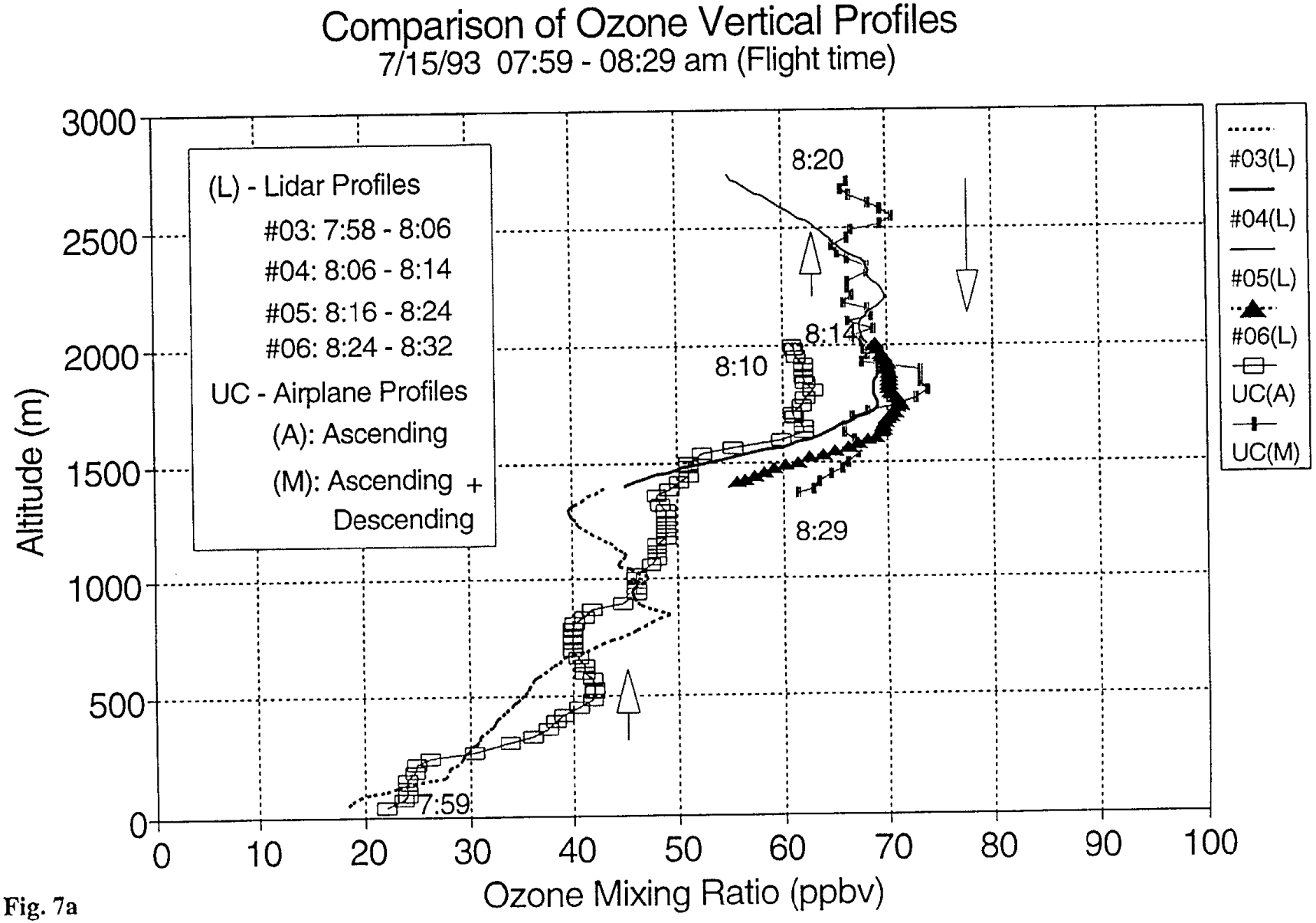
Comparison of Ozone Vertical Profiles
7/15/93 07:59 - 08:29 am (Flight time)
(L) - Lidar Profiles
#03: 7:58 - 8:06
#04: 8:06 - 8:14
#05: 8:16 - 8:24
#06: 8:24 - 8:32
UC - Airplane Profiles
(A): Ascending
(M): Ascending + Descending
8:20
8:14
8:10
8:29
7:59
#03(L)
#04(L)
#05(L)
#06(L)
UC(A)
UC(M)
Altitude (m)
Ozone Mixing Ratio (ppbv)
0
500
1000
1500
2000
2500
3000
0
10
20
30
40
50
60
70
80
90
100

Fig. 7a

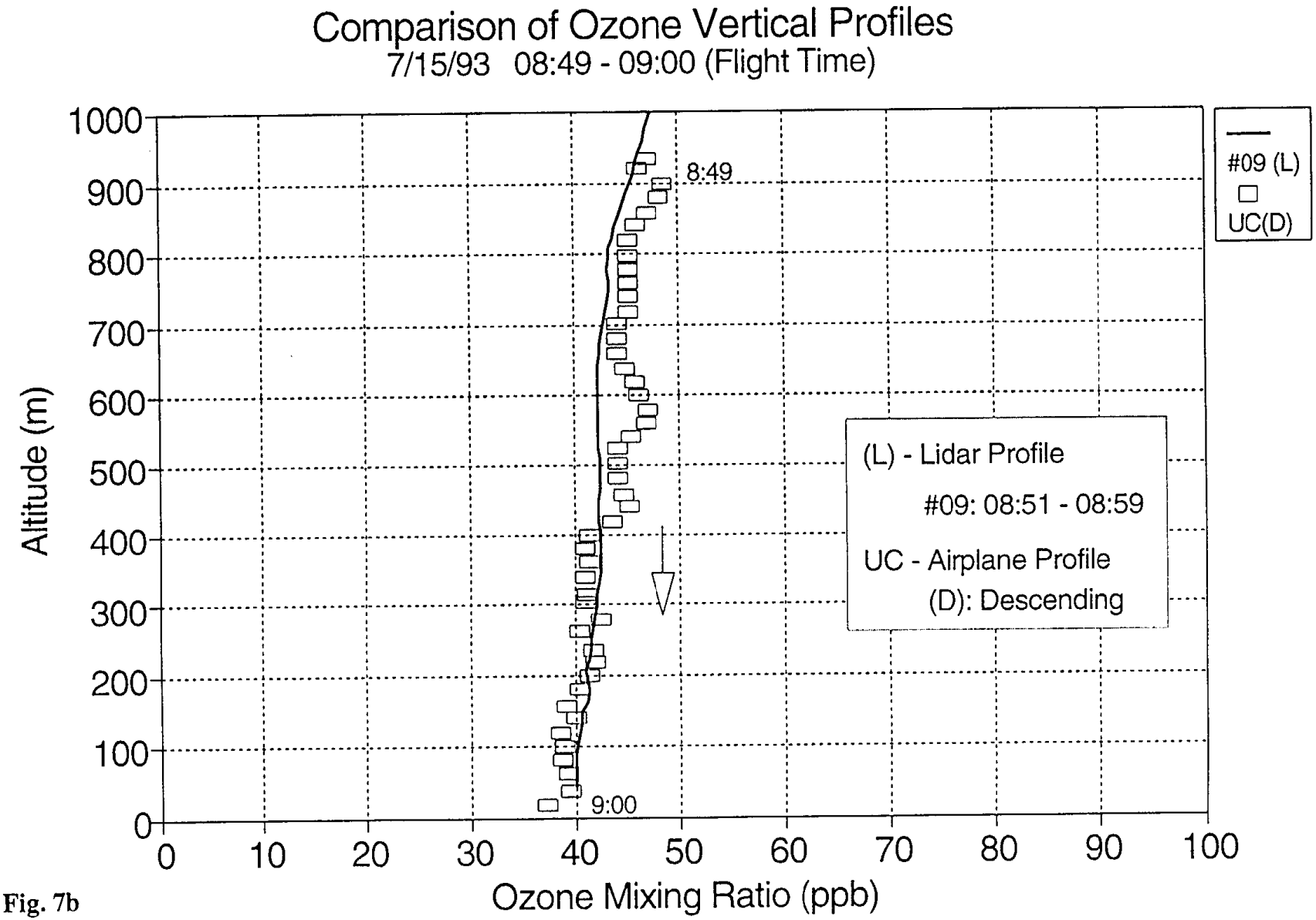
Comparison of Ozone Vertical Profiles
7/15/93 08:49 - 09:00 (Flight Time)
Altitude (m)
1000
900
800
700
600
500
400
300
200
100
0
0
10
20
30
40
50
60
70
80
90
100
Ozone Mixing Ratio (ppb)
8:49
9:00
#09 (L)
UC(D)
(L) - Lidar Profile
#09: 08:51 - 08:59
UC - Airplane Profile
(D): Descending

Fig. 7b

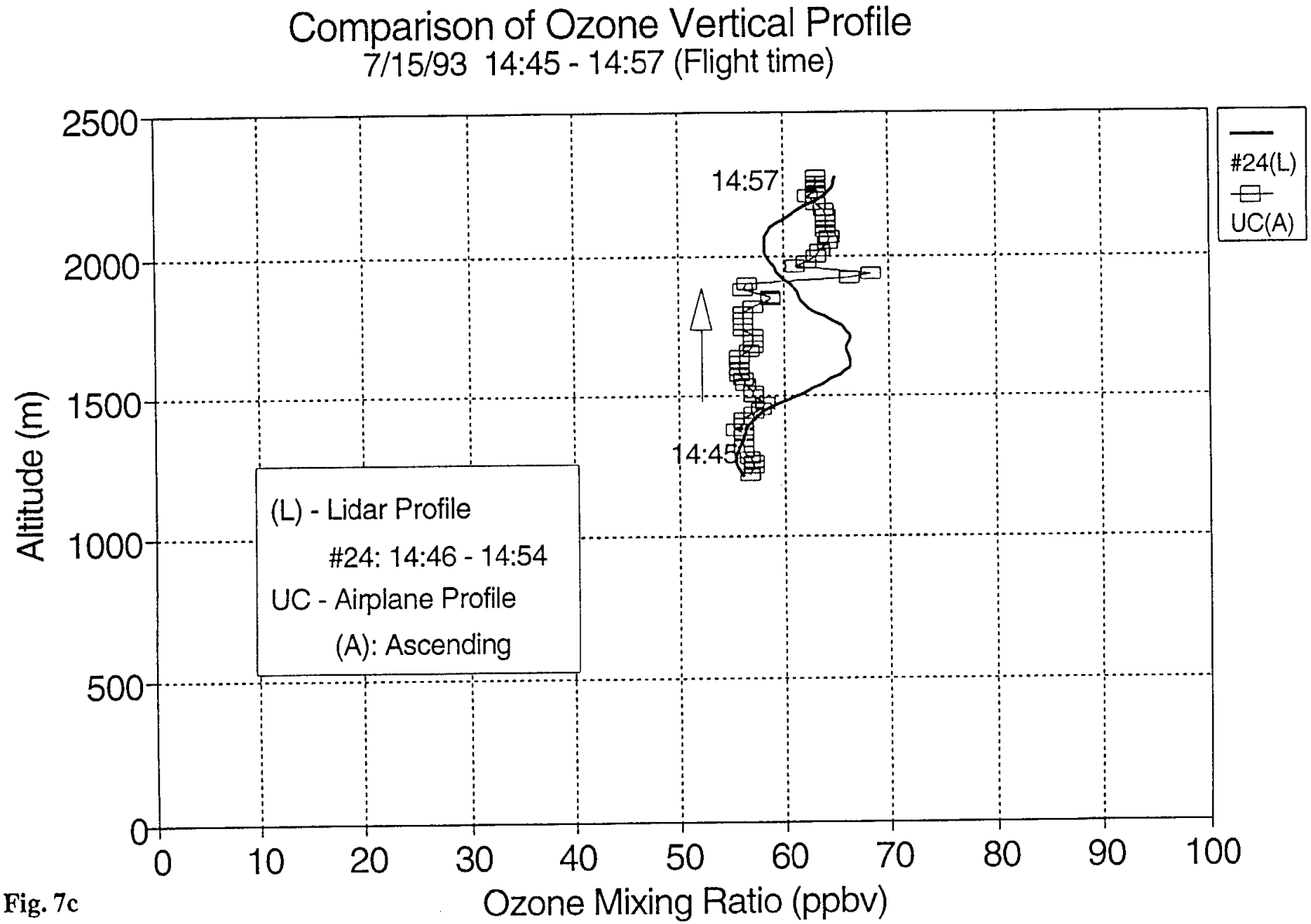
Comparison of Ozone Vertical Profile
7/15/93 14:45 - 14:57 (Flight time)
Altitude (m)
2500
2000
1500
1000
500
0
0
10
20
30
40
50
60
70
80
90
100
Ozone Mixing Ratio (ppbv)
14:57
14:45
#24(L)
UC(A)
(L) - Lidar Profile
#24: 14:46 - 14:54
UC - Airplane Profile
(A): Ascending

Fig. 7c

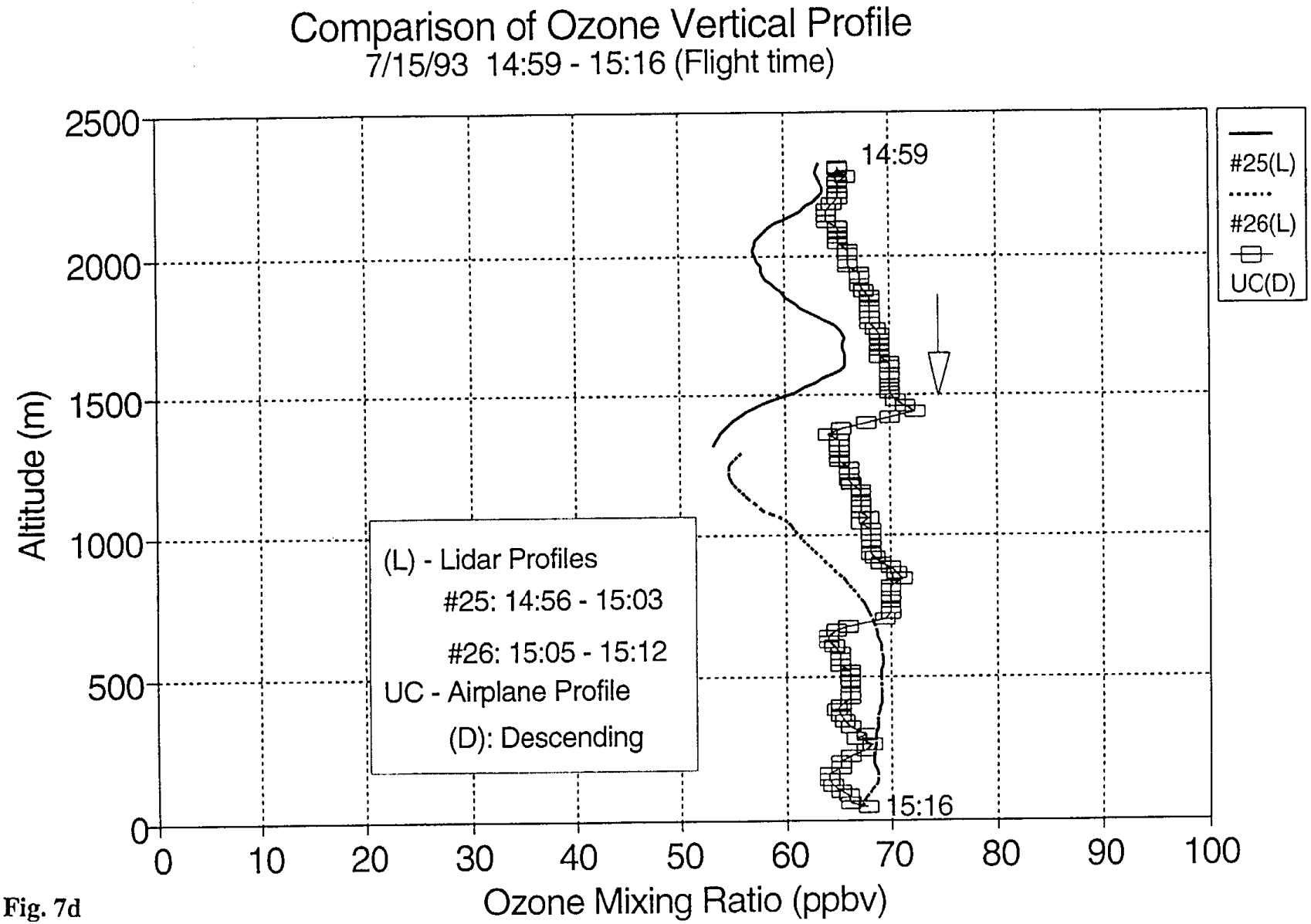
Comparison of Ozone Vertical Profile
7/15/93 14:59 - 15:16 (Flight time)
Altitude (m)
2500
2000
1500
1000
500
0
0
10
20
30
40
50
60
70
80
90
100
Ozone Mixing Ratio (ppbv)
14:59
15:16
#25(L)
#26(L)
UC(D)
(L) - Lidar Profiles
#25: 14:56 - 15:03
#26: 15:05 - 15:12
UC - Airplane Profile
(D): Descending

Fig. 7d

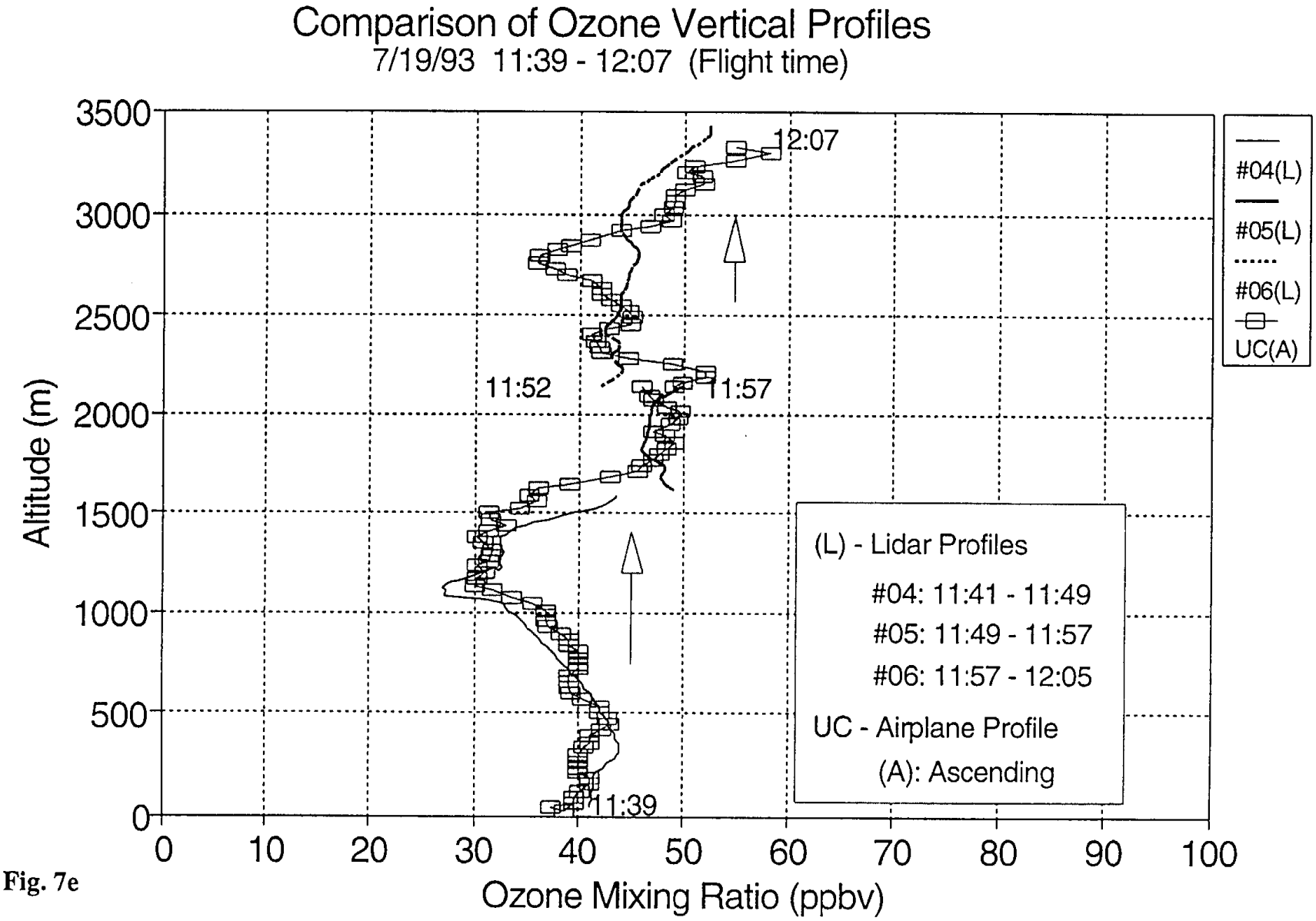
Comparison of Ozone Vertical Profiles
7/19/93 11:39 - 12:07 (Flight time)
Altitude (m)
Ozone Mixing Ratio (ppbv)
0
500
1000
1500
2000
2500
3000
3500
0
10
20
30
40
50
60
70
80
90
100
12:07
11:52
11:57
11:39
#04(L)
#05(L)
#06(L)
UC(A)
(L) - Lidar Profiles
#04: 11:41 - 11:49
#05: 11:49 - 11:57
#06: 11:57 - 12:05
UC - Airplane Profile
(A): Ascending

Fig. 7e

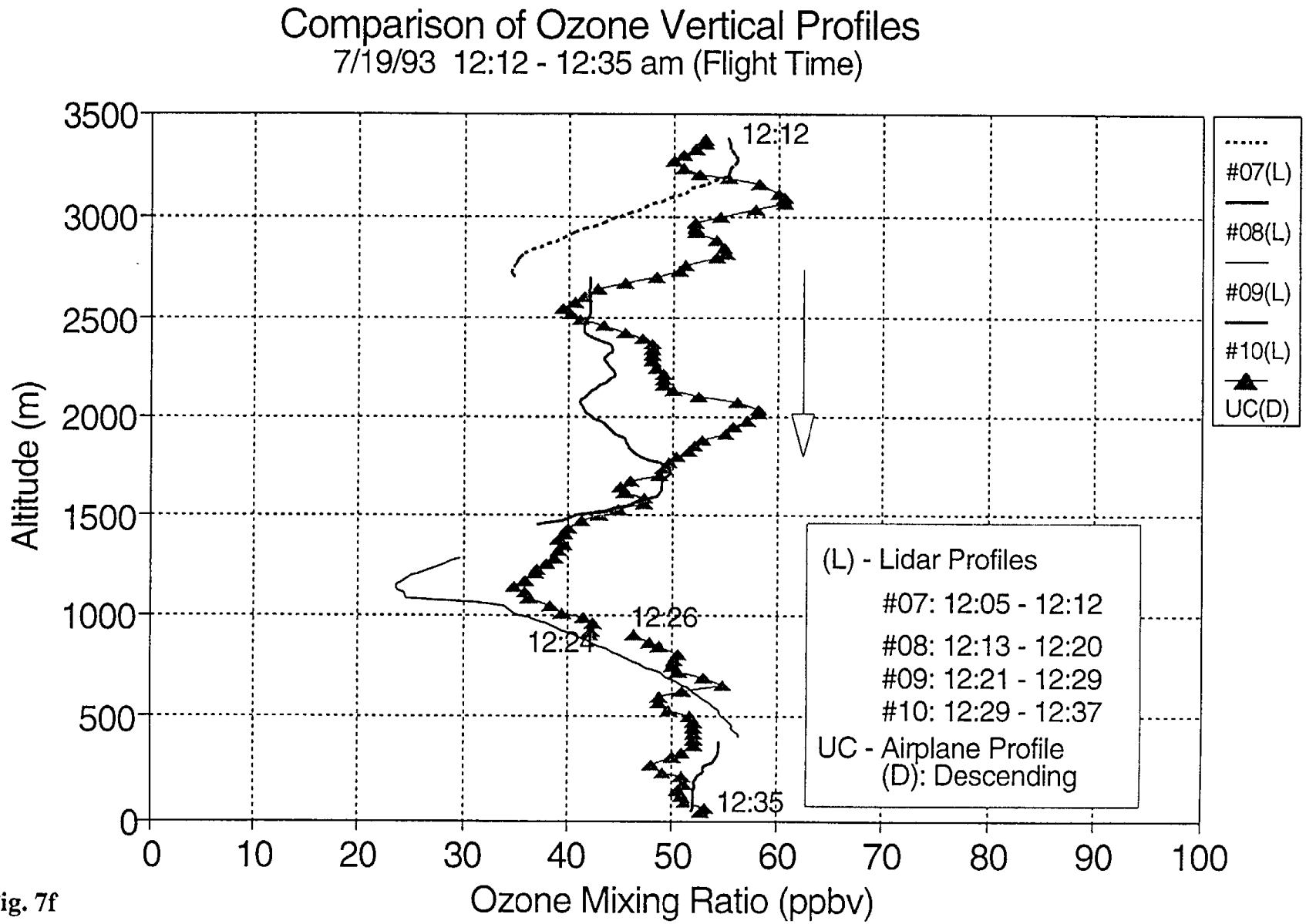
Comparison of Ozone Vertical Profiles
7/19/93 12:12 - 12:35 am (Flight Time)
Altitude (m)
Ozone Mixing Ratio (ppbv)
0
500
1000
1500
2000
2500
3000
3500
0
10
20
30
40
50
60
70
80
90
100
12:12
12:24
12:26
12:35
#07(L)
#08(L)
#09(L)
#10(L)
UC(D)
(L) - Lidar Profiles
#07: 12:05 - 12:12
#08: 12:13 - 12:20
#09: 12:21 - 12:29
#10: 12:29 - 12:37
UC - Airplane Profile
(D): Descending

Fig. 7f

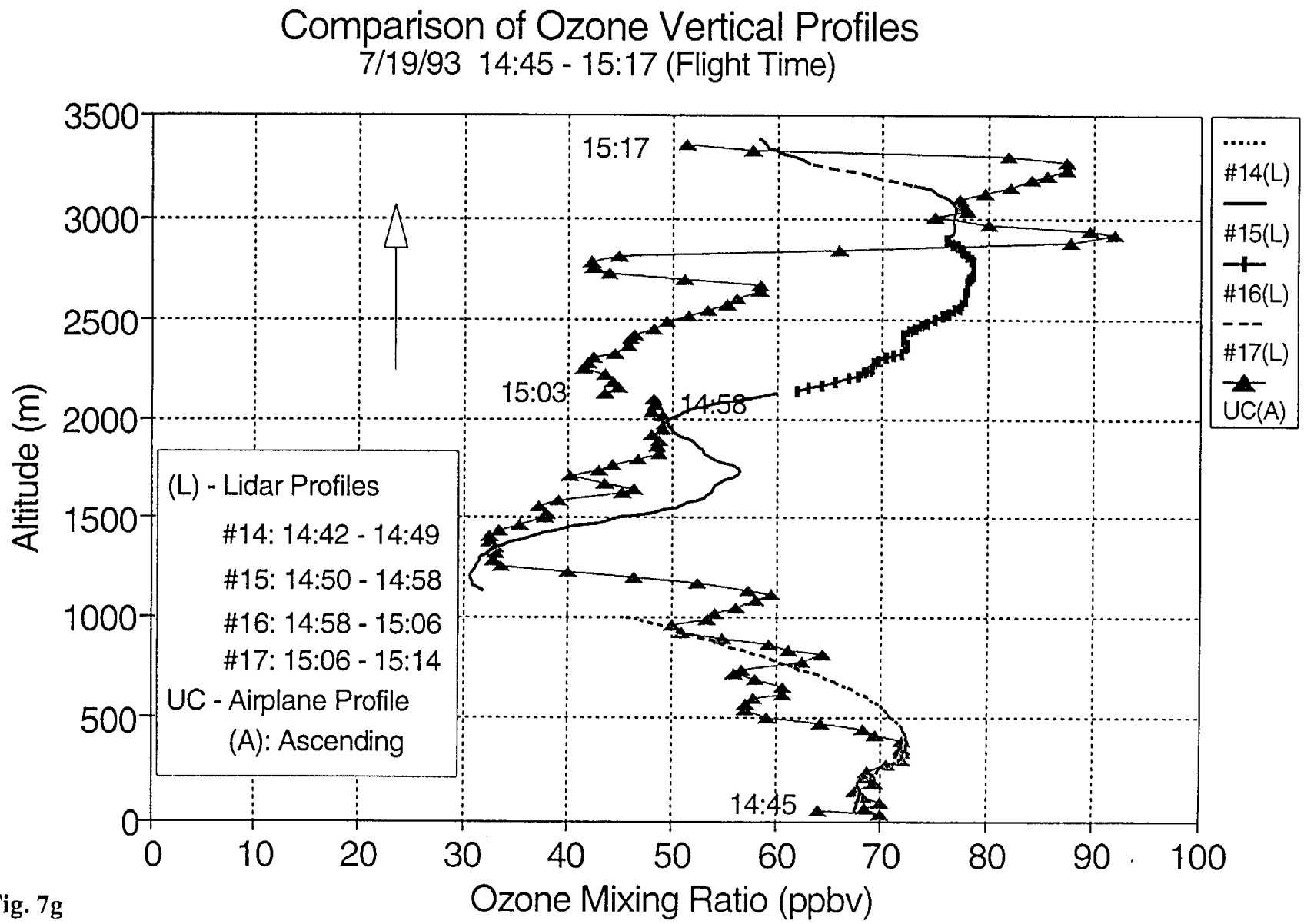
Comparison of Ozone Vertical Profiles
7/19/93 14:45 - 15:17 (Flight Time)
Altitude (m)
Ozone Mixing Ratio (ppbv)
3500
3000
2500
2000
1500
1000
500
0
0
10
20
30
40
50
60
70
80
90
100
15:17
15:03
14:58
14:45
(L) - Lidar Profiles
#14: 14:42 - 14:49
#15: 14:50 - 14:58
#16: 14:58 - 15:06
#17: 15:06 - 15:14
UC - Airplane Profile
(A): Ascending
#14(L)
#15(L)
#16(L)
#17(L)
UC(A)

Fig. 7g

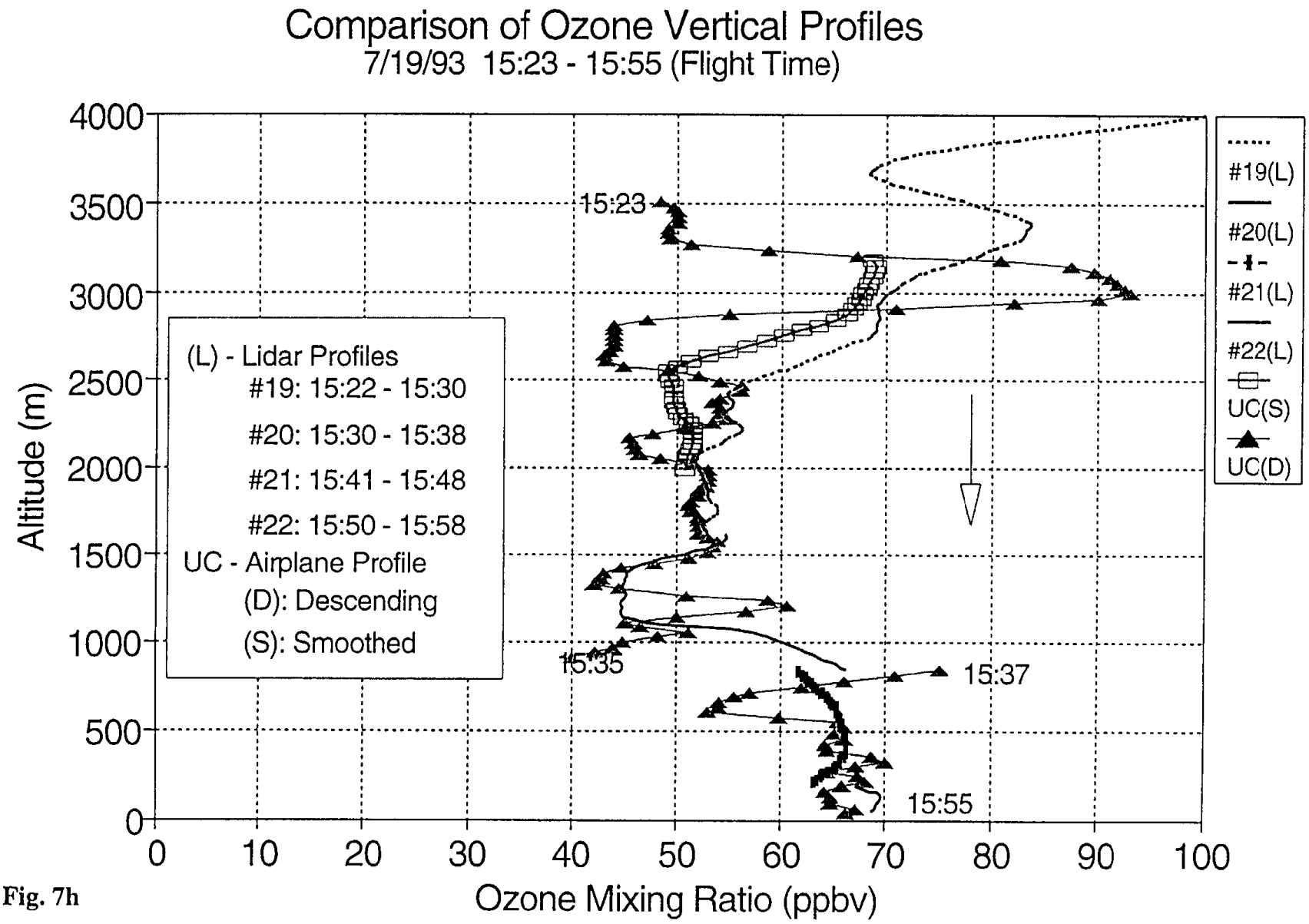
Comparison of Ozone Vertical Profiles
7/19/93 15:23 - 15:55 (Flight Time)
Altitude (m)
4000
3500
3000
2500
2000
1500
1000
500
0
0
10
20
30
40
50
60
70
80
90
100
Ozone Mixing Ratio (ppbv)
(L) - Lidar Profiles
#19: 15:22 - 15:30
#20: 15:30 - 15:38
#21: 15:41 - 15:48
#22: 15:50 - 15:58
UC - Airplane Profile
(D): Descending
(S): Smoothed
15:23
15:35
15:37
15:55
#19(L)
#20(L)
#21(L)
#22(L)
UC(S)
UC(D)

Fig. 7h

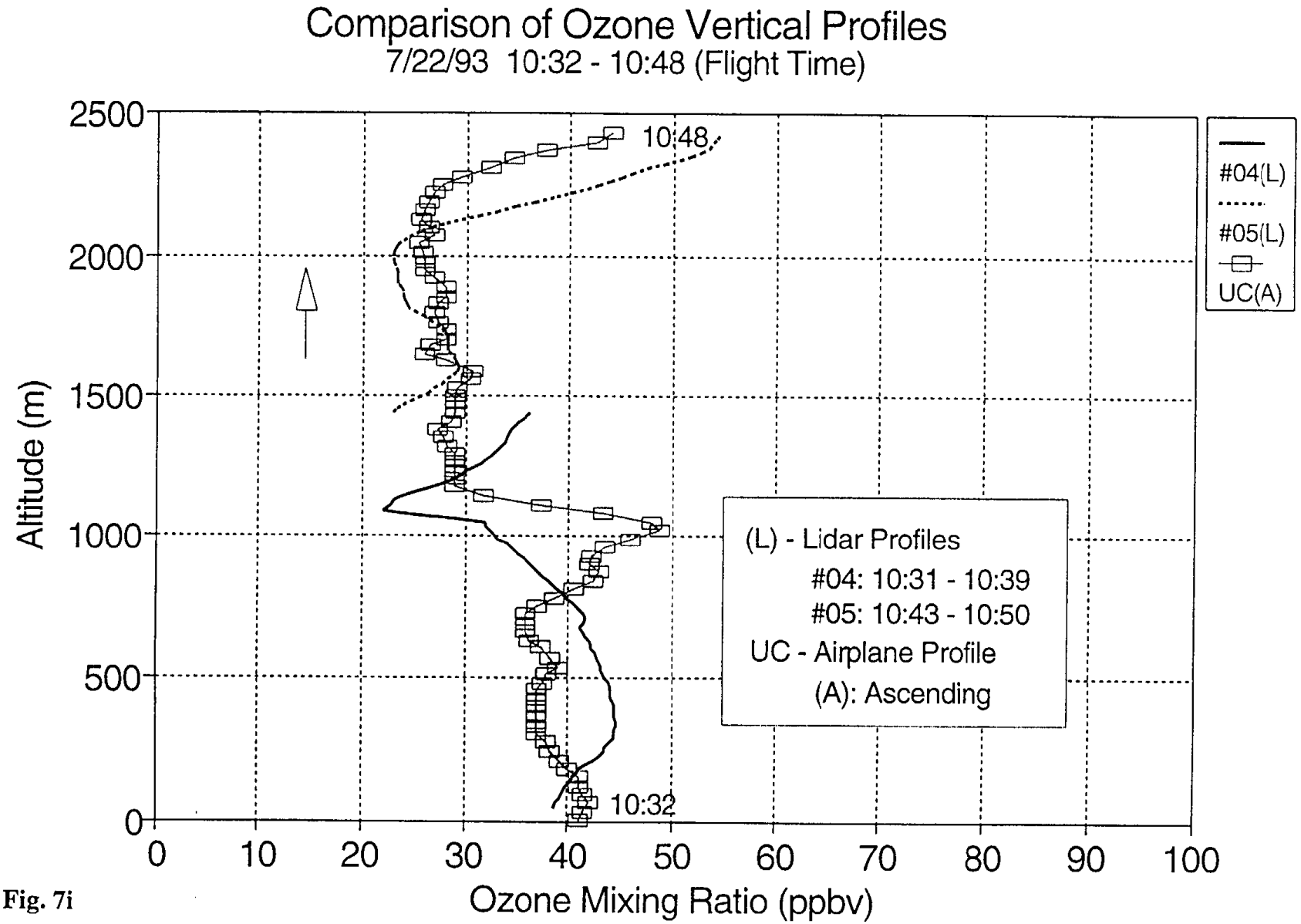
Comparison of Ozone Vertical Profiles
7/22/93 10:32 - 10:48 (Flight Time)
Altitude (m)
2500
2000
1500
1000
500
0
0
10
20
30
40
50
60
70
80
90
100
Ozone Mixing Ratio (ppbv)
10:48
10:32
#04(L)
#05(L)
UC(A)
(L) - Lidar Profiles
#04: 10:31 - 10:39
#05: 10:43 - 10:50
UC - Airplane Profile
(A): Ascending

Fig. 7i

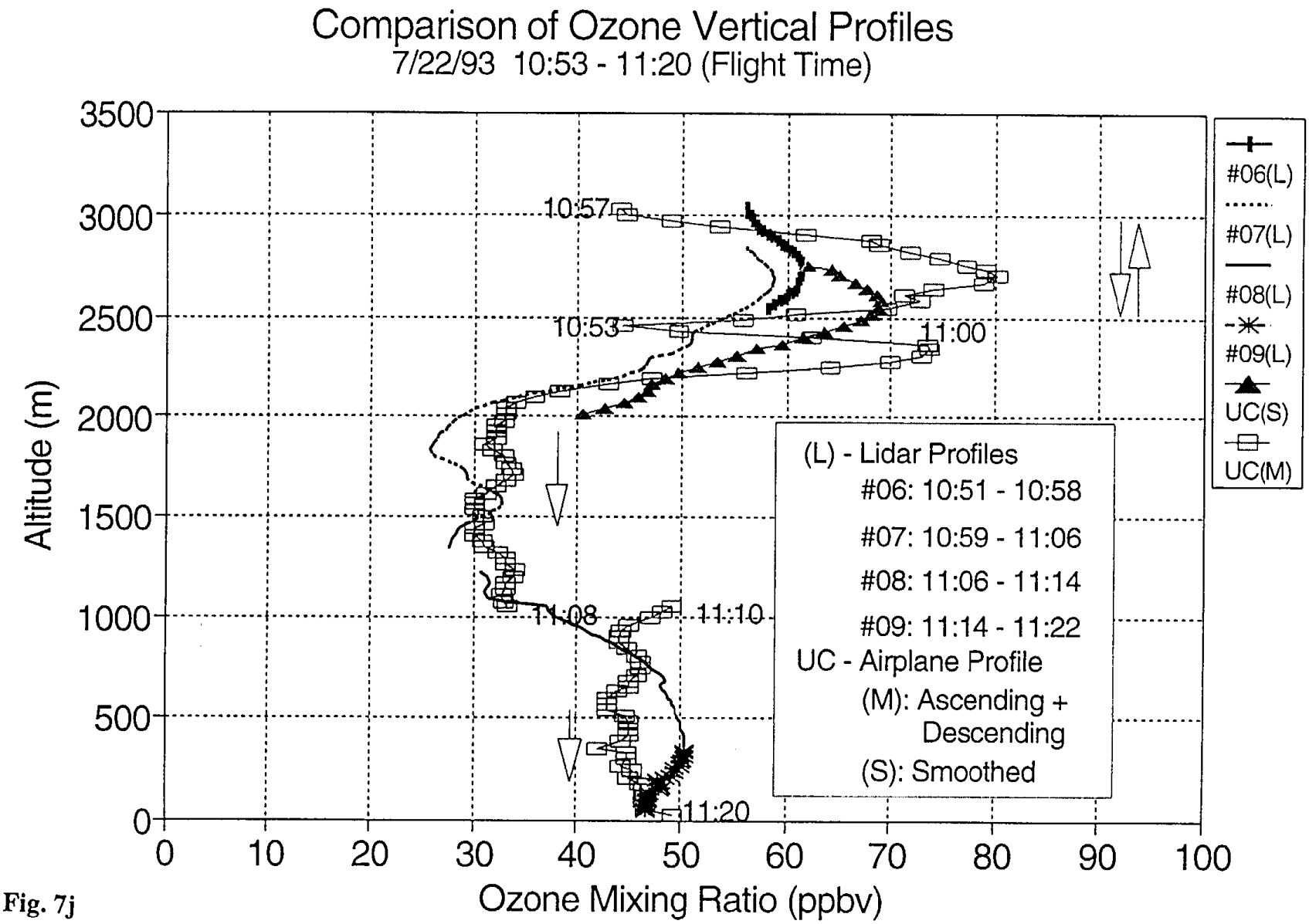
Comparison of Ozone Vertical Profiles
7/22/93 10:53 - 11:20 (Flight Time)
Altitude (m)
Ozone Mixing Ratio (ppbv)
0
500
1000
1500
2000
2500
3000
3500
0
10
20
30
40
50
60
70
80
90
100
10:57
10:53
11:00
11:08
11:10
11:20
#06(L)
#07(L)
#08(L)
#09(L)
UC(S)
UC(M)
(L) - Lidar Profiles
#06: 10:51 - 10:58
#07: 10:59 - 11:06
#08: 11:06 - 11:14
#09: 11:14 - 11:22
UC - Airplane Profile
(M): Ascending + Descending
(S): Smoothed

Fig. 7j

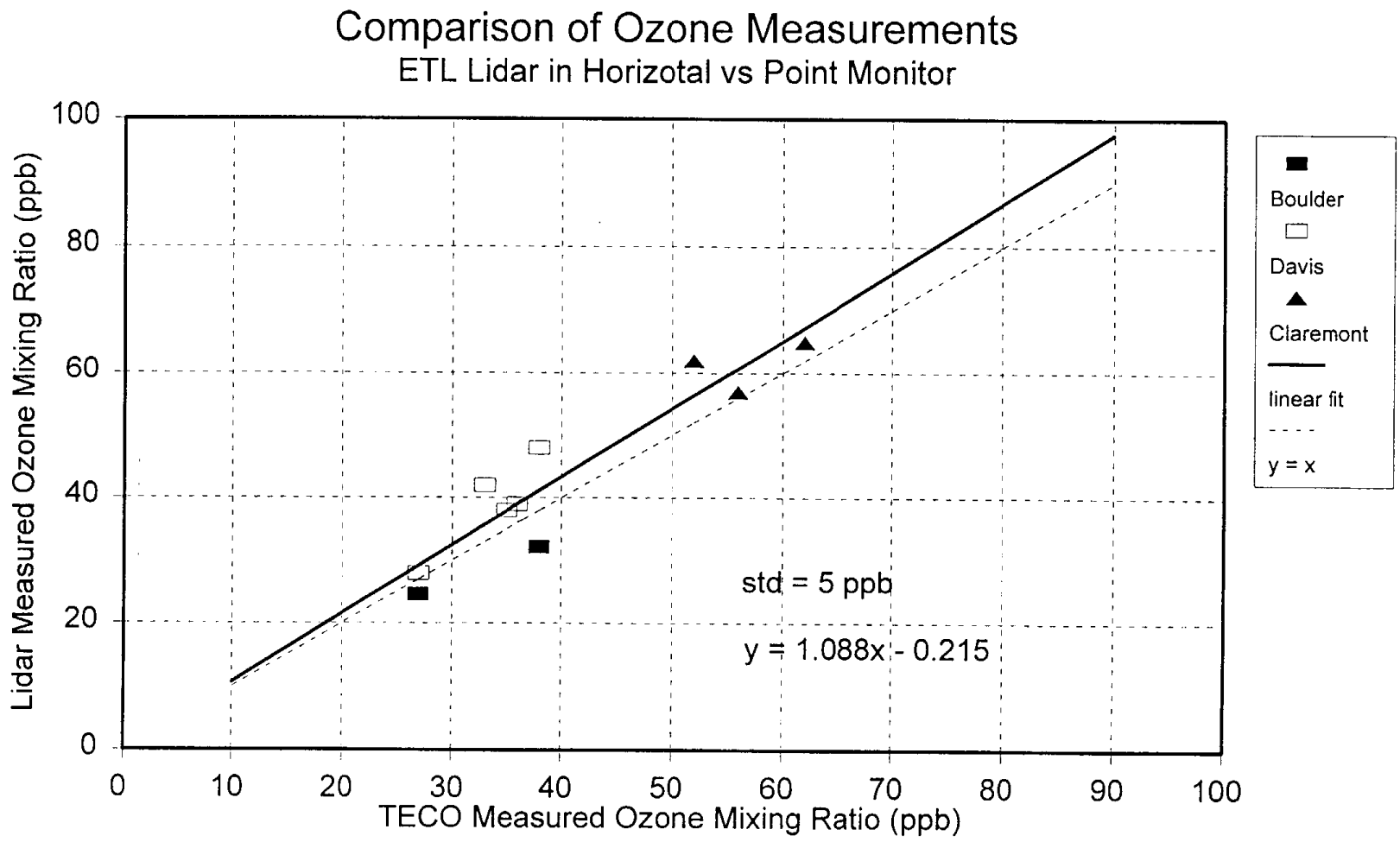
Comparison of Ozone Measurements
ETL Lidar in Horizotal vs Point Monitor
Lidar Measured Ozone Mixing Ratio (ppb)
TECO Measured Ozone Mixing Ratio (ppb)
0
20
40
60
80
100
0
10
20
30
40
50
60
70
80
90
100
std = 5 ppb
y = 1.088x - 0.215
Boulder
Davis
Claremont
linear fit
y = x

Fig. 8

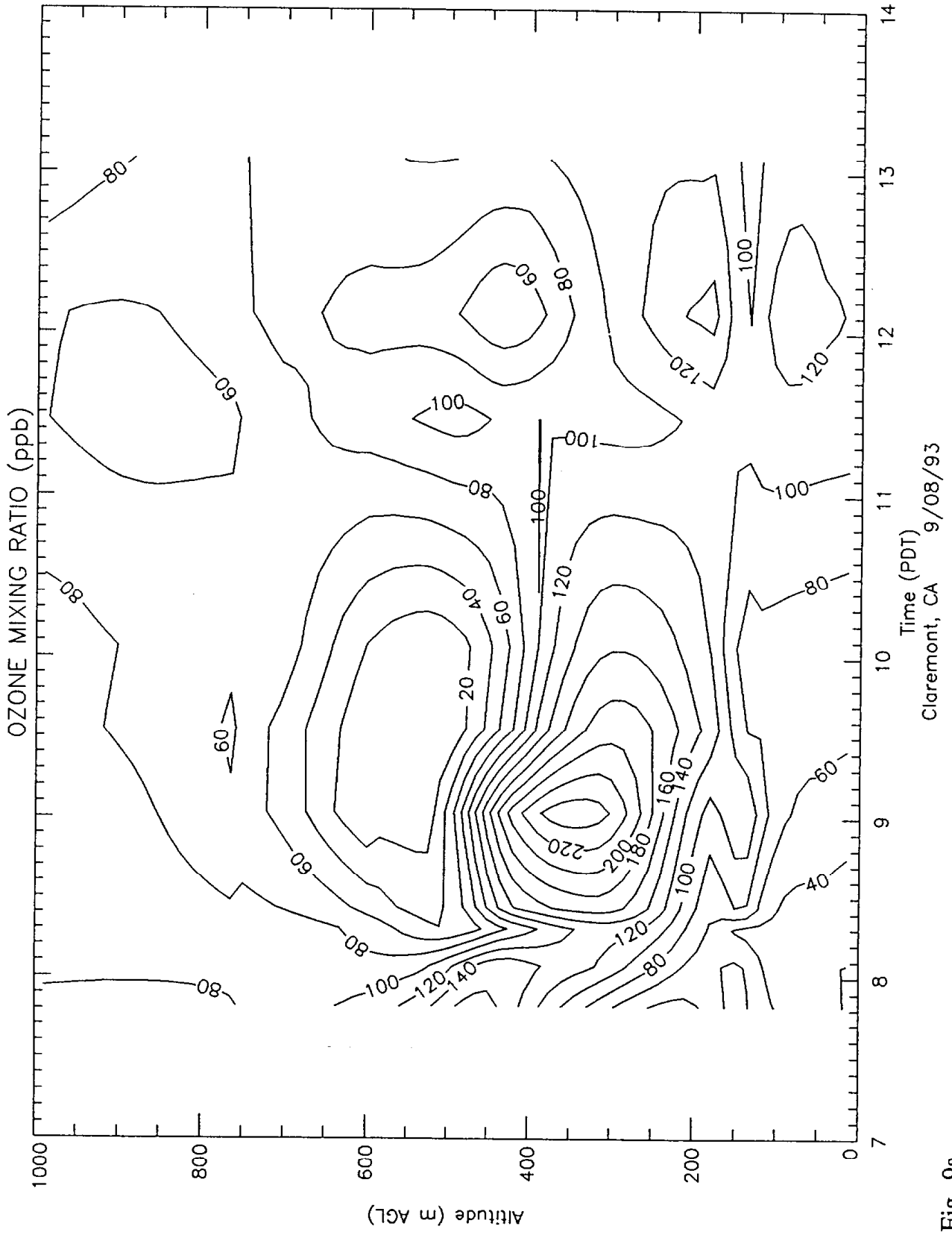
OZONE MIXING RATIO (ppb)
Altitude (m AGL)
Time (PDT)
Claremont, CA 9/08/93

Fig. 9a

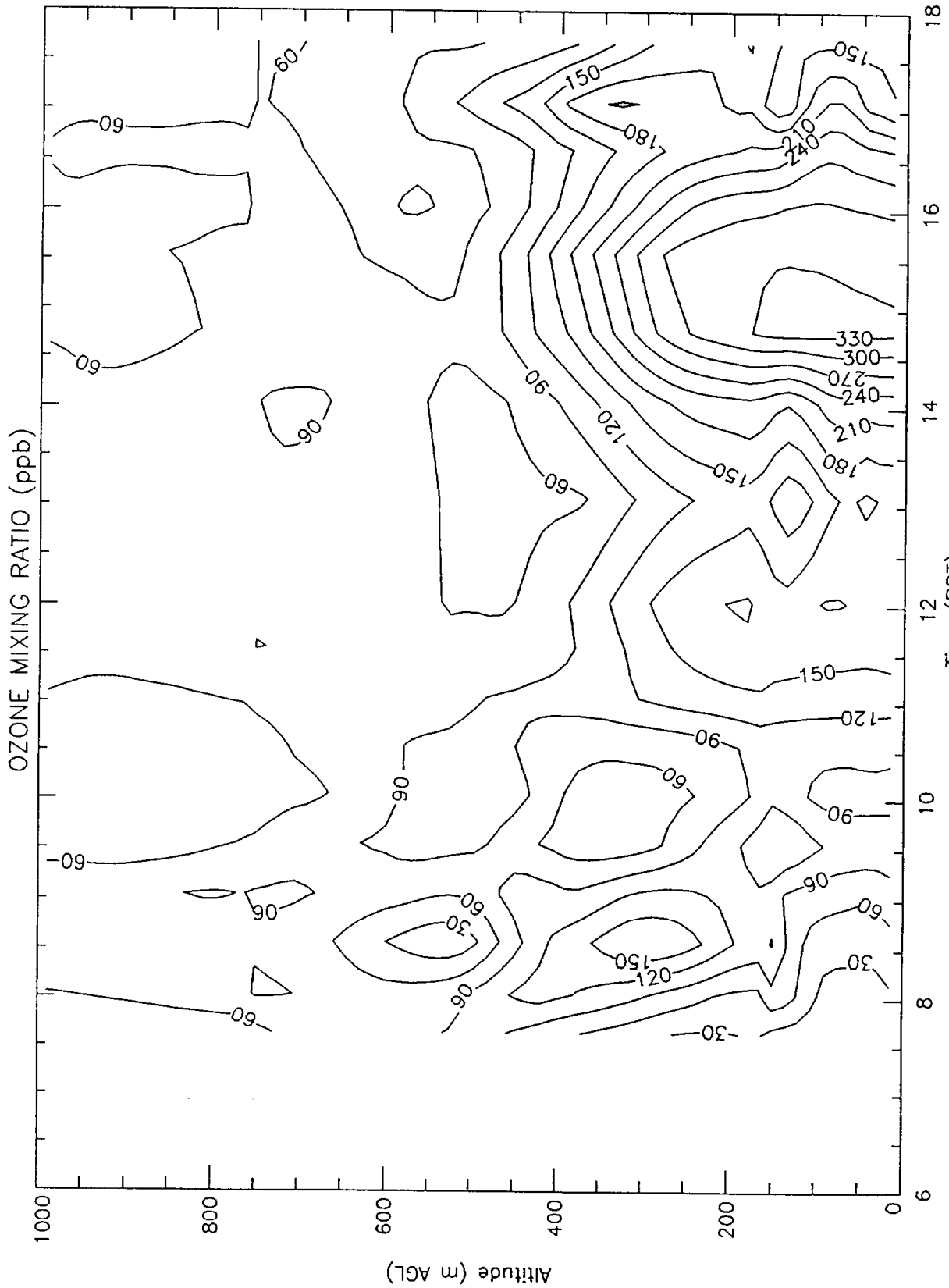
OZONE MIXING RATIO (ppb)
Altitude (m AGL)
Time (PDT)
Claremont, CA 9/09/93
0
200
400
600
800
1000
6
8
10
12
14
16
18
30
60
90
120
150
180
210
240
270
300
330

Fig. 9b

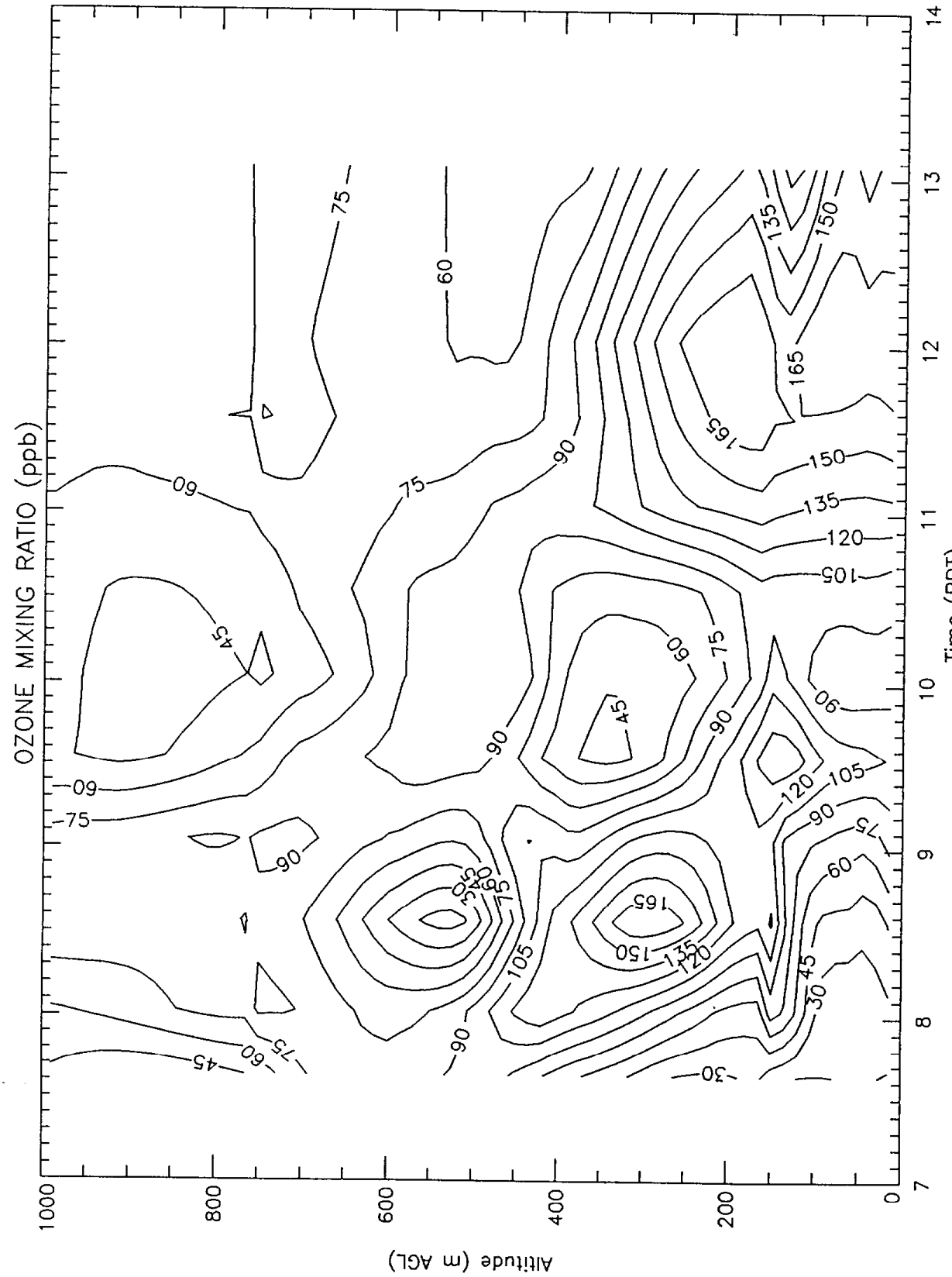
OZONE MIXING RATIO (ppb)
Altitude (m AGL)
Time (PDT)
Claremont, CA 9/09/93

Fig. 9c

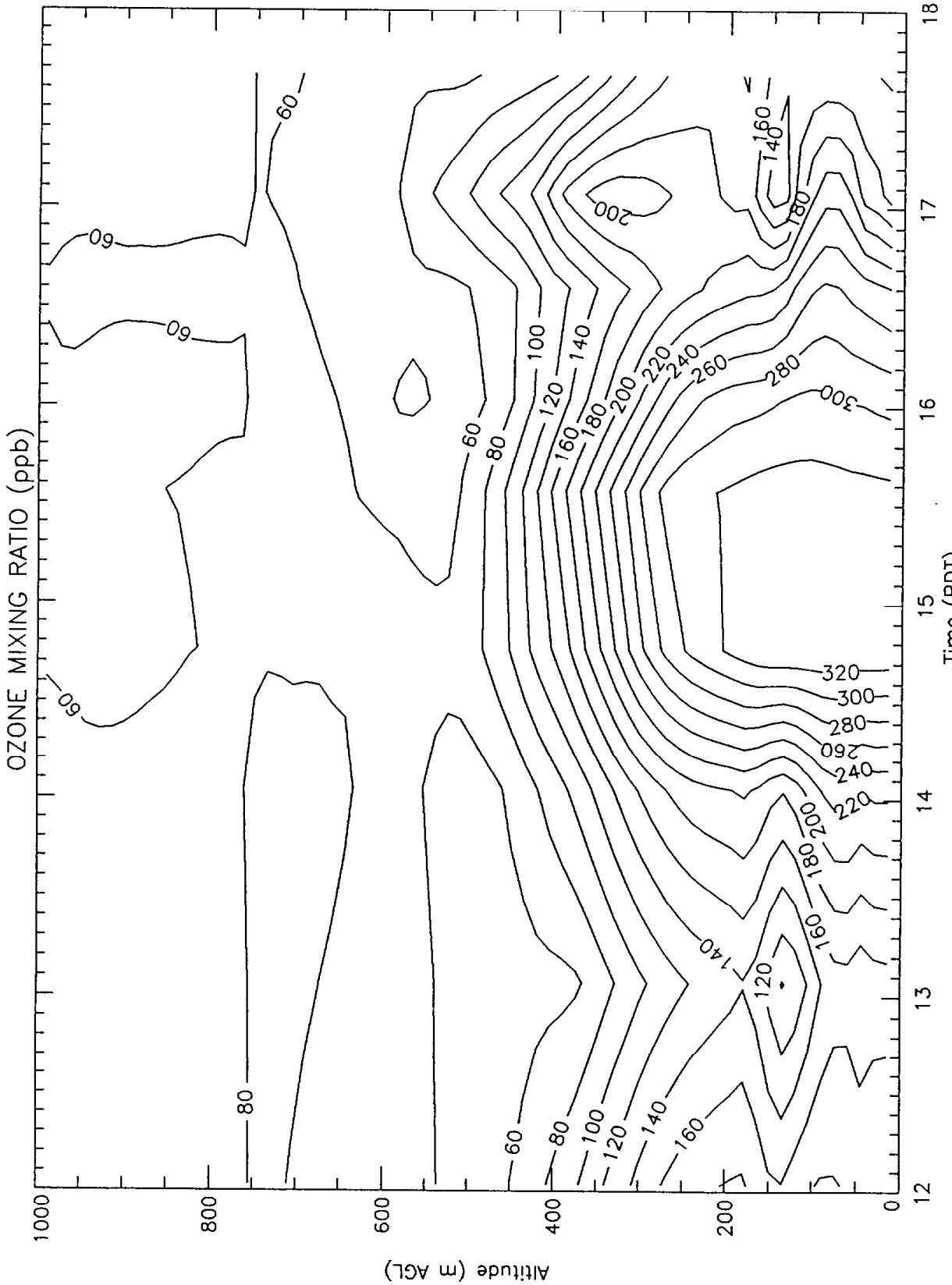
OZONE MIXING RATIO (ppb)
Altitude (m AGL)
Time (PDT)
Claremont, CA 9/09/93

Fig. 9d

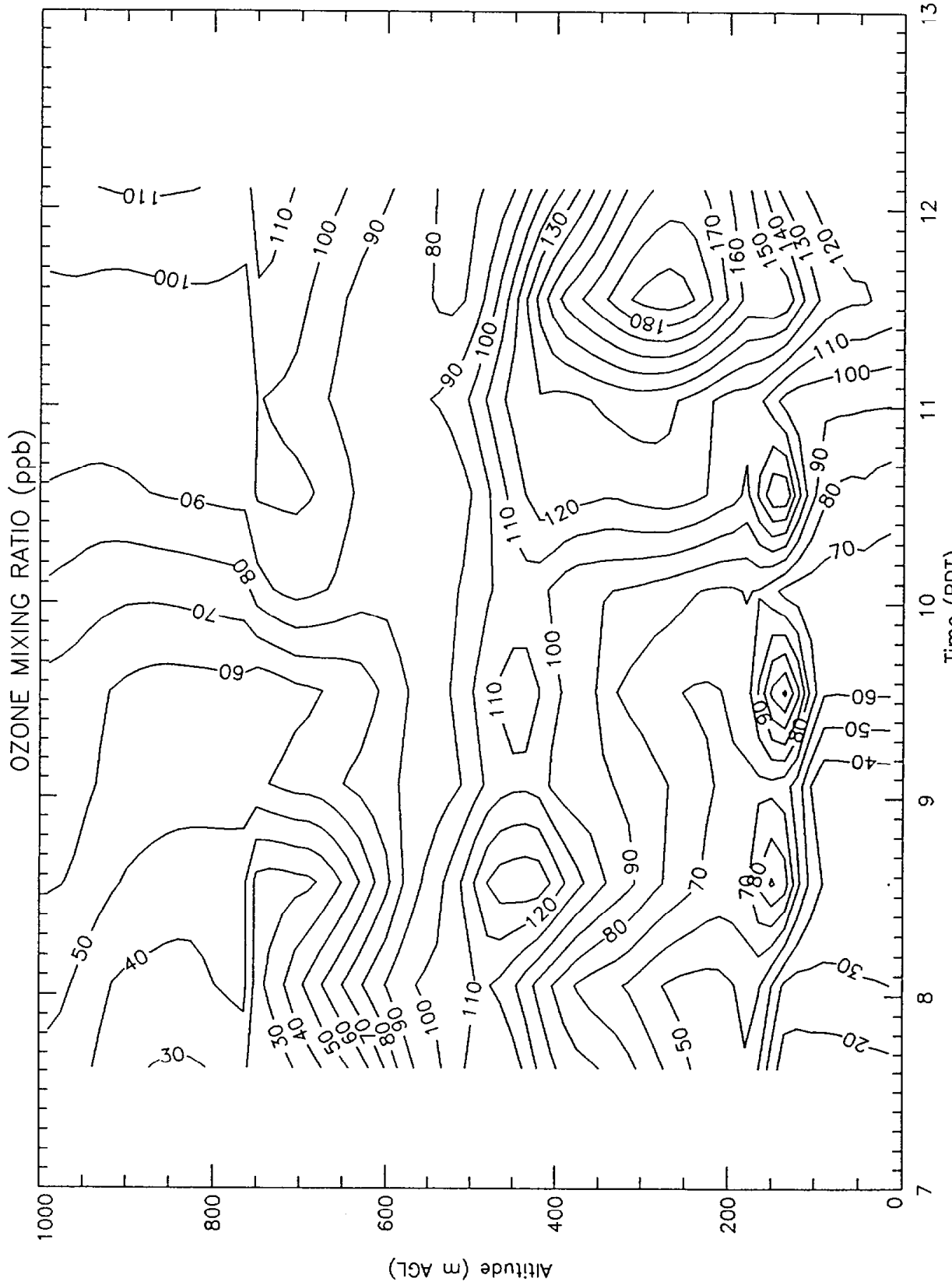
OZONE MIXING RATIO (ppb)
Altitude (m AGL)
Time (PDT)
Claremont, CA 9/10/93

Fig. 9e

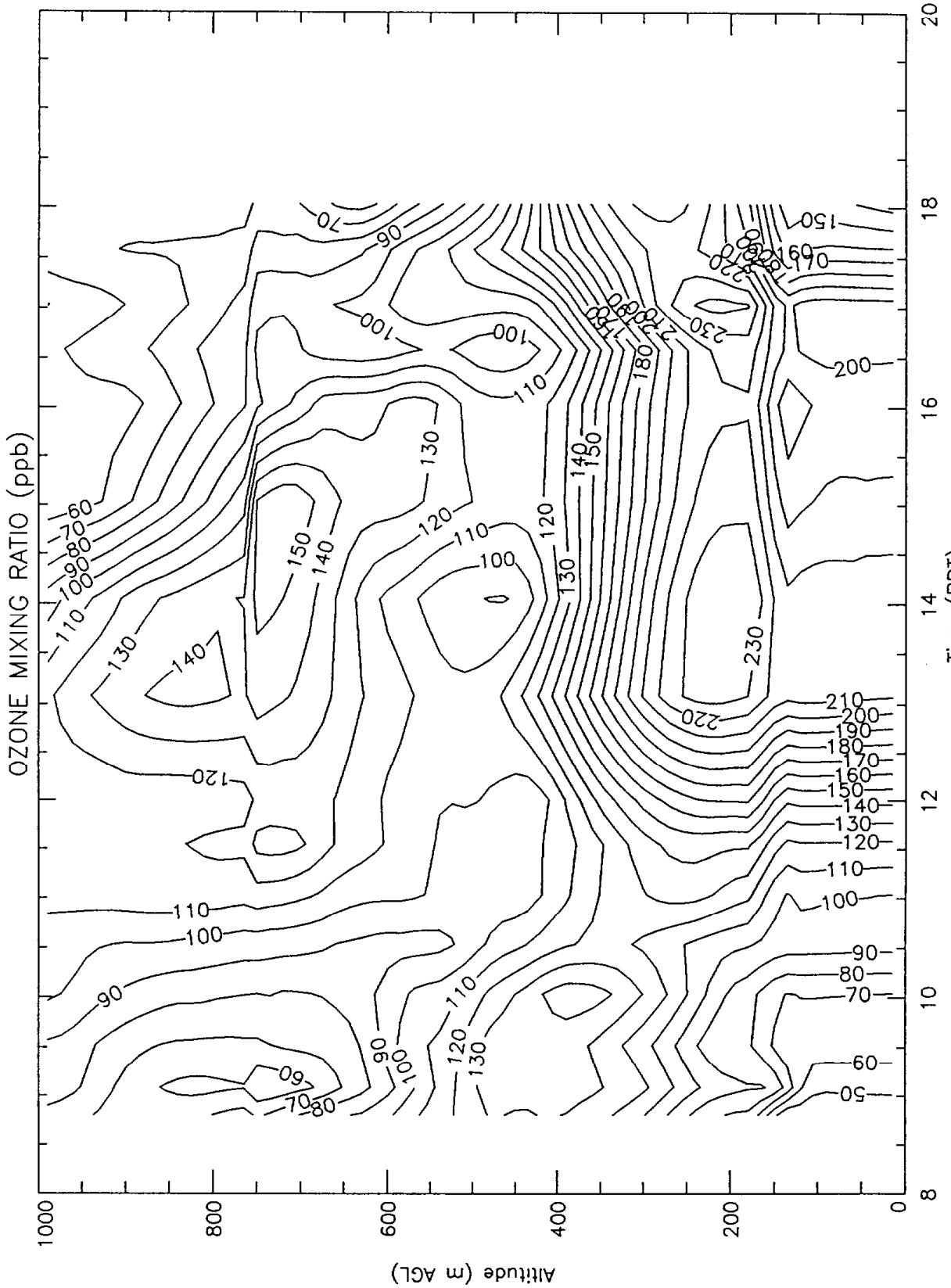
OZONE MIXING RATIO (ppb)
Altitude (m AGL)
Time (PDT)
Claremont, CA 9/11/93

Fig. 9f

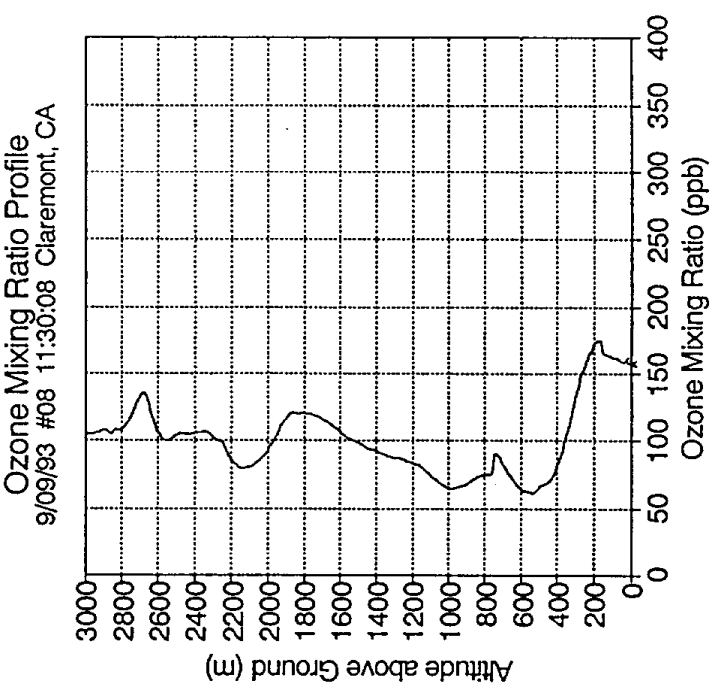

Fig. 10b

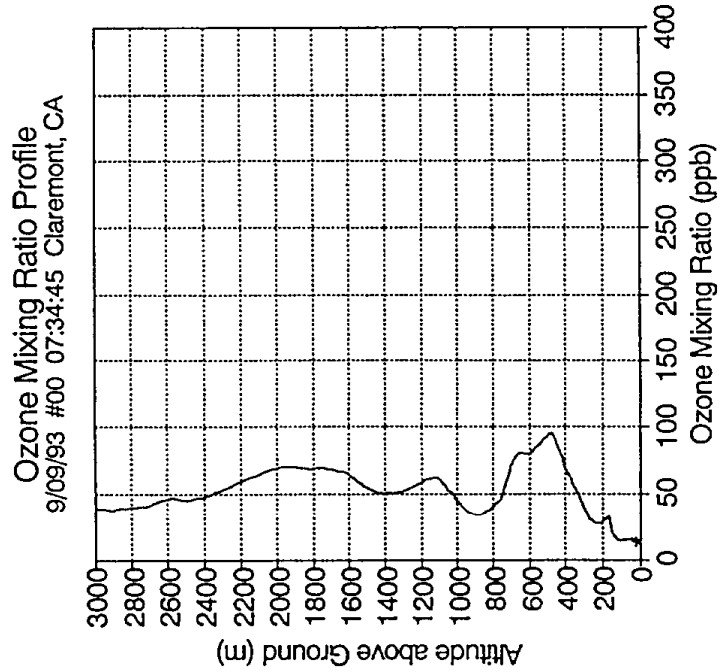

Fig. 10a

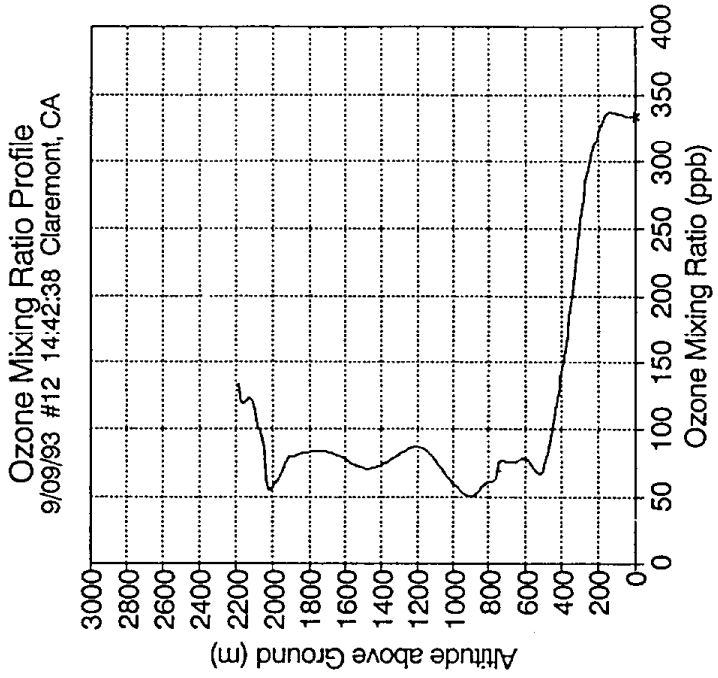

Fig.10d

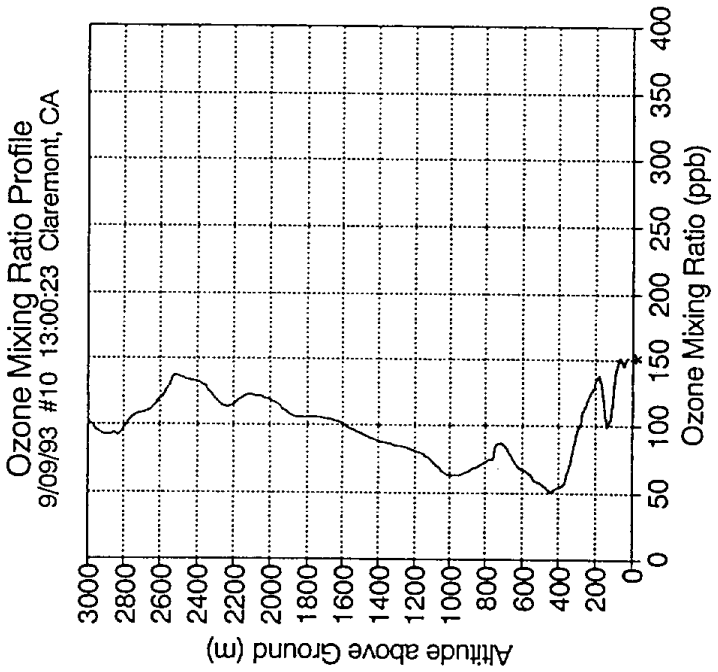

Fig. 10c

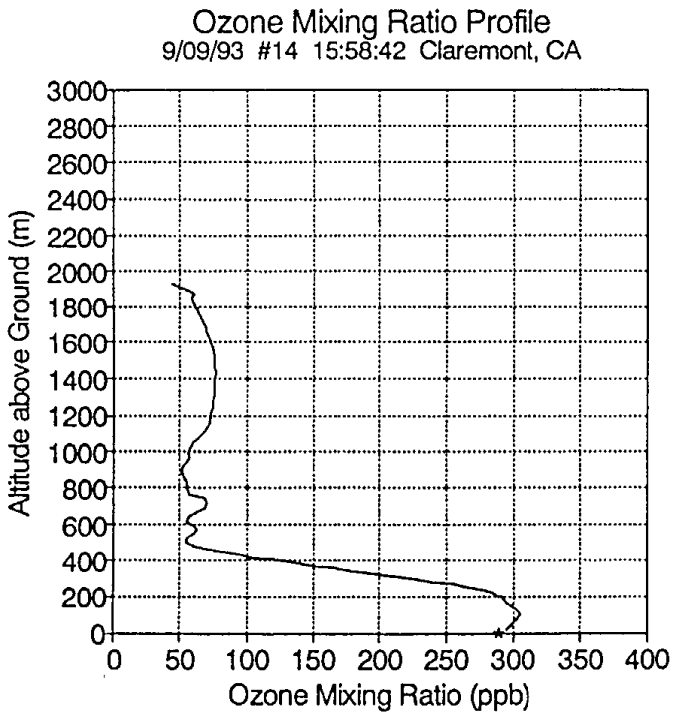

Fig.10e

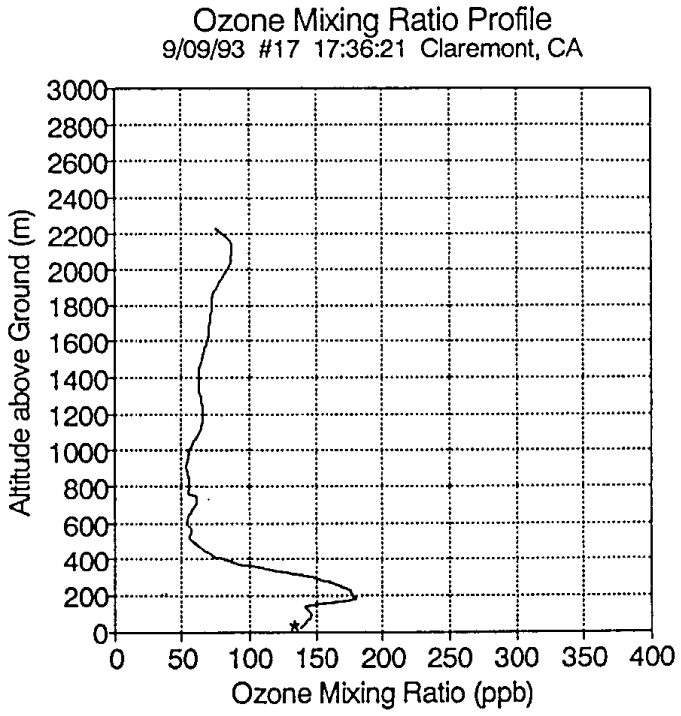

Fig. 10f

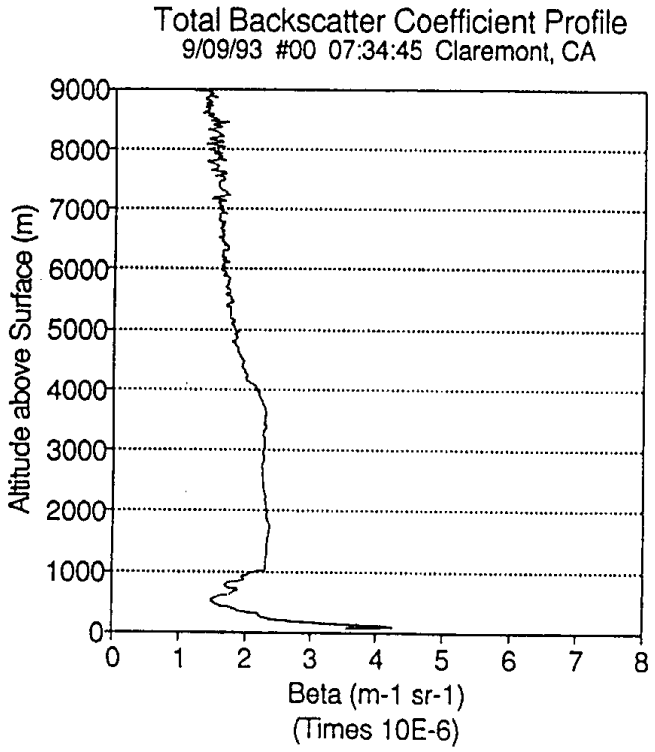

Fig. 11a

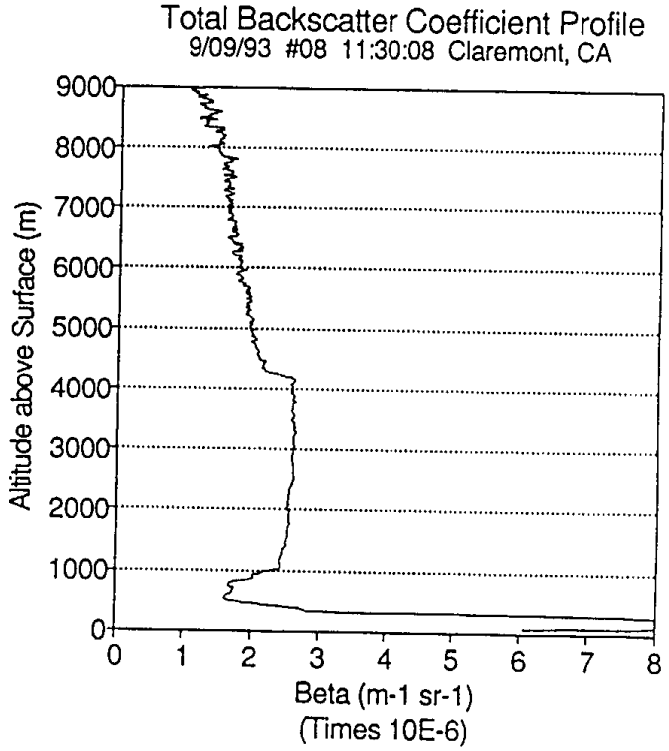

Fig. 11b

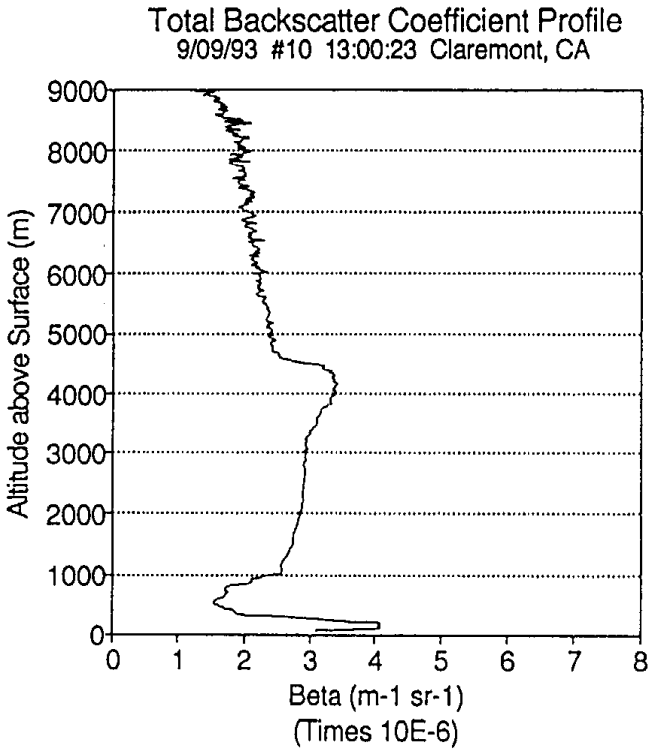

Fig. 11c

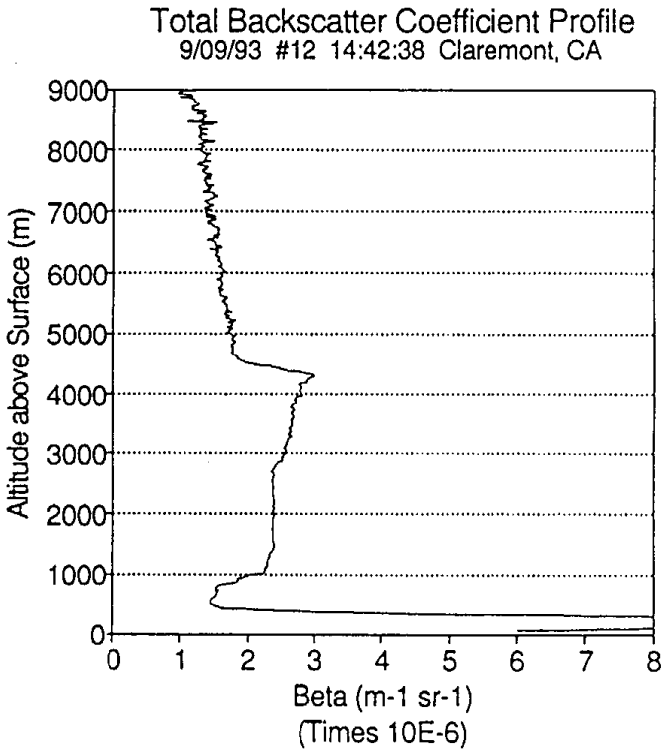

Fig. 11d

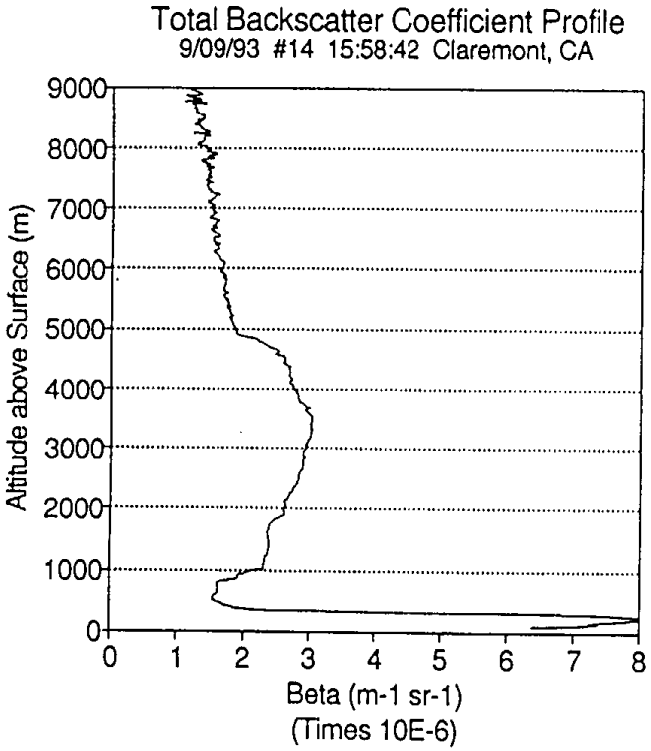

Fig. 11e

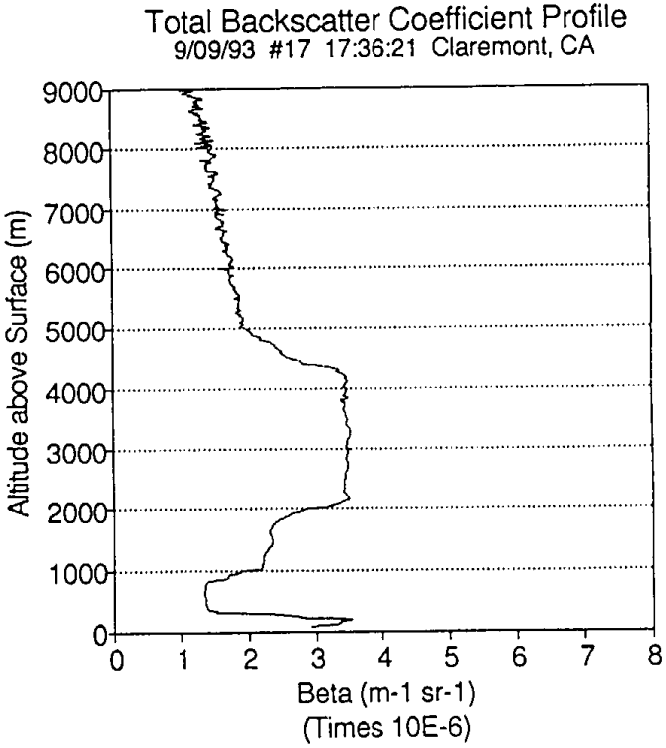

Fig. 11f

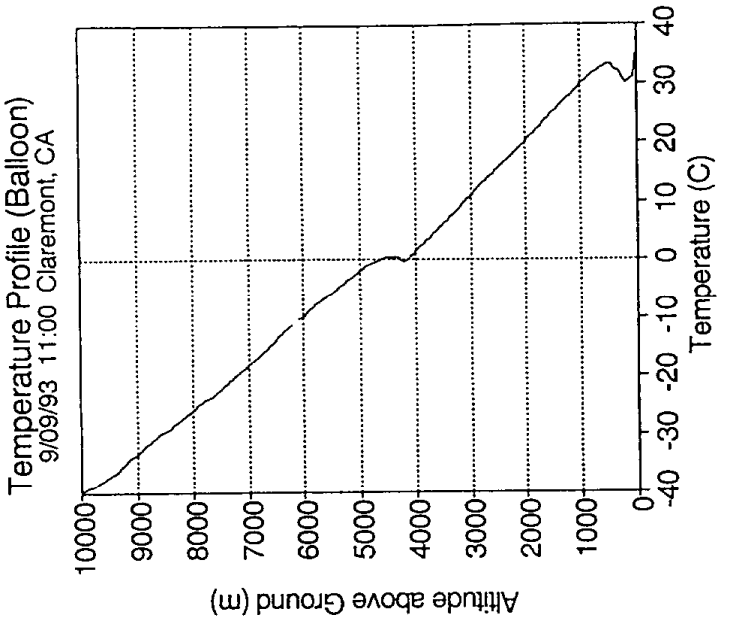

Fig. 12b

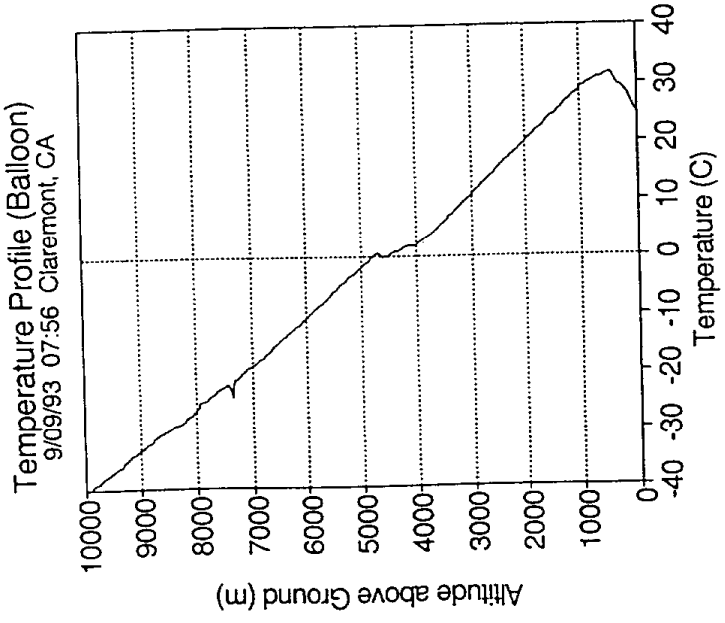

Fig. 12a

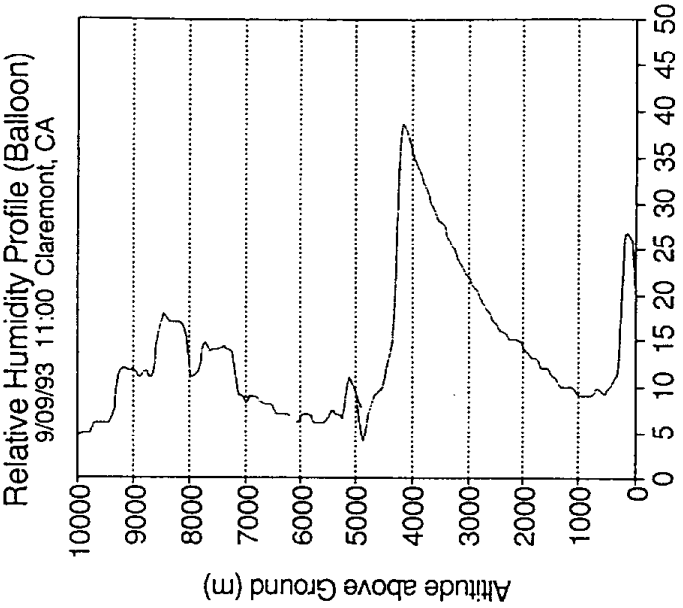

Fig. 13b

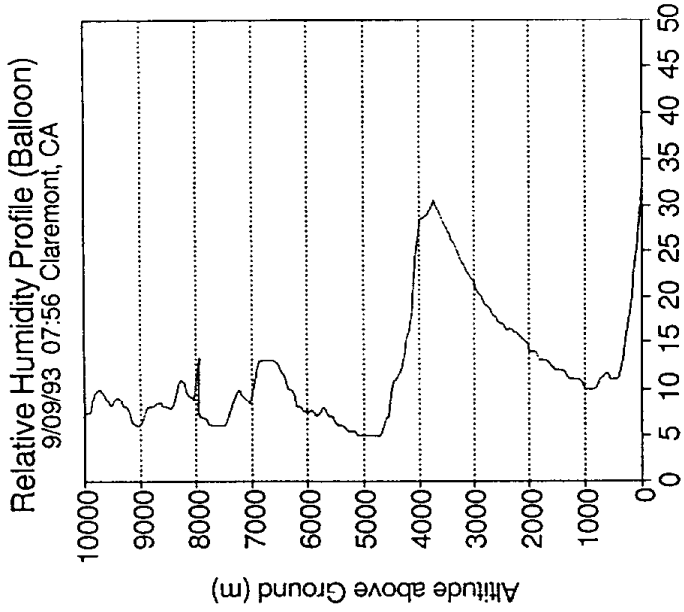

Fig. 13a

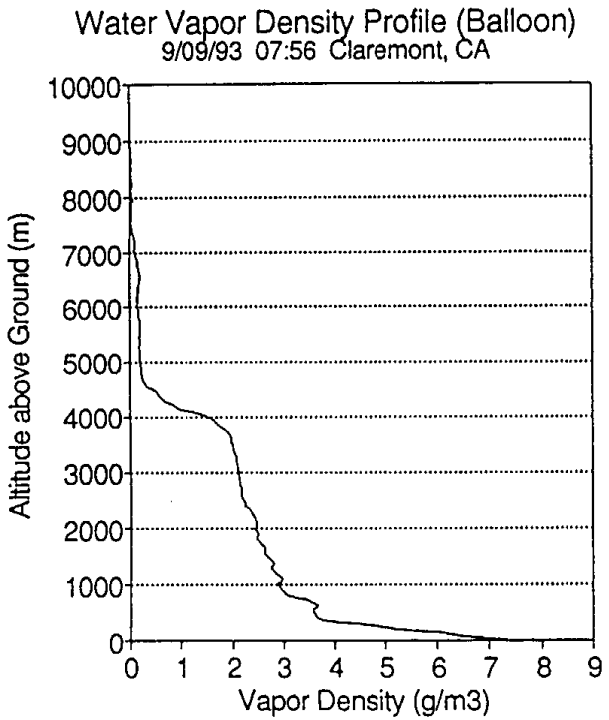

Fig. 14a

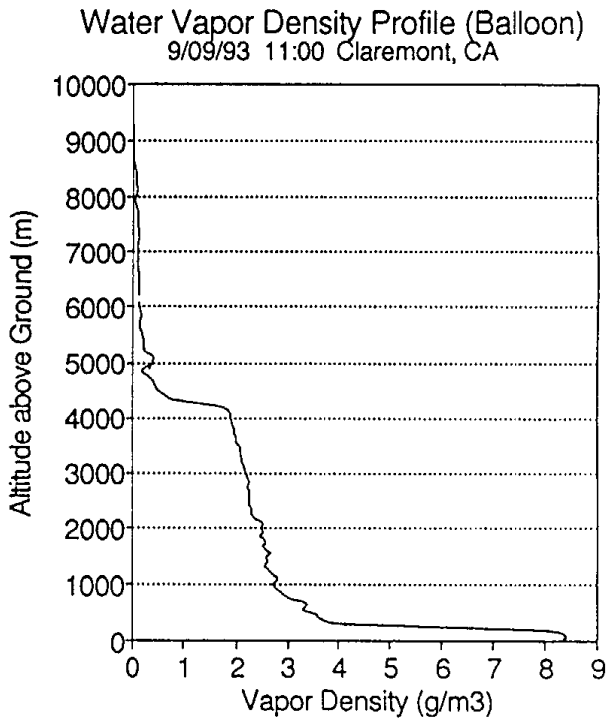

Fig. 14b

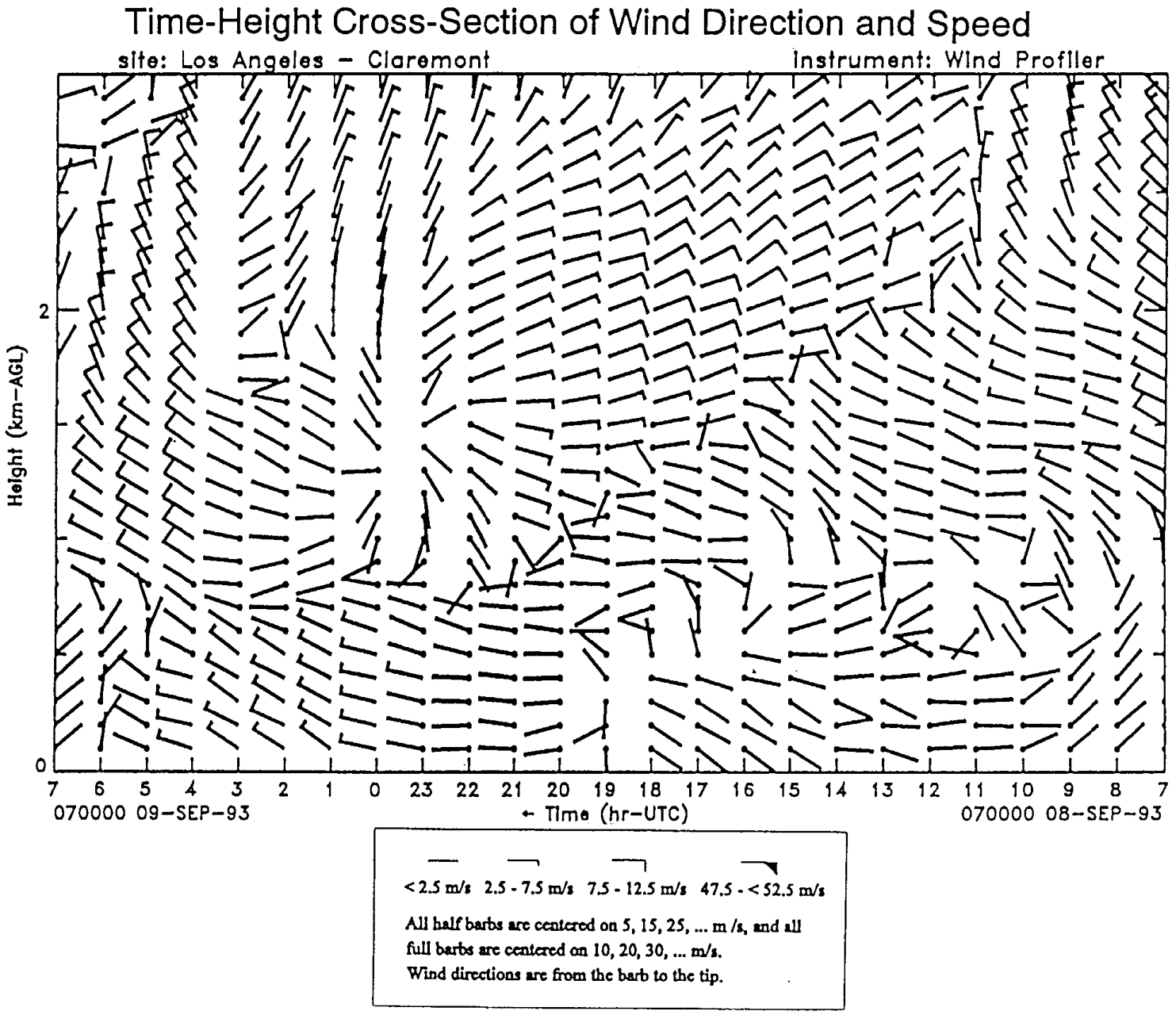
Time-Height Cross-Section of Wind Direction and Speed
site: Los Angeles – Claremont
Instrument: Wind Profiler
Height (km–AGL)
2
0
7 6 5 4 3 2 1 0 23 22 21 20 19 18 17 16 15 14 13 12 11 10 9 8 7
070000 09–SEP–93
← Time (hr–UTC)
070000 08–SEP–93
< 2.5 m/s
2.5 - 7.5 m/s
7.5 - 12.5 m/s
47.5 - < 52.5 m/s
All half barbs are centered on 5, 15, 25, ... m /s, and all full barbs are centered on 10, 20, 30, ... m/s.
Wind directions are from the barb to the tip.

Fig. 15a

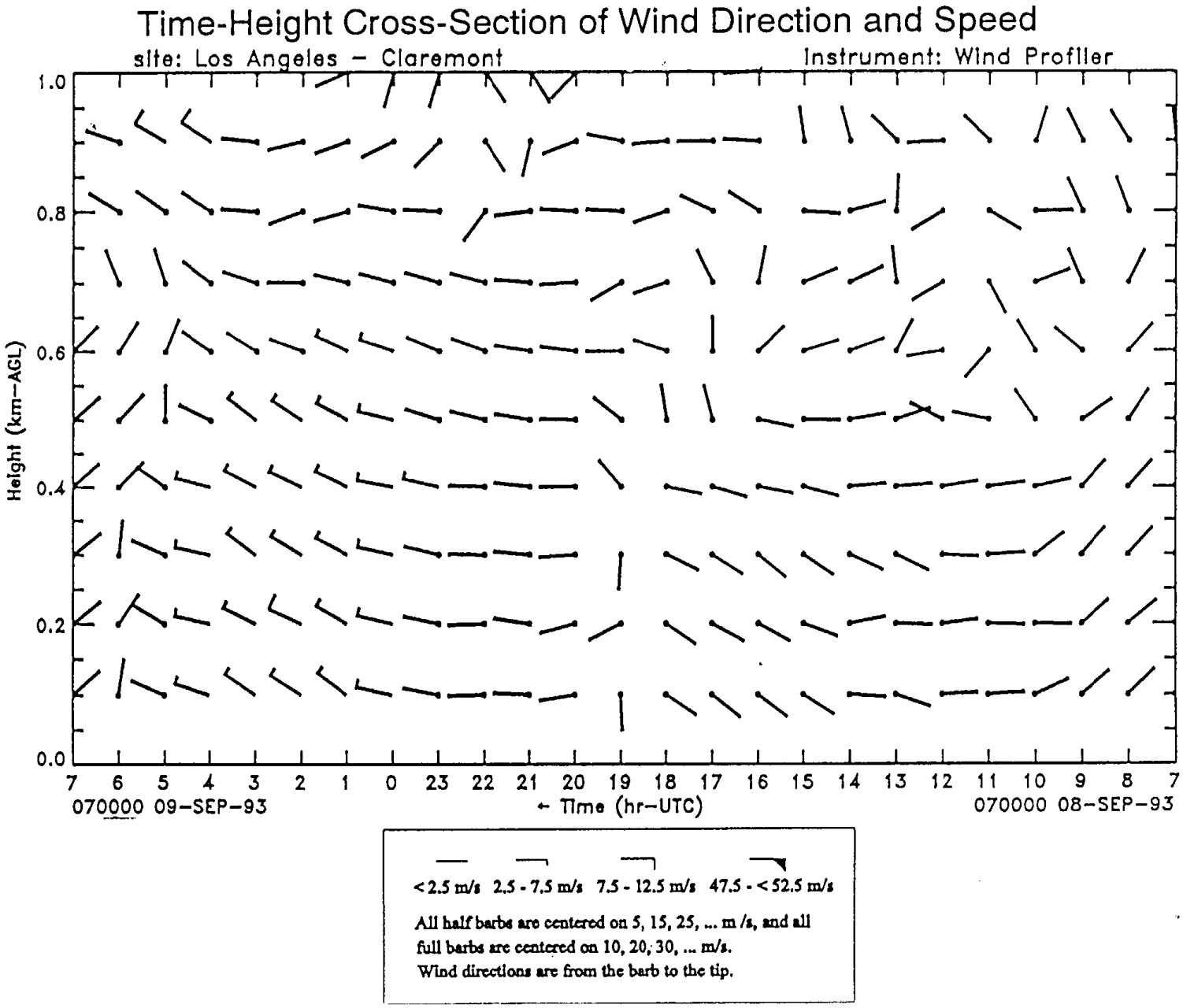
Time-Height Cross-Section of Wind Direction and Speed
site: Los Angeles - Claremont
Instrument: Wind Profiler
Height (km-AGL)
1.0
0.8
0.6
0.4
0.2
0.0
7 6 5 4 3 2 1 0 23 22 21 20 19 18 17 16 15 14 13 12 11 10 9 8 7
070000 09-SEP-93
← Time (hr-UTC)
070000 08-SEP-93
< 2.5 m/s
2.5 - 7.5 m/s
7.5 - 12.5 m/s
47.5 - < 52.5 m/s
All half barbs are centered on 5, 15, 25, ... m /s, and all full barbs are centered on 10, 20, 30, ... m/s.
Wind directions are from the barb to the tip.

Fig. 15b

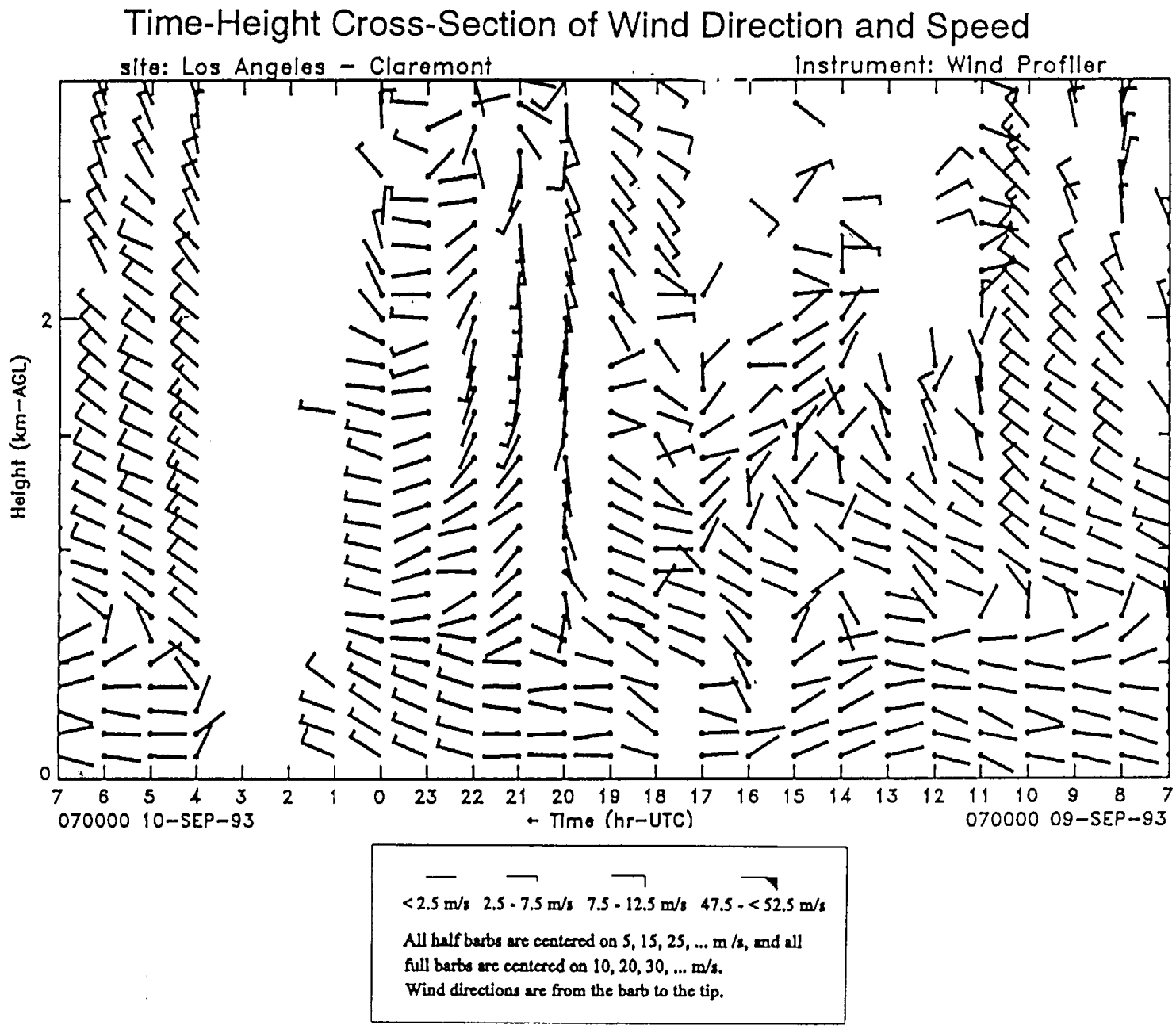
Time-Height Cross-Section of Wind Direction and Speed
site: Los Angeles - Claremont
Instrument: Wind Profiler
Height (km-AGL)
0
2
7 6 5 4 3 2 1 0 23 22 21 20 19 18 17 16 15 14 13 12 11 10 9 8 7
070000 10-SEP-93
← Time (hr-UTC)
070000 09-SEP-93
< 2.5 m/s
2.5 - 7.5 m/s
7.5 - 12.5 m/s
47.5 - < 52.5 m/s
All half barbs are centered on 5, 15, 25, ... m /s, and all full barbs are centered on 10, 20, 30, ... m/s.
Wind directions are from the barb to the tip.

Fig. 15c

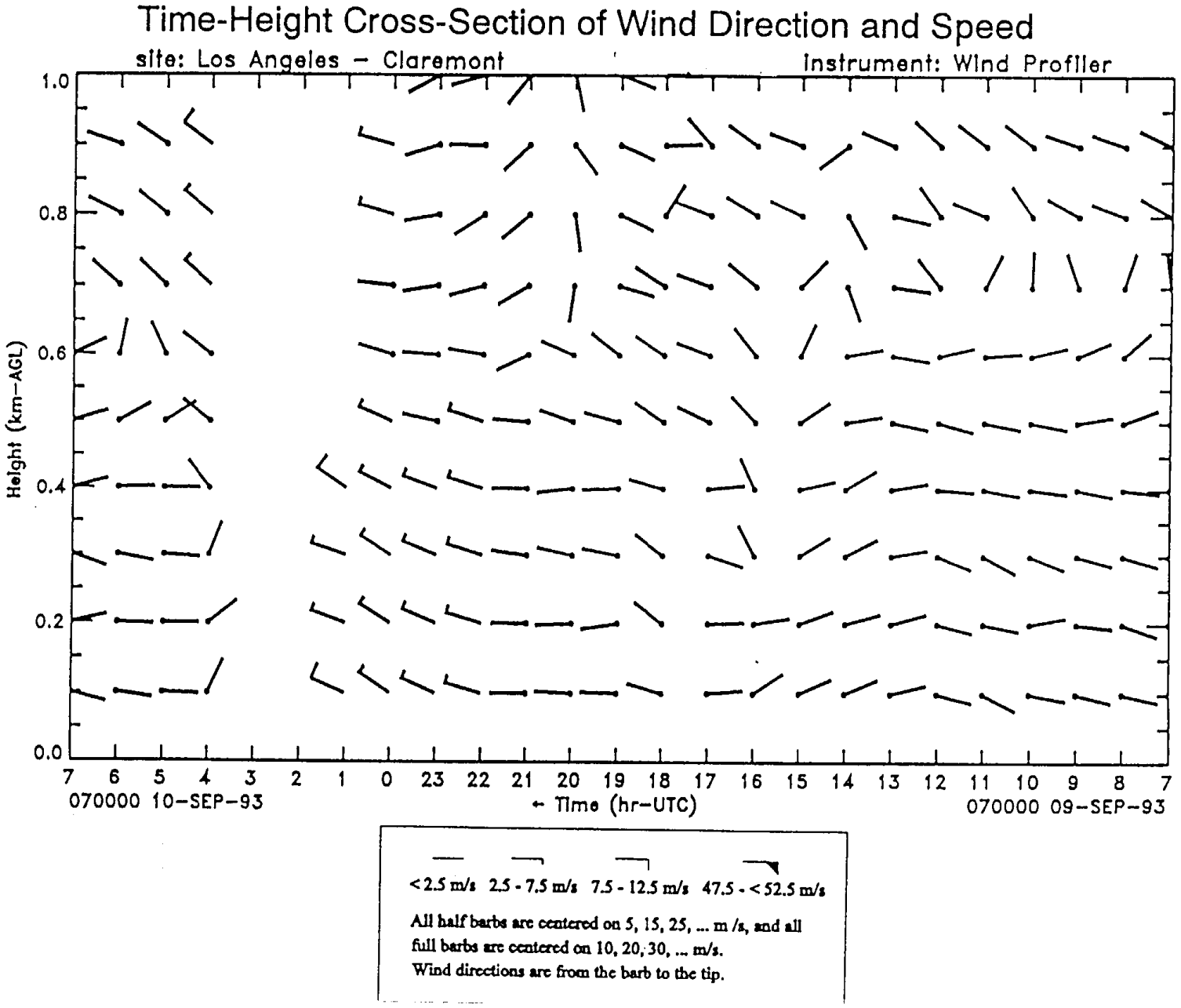
Time-Height Cross-Section of Wind Direction and Speed
site: Los Angeles – Claremont
Instrument: Wind Profiler
Height (km-AGL)
1.0
0.8
0.6
0.4
0.2
0.0
7 6 5 4 3 2 1 0 23 22 21 20 19 18 17 16 15 14 13 12 11 10 9 8 7
070000 10-SEP-93
← Time (hr-UTC)
070000 09-SEP-93
< 2.5 m/s
2.5 - 7.5 m/s
7.5 - 12.5 m/s
47.5 - < 52.5 m/s
All half barbs are centered on 5, 15, 25, ... m /s, and all full barbs are centered on 10, 20, 30, ... m/s.
Wind directions are from the barb to the tip.

Fig. 15d

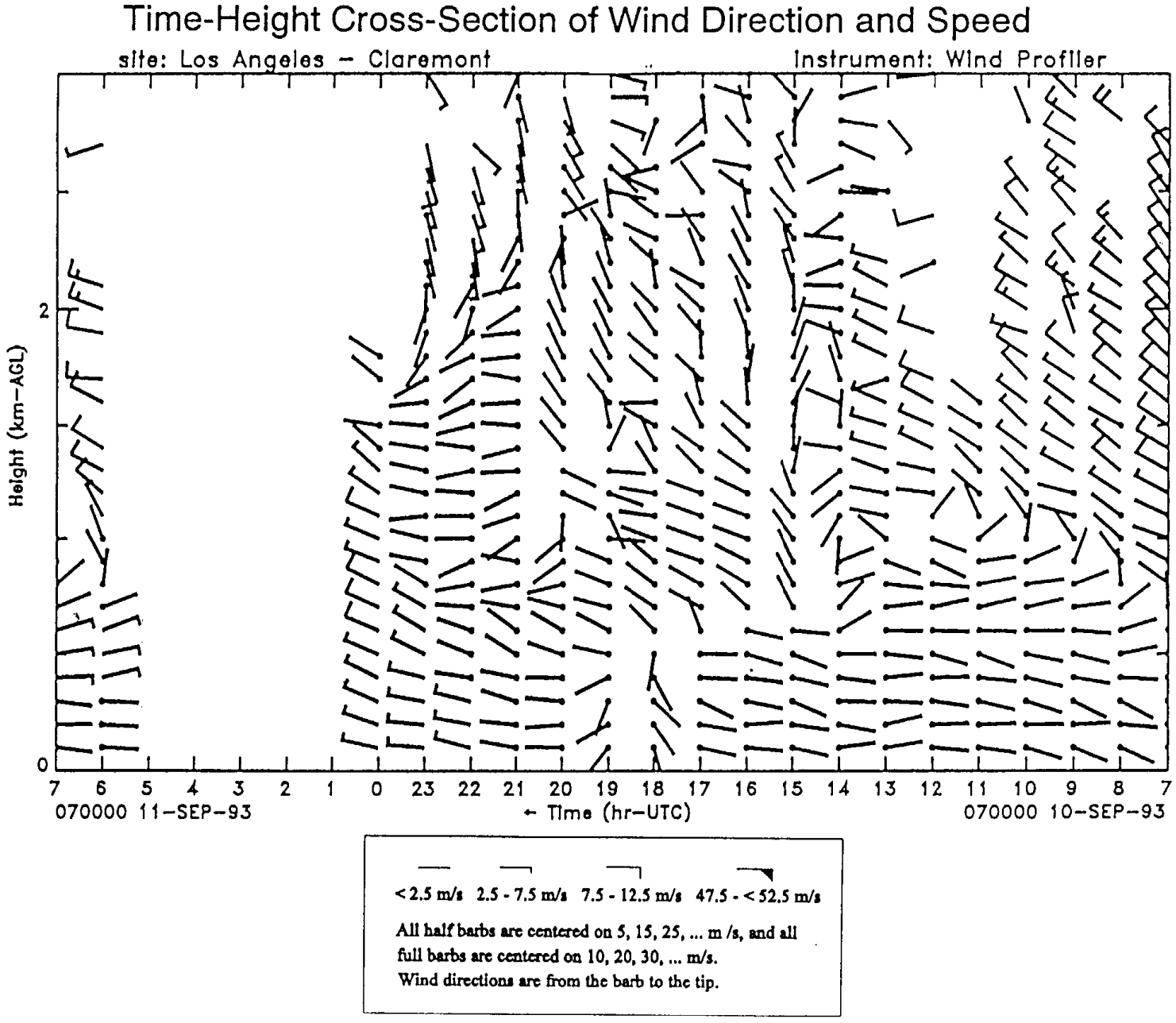
Time-Height Cross-Section of Wind Direction and Speed
site: Los Angeles - Claremont
Instrument: Wind Profiler
Height (km-AGL)
0
2
7 6 5 4 3 2 1 0 23 22 21 20 19 18 17 16 15 14 13 12 11 10 9 8 7
070000 11-SEP-93
← Time (hr-UTC)
070000 10-SEP-93
< 2.5 m/s
2.5 - 7.5 m/s
7.5 - 12.5 m/s
47.5 - < 52.5 m/s
All half barbs are centered on 5, 15, 25, ... m /s, and all full barbs are centered on 10, 20, 30, ... m/s.
Wind directions are from the barb to the tip.

Fig. 15e

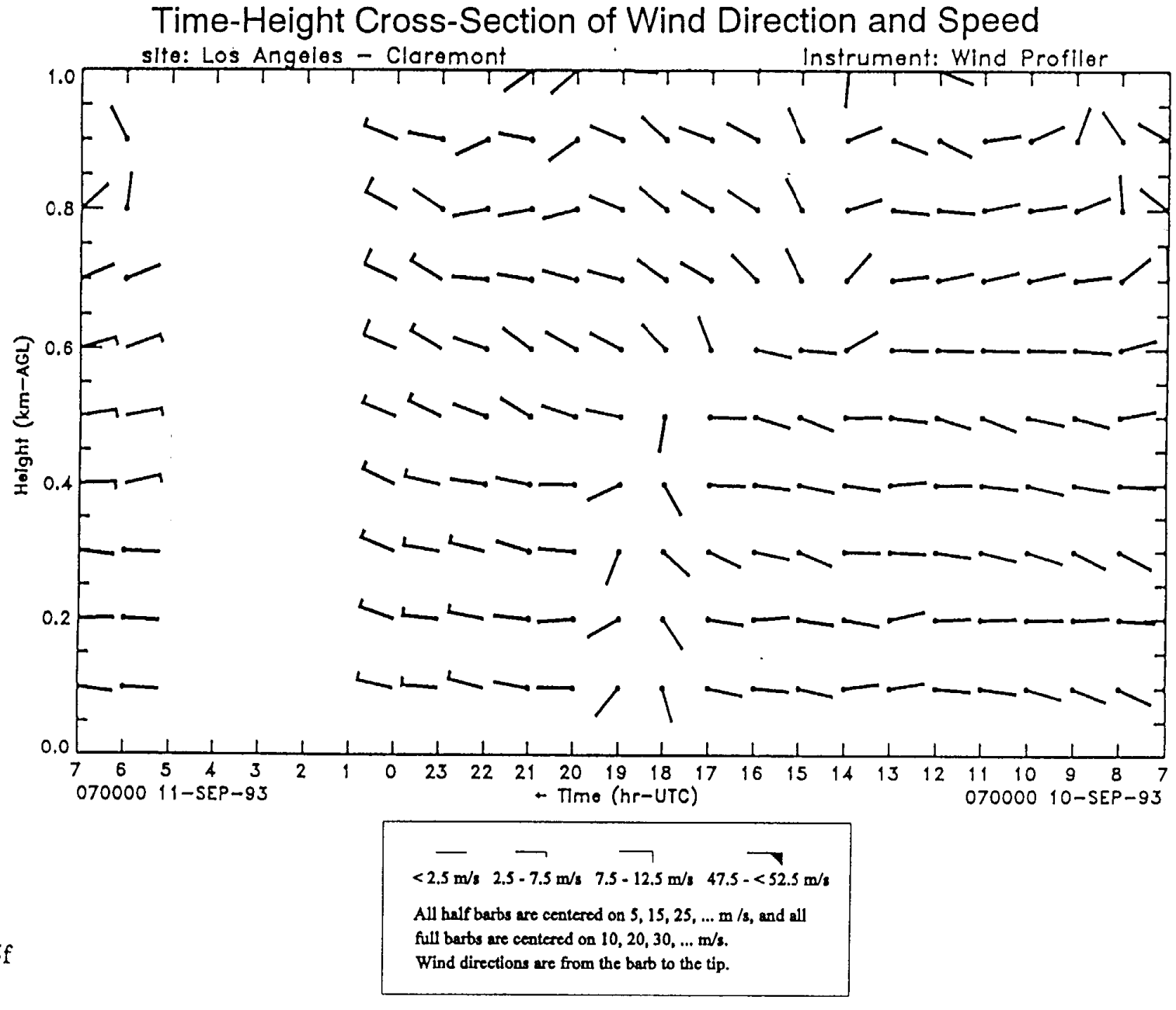
Time-Height Cross-Section of Wind Direction and Speed
site: Los Angeles – Claremont
Instrument: Wind Profiler
Height (km-AGL)
1.0
0.8
0.6
0.4
0.2
0.0
7 6 5 4 3 2 1 0 23 22 21 20 19 18 17 16 15 14 13 12 11 10 9 8 7
070000 11-SEP-93
← Time (hr-UTC)
070000 10-SEP-93
< 2.5 m/s
2.5 - 7.5 m/s
7.5 - 12.5 m/s
47.5 - < 52.5 m/s
All half barbs are centered on 5, 15, 25, ... m /s, and all full barbs are centered on 10, 20, 30, ... m/s.
Wind directions are from the barb to the tip.

Fig. 15f

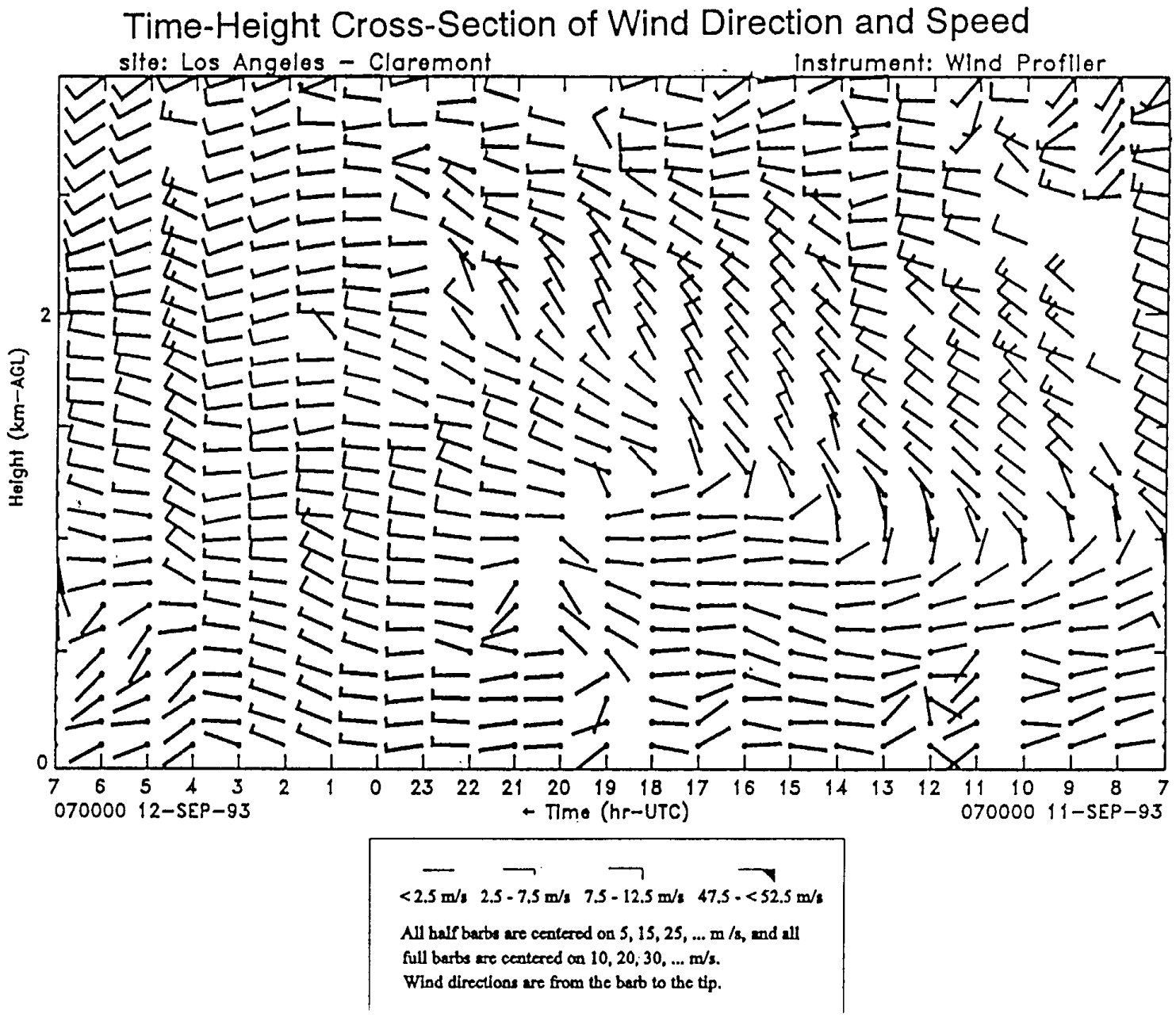
Time-Height Cross-Section of Wind Direction and Speed
site: Los Angeles – Claremont
Instrument: Wind Profiler
Height (km-AGL)
2
0
7 6 5 4 3 2 1 0 23 22 21 20 19 18 17 16 15 14 13 12 11 10 9 8 7
070000 12-SEP-93
← Time (hr-UTC)
070000 11-SEP-93
< 2.5 m/s
2.5 - 7.5 m/s
7.5 - 12.5 m/s
47.5 - < 52.5 m/s
All half barbs are centered on 5, 15, 25, ... m /s, and all full barbs are centered on 10, 20, 30, ... m/s.
Wind directions are from the barb to the tip.

Fig. 15g

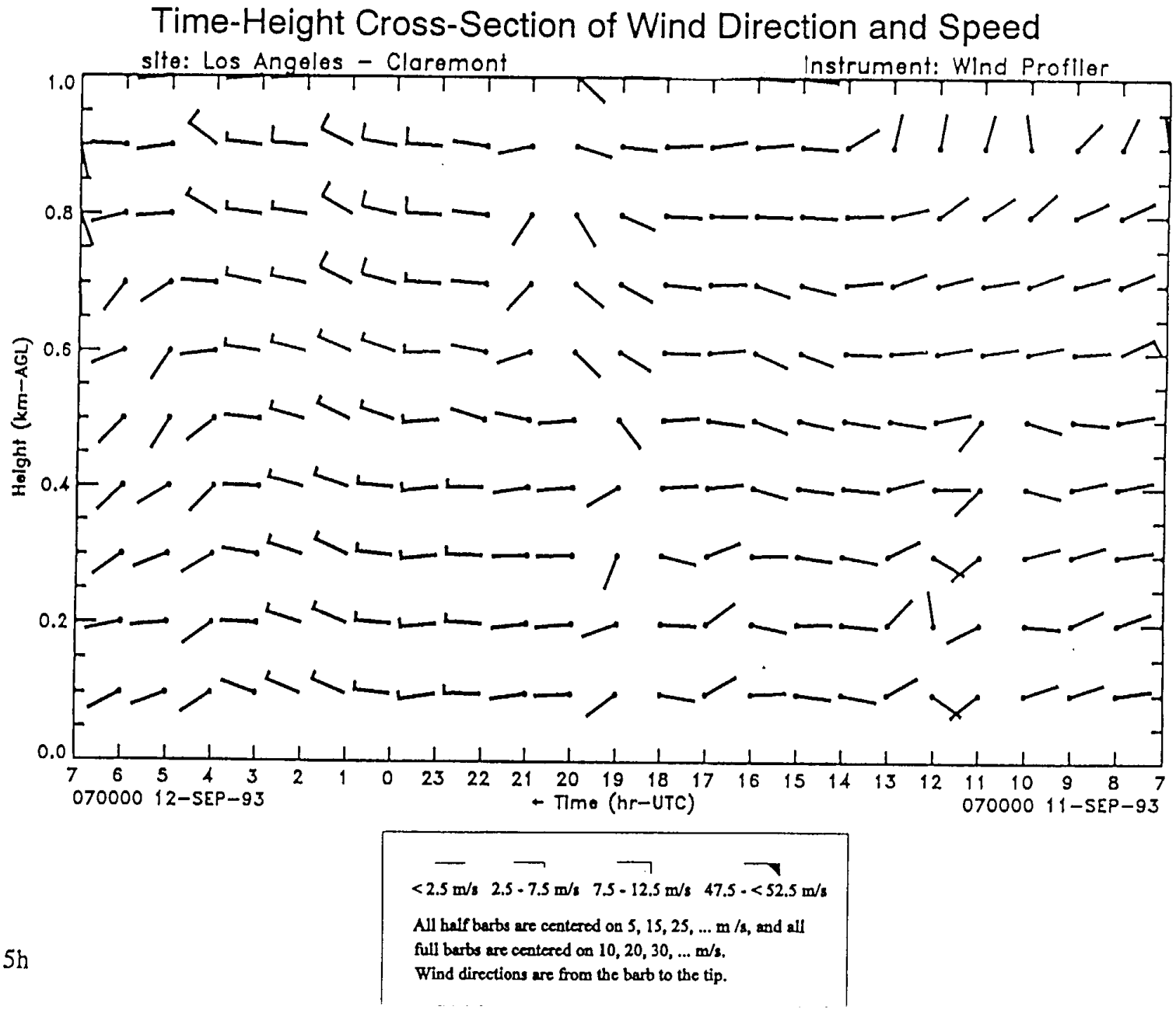
Time-Height Cross-Section of Wind Direction and Speed
site: Los Angeles - Claremont
Instrument: Wind Profiler
Height (km-AGL)
1.0
0.8
0.6
0.4
0.2
0.0
7 6 5 4 3 2 1 0 23 22 21 20 19 18 17 16 15 14 13 12 11 10 9 8 7
070000 12-SEP-93
← Time (hr-UTC)
070000 11-SEP-93
< 2.5 m/s
2.5 - 7.5 m/s
7.5 - 12.5 m/s
47.5 - < 52.5 m/s
All half barbs are centered on 5, 15, 25, ... m /s, and all full barbs are centered on 10, 20, 30, ... m/s.
Wind directions are from the barb to the tip.

Fig. 15h

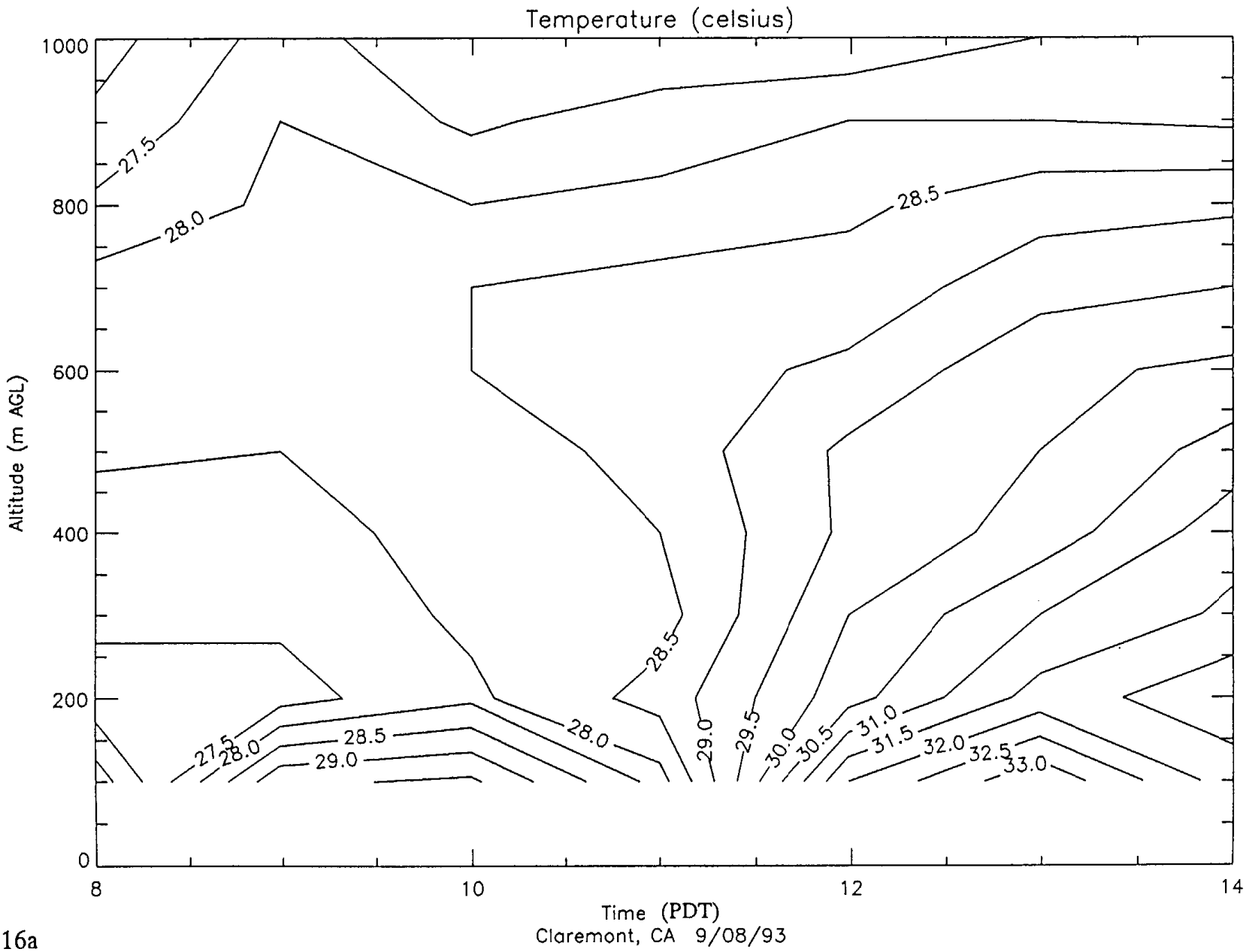
Temperature (celsius)
Altitude (m AGL)
1000
800
600
400
200
0
8
10
12
14
Time (PDT)
Claremont, CA 9/08/93
27.5
28.0
28.5
29.0
29.5
30.0
30.5
31.0
31.5
32.0
32.5
33.0

Fig. 16a

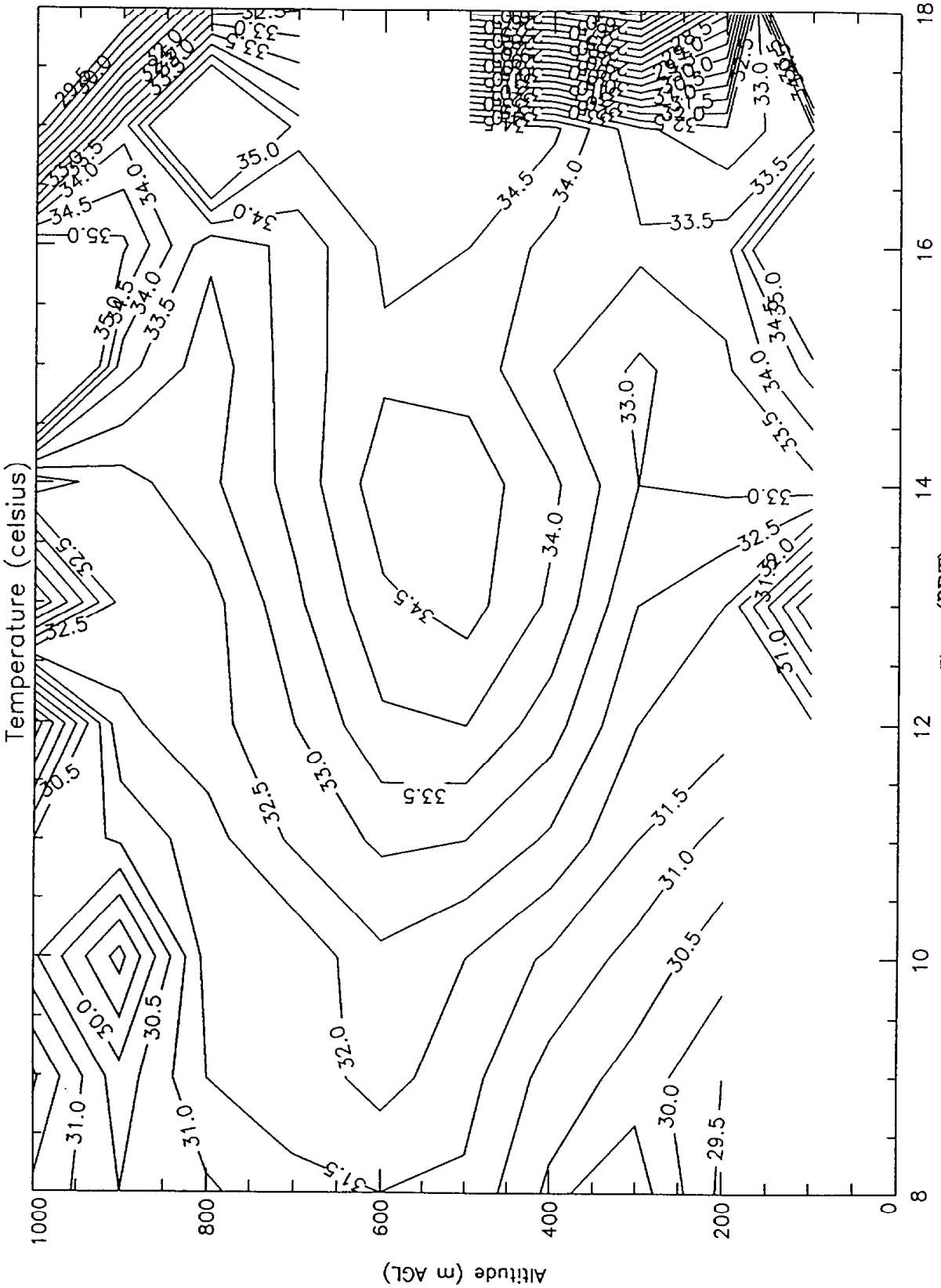
Temperature (celsius)
Altitude (m AGL)
Time (PDT)
Claremont, CA 9/09/93
1000
800
600
400
200
0
8
10
12
14
16
18
29.5
30.0
30.5
31.0
31.5
32.0
32.5
33.0
33.5
34.0
34.5
35.0

Fig. 16b

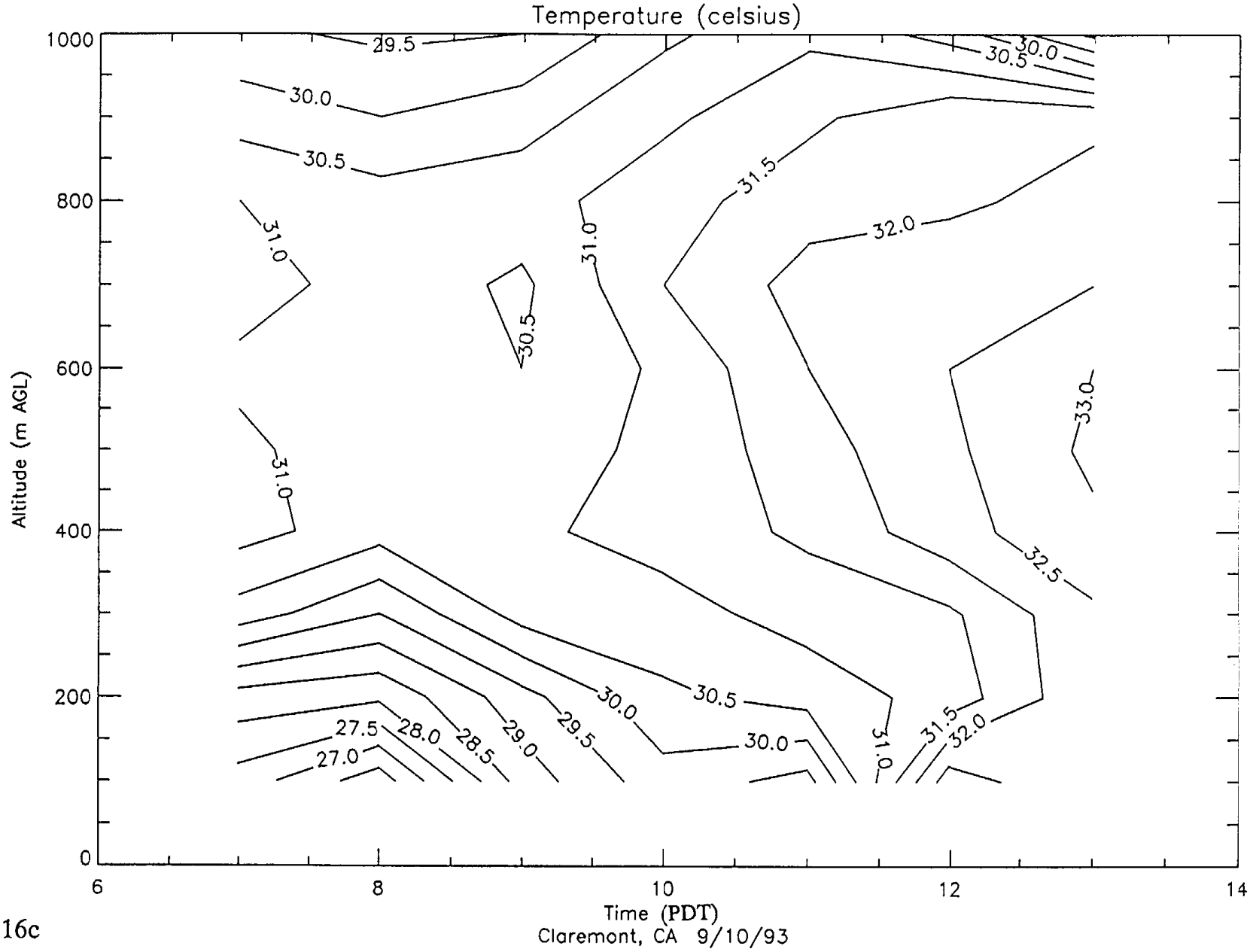
Temperature (celsius)
Altitude (m AGL)
1000
800
600
400
200
0
6
8
10
12
14
Time (PDT)
Claremont, CA 9/10/93
29.5
30.0
30.5
31.0
31.5
32.0
32.5
33.0
27.5
28.0
28.5
29.0

Fig. 16c

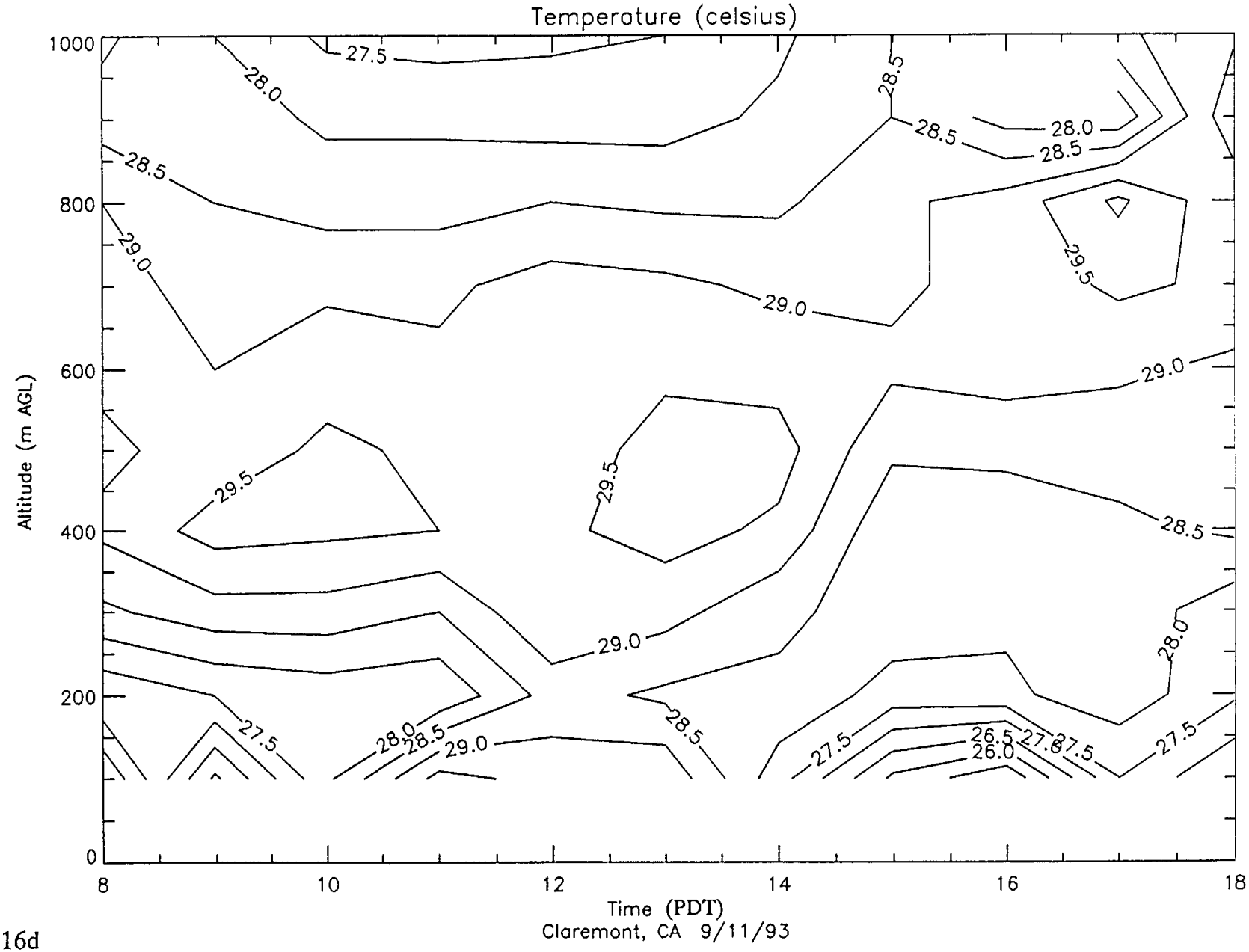
Temperature (celsius)
Altitude (m AGL)
1000
800
600
400
200
0
8
10
12
14
16
18
Time (PDT)
Claremont, CA 9/11/93
27.5
28.0
28.5
29.0
29.5
26.0
26.5
27.8

Fig. 16d

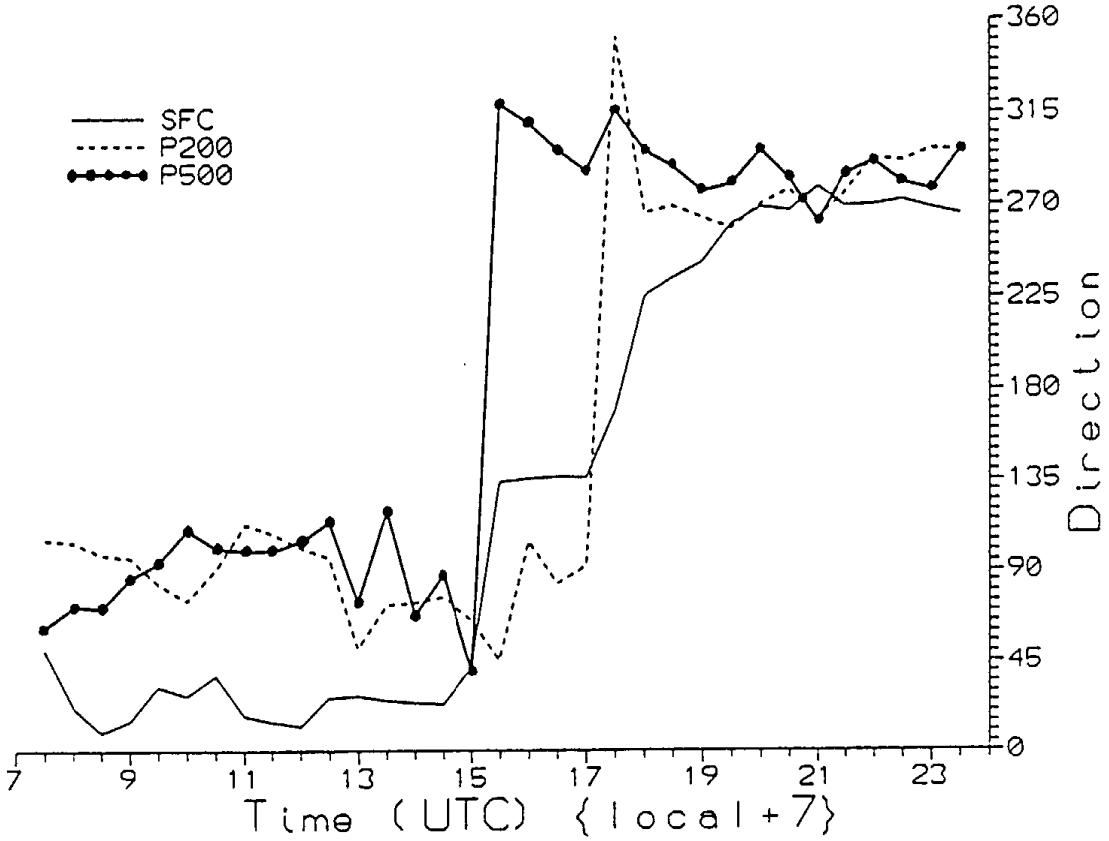

Time series of 30 min average wind directions (surface and profiler 0.2 and 0.5 km AGL) at 0700 UTC 9 September until 0000 UTC 10 September 1993. Local time equals UTC-7 hrs.

Fig. 17

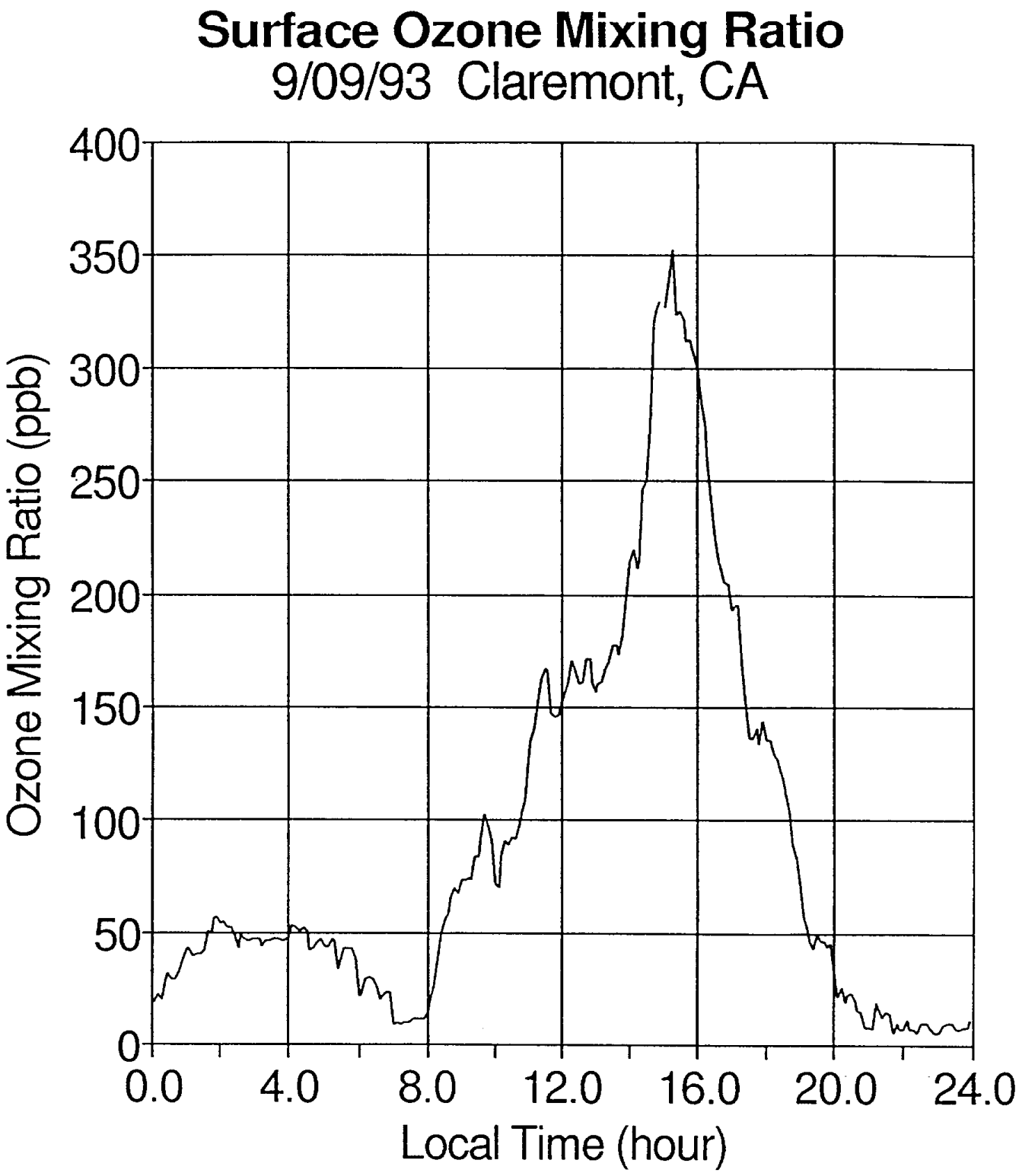
Surface Ozone Mixing Ratio
9/09/93 Claremont, CA
Ozone Mixing Ratio (ppb)
400
350
300
250
200
150
100
50
0
0.0
4.0
8.0
12.0
16.0
20.0
24.0
Local Time (hour)

Fig. 18

REFERENCES

1. Yanzeng Zhao, James N. Howell, and R. Michael Hardesty, "Transportable Lidar for the Measurement of Ozone Concentration and Aerosol Profiles in the Lower Troposphere," A&WMA/SPIE *International Symposium on Optical Sensing for Environmental Monitoring*, October 11-14, 1993, Atlanta, Georgia, pp. 310-320, **SPIE Proceedings** Vol. 2112.

2. Yanzeng Zhao, R. Michael Hardesty, Daniel E. Wolf, and John E. Gaynor, "Joint Observations of the ETL Ozone Lidar and MPS System during the Los Angeles Free-Radical Study," A&WMA/EPA *International Symposium and Courses: Measurement of Toxic and Related Air Pollutants*, May 3-6, 1994, Durham, North Carolina.

3. Yanzeng Zhao, James N. Howell, and R. Michael Hardesty, "ETL's Transportable Lower Troposphere Ozone Lidar," *17th International Laser Radar Conference*, July 25-29, 1994, Sendai, Japan.

4. John J. Carroll and Yanzeng Zhao, "Comparison of *in situ* and DIAL Measured Vertical Tropospheric Ozone Profiles," *Third International Symposium on Tropospheric Profiling: Needs and Technologies*, August 30 - September 2, 1994, Hamburg, Germany.

5. Weber, B.L., and D.B. Wuertz, "Quality control algorithm for profiler measurements of winds and temperatures," NOAA Technical Memorandum ERL WPL-212, NOAA Environmental Research Laboratories, Boulder CO 32 pp, 1991.

6. Moran, K.P., and B.L. Weber, "The Mobile Profiler System: A transportable integrated sounding system for measuring atmospheric parameters," Preprint: Twenty-sixth International Conference on Radar Meteorology, Norman, OK, 24-28 May 1993, Amer.

Meteor. Soc., 637-639.

7. Wolfe, D., B. Weber, D. Wuertz, D. Welsh, D. Merritt, S. King, R. Fritz, K. Moran, M. Simon, S. Anthony, J. Cogan, D. Littell, and E. Measure, "An Overview of the Mobile Profiler System: Preliminary Results from Field Tests during the Los Angeles Free-Radical Study" (in review).

8. Yanzeng Zhao, R. Michael Hardesty, and M. J. Post, "A Multibeam Transmitter for Signal Dynamic Range Reduction in Incoherent Lidar Systems," *Appl. Opt.* **31** 7623-7632 (1992).

9. Yanzeng Zhao, James N. Howell, and R. Michael Hardesty,"Transportable Lidar for the Measurement of Ozone Concentration and Flux Profiles in the Lower Troposphere," *16th International Laser Radar Conference*, 20-24 July 1992, Cambridge, Massachusetts.

10. Yanzeng Zhao, "Numerical Differentiation Methods for Estimating Ozone Concentration in DIAL Measurements," *1990 Technical Digest Series*, Volume 4, pp. 388-391, Optical Remote Sensing of the Atmosphere, February 12-15, 1990, Incline Village, Nevada.

11. Vladimir A. Kovalev, "Lidar measurement of the Vertical Aerosol Extinction Profiles with Range-Dependent Backscatter-to-Extinction Ratios," *Appl. Opt.* **36**, 6053-6065, 1993.

12. *Tropospheric Ozone Lidar Intercomparison Experiment, TROLIX'91, Field Phase Report*, Max-Planck-Institut fur Meteorologie, Report No. 102, by Jans Bösenberg et al, Hamburg, April 1993.

13. Keith, R.W., "A climatological/air quality profile; California south coast air basin. Air Programs Division Report, El Monte, CA, 165 pp, 1980.

14. Roberts, P.T. and H.H. Main, 1993: Ozone and particulate matter case study analyses for the southern California air quality study. Final Report prepared for South Coast Air Quality District by Sonoma Technology Inc.

LIST OF PUBLICATIONS

1. Yanzeng Zhao, James N. Howell, and R. Michael Hardesty, "Transportable Lidar for the Measurement of Ozone Concentration and Aerosol Profiles in the Lower Troposphere," A&WMA/SPIE *International Symposium on Optical Sensing for Environmental Monitoring*, October 11-14, 1993, Atlanta, Georgia, pp. 310-320, **SPIE Proceedings** Vol. 2112.

2. Yanzeng Zhao, R. Michael Hardesty, Daniel E. Wolfe, and John E. Gaynor, "Joint Observations of the ETL Ozone Lidar and MPS System during the Los Angeles Free-Radical Study," A&WMA/EPA *International Symposium and Courses: Measurement of Toxic and Related Air Pollutants*, May 3-6, 1994, Durham, North Carolina.

3. Yanzeng Zhao, James N. Howell, and R. Michael Hardesty, "ETL's Transportable Lower Troposphere Ozone Lidar," *17th International Laser Radar Conference*, July 25-29, 1994, Sendai, Japan.

4. John J. Carroll and Yanzeng Zhao, "Comparison of *in situ* and DIAL Measured Vertical Tropospheric Ozone Profiles," *Third International Symposium on Tropospheric Profiling: Needs and Technologies*, August 30 - September 2, 1994, Hamburg, Germany.

GLOSSARY OF TERMS, ABBREVIATIONS, AND SYMBOLS

AGL	**A**bove **G**round **L**evel
DIAL	**Di**fferential **A**bsorption **L**idar
ETL	**E**nvironmental **T**echnology **L**aboratory (former Wave Propagation Laboratory)
LAFRS	**L**os Angeles **A**tmospheric **F**ree **R**adical **S**tudy
LIDAR	**Li**ght **D**etection **a**nd **R**anging (Lidar is a system that transmits laser beam(s) and collects backscattered radiation through telescope(s). The received radiation is then transferred to electronic signals by optical detectors. Since the backscattered radiation from different distance has different time delay, the signal is range-resolved.)
MPS	**M**obile **P**rofiler **S**ystem
NOAA	**N**ational **O**ceanic and **A**tmospheric **A**dministration
SNR	**S**ignal-to-**N**oise **R**atio
UTC	**U**niversal **T**ime **C**oordinate
PDT	**P**acific **D**aylight **T**ime

APPENDIX A OZONE ABSORPTION BANDS

The following figures are taken from the book *Aeronomy of the Middle Atmosphere: Chemistry and Physics in the Stratosphere and Mesosphere*, by Guy Brasseur and Susan Solomon, 1984. The straight lines in the upper figure were added by the author to show the online and offline wavelengths of the ETL ozone lidar.

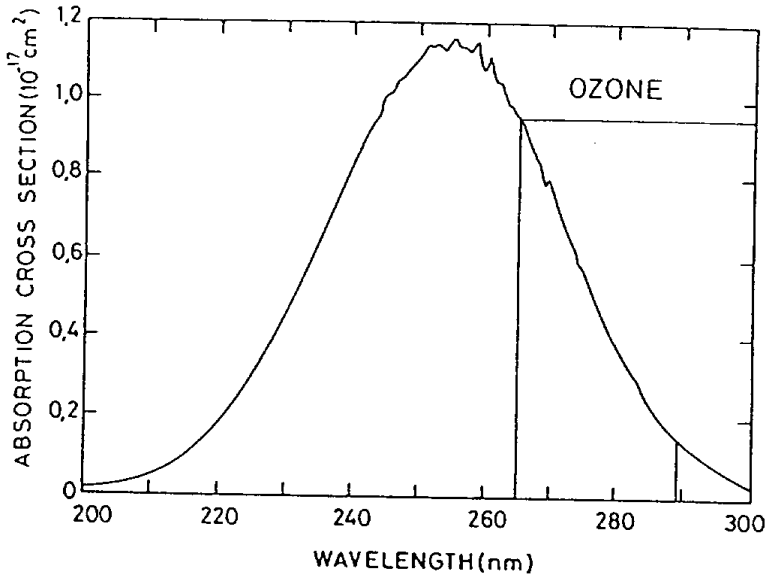

Fig. 4.32. Hartley band of ozone. Absorption cross section from 200 to 300 nm After Griggs (1968).

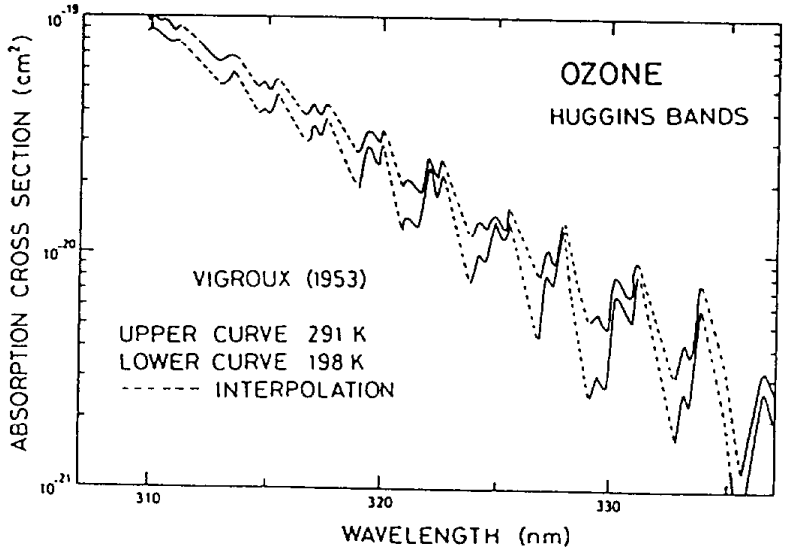

Fig. 4.33. Huggins bands of ozone. Absorption cross sections from 310 to 370 nm, showing the effects of temperature. From Nicolet (1980).

APPENDIX B ETL OZONE LIDAR IN A LABORATORY

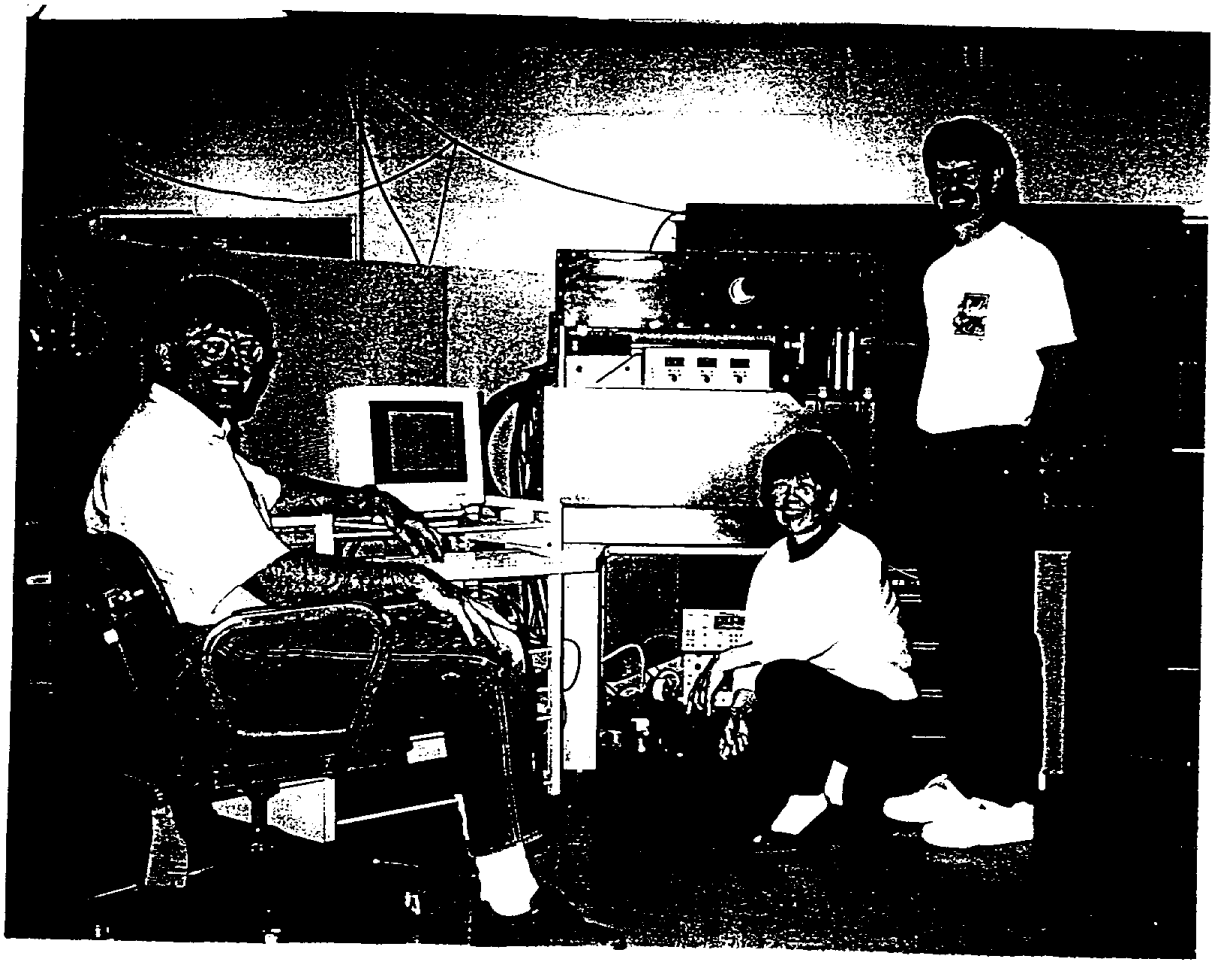

APPENDIX C ETL OZONE LIDAR IN THE 20-FOOT MODIFIED SEA-CONTAINER

APPENDIX D ORTHOGRAPHIC VIEW OF LOS ANGELES BASIN

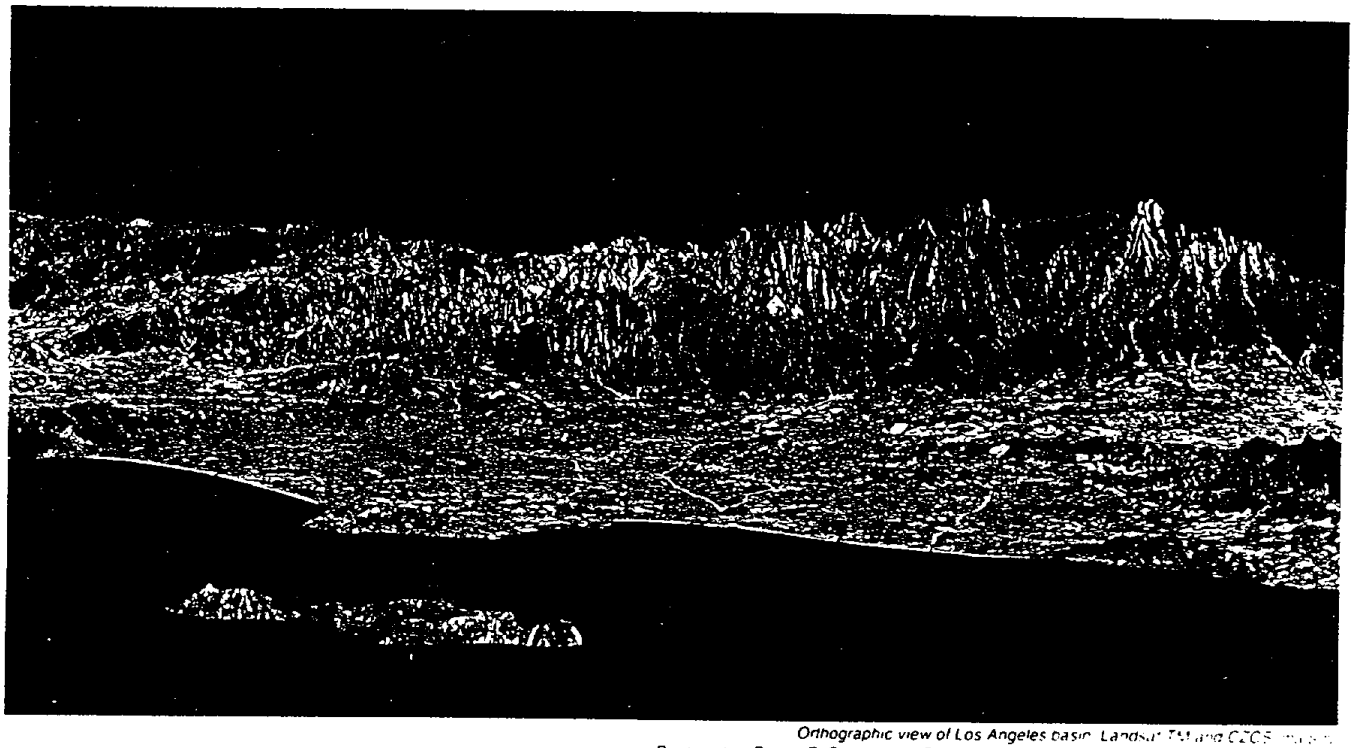

Orthographic view of Los Angeles basin. Landsat TM and CDCS [illegible]
Produced by Robert E. Crippen, Jet Propulsion Laboratory, Cal[illegible]

APPENDIX E INTERCOMPARISON BETWEEN VARIOUS OZONE LIDARS AND A HELICOPTER-BORNE UV-PHOTOMETER AND AN OZONE SONDE (FROM REFERENCE 12)

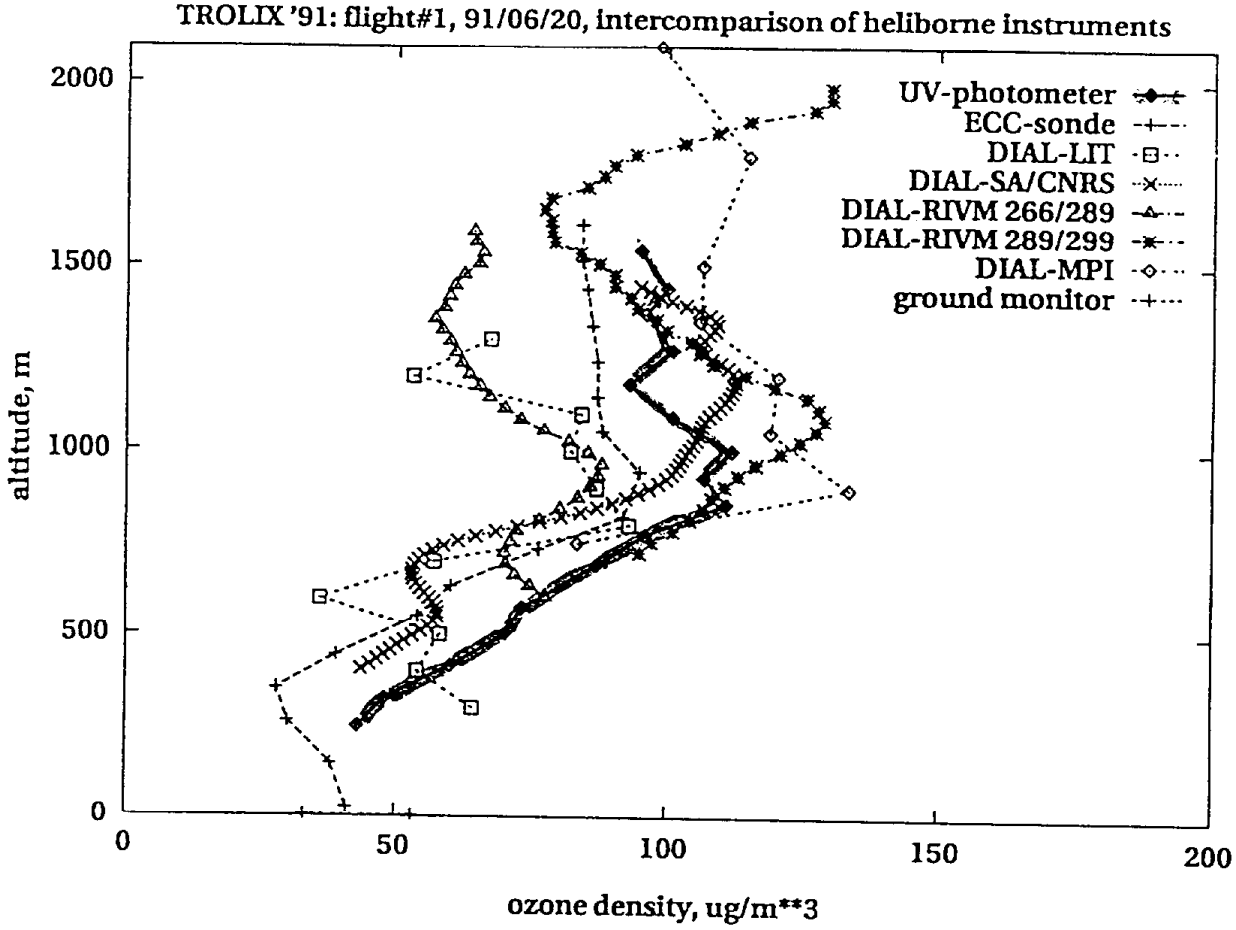

Figure 6.5: Intercomparison of Lidars and in situ instruments for helicopter flight 1 on June 20.

APPENDIX F EXAMPLES OF AIRPLANE FLIGHT PATHS

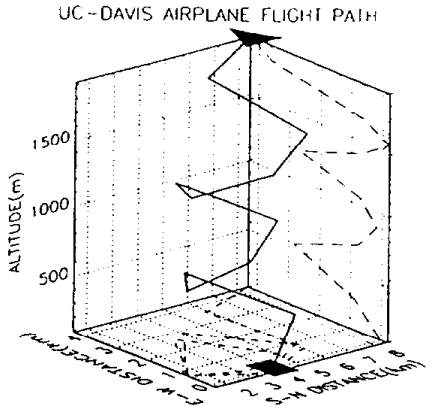

7/15/93 TIME: 7:57:4 - 8:9:13

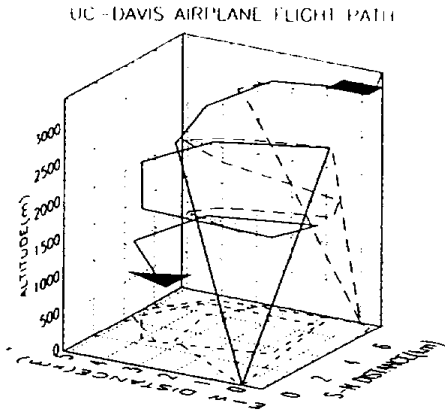

7/19/93 TIME: 15:19:28 - 15:34:56

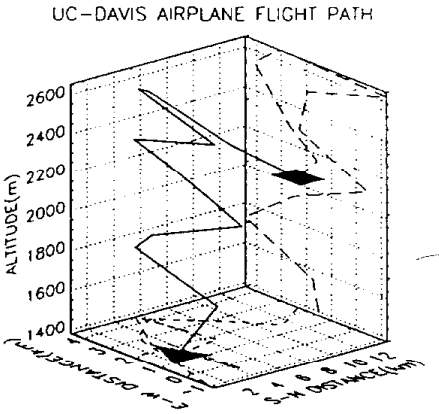

7/15/94 TIME: 8:12:33 - 8:28:8

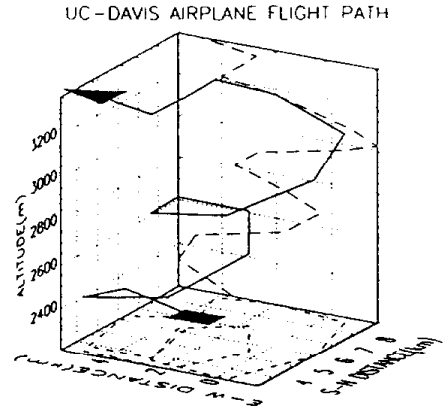

7/19/93 TIME: 14:59:54 - 15:16:29

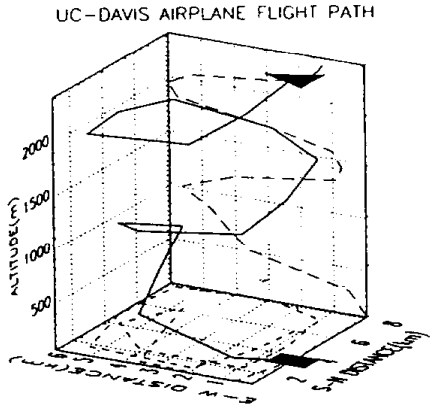

7/22/93 TIME: 10:30:3 - 10:47:45

APPENDIX G TIME-HEIGHT CHARTS OF OZONE CONCENTRATIONS ON SEPTEMBER 5, 7, 8-11, 14, 18-19, 1993

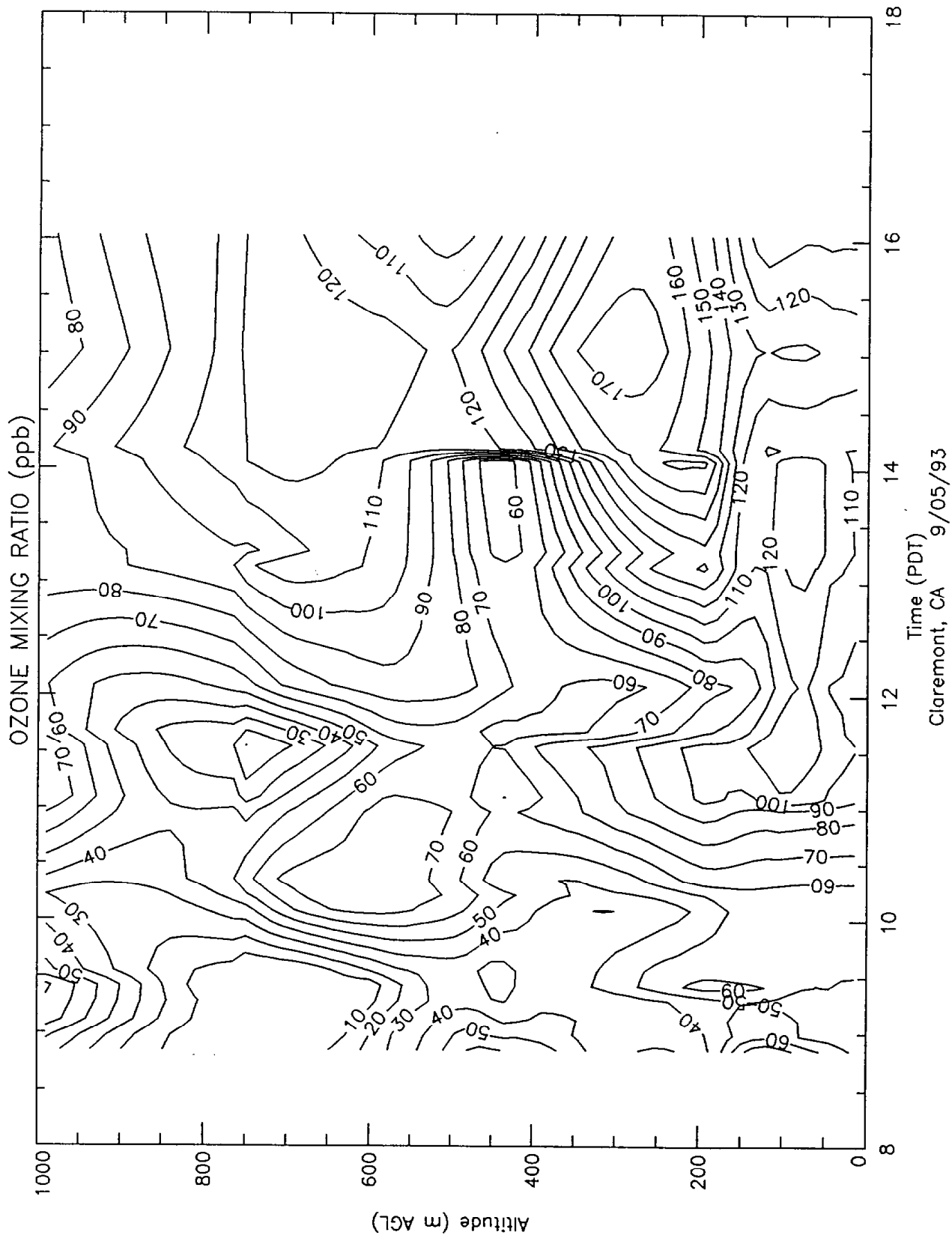
OZONE MIXING RATIO (ppb)
Altitude (m AGL)
Time (PDT)
Claremont, CA 9/05/93

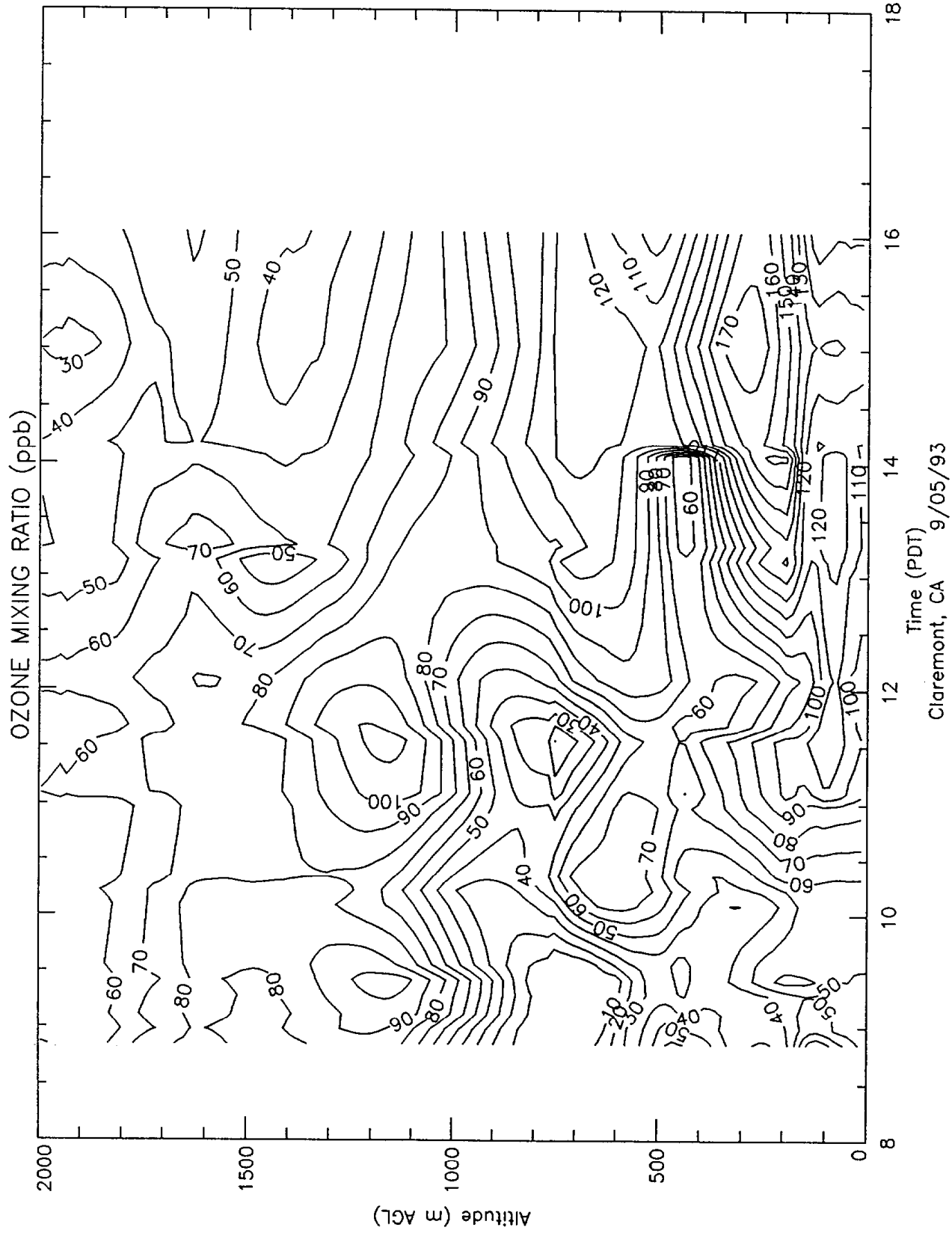
OZONE MIXING RATIO (ppb)
Altitude (m AGL)
Time (PDT)
Claremont, CA 9/05/93

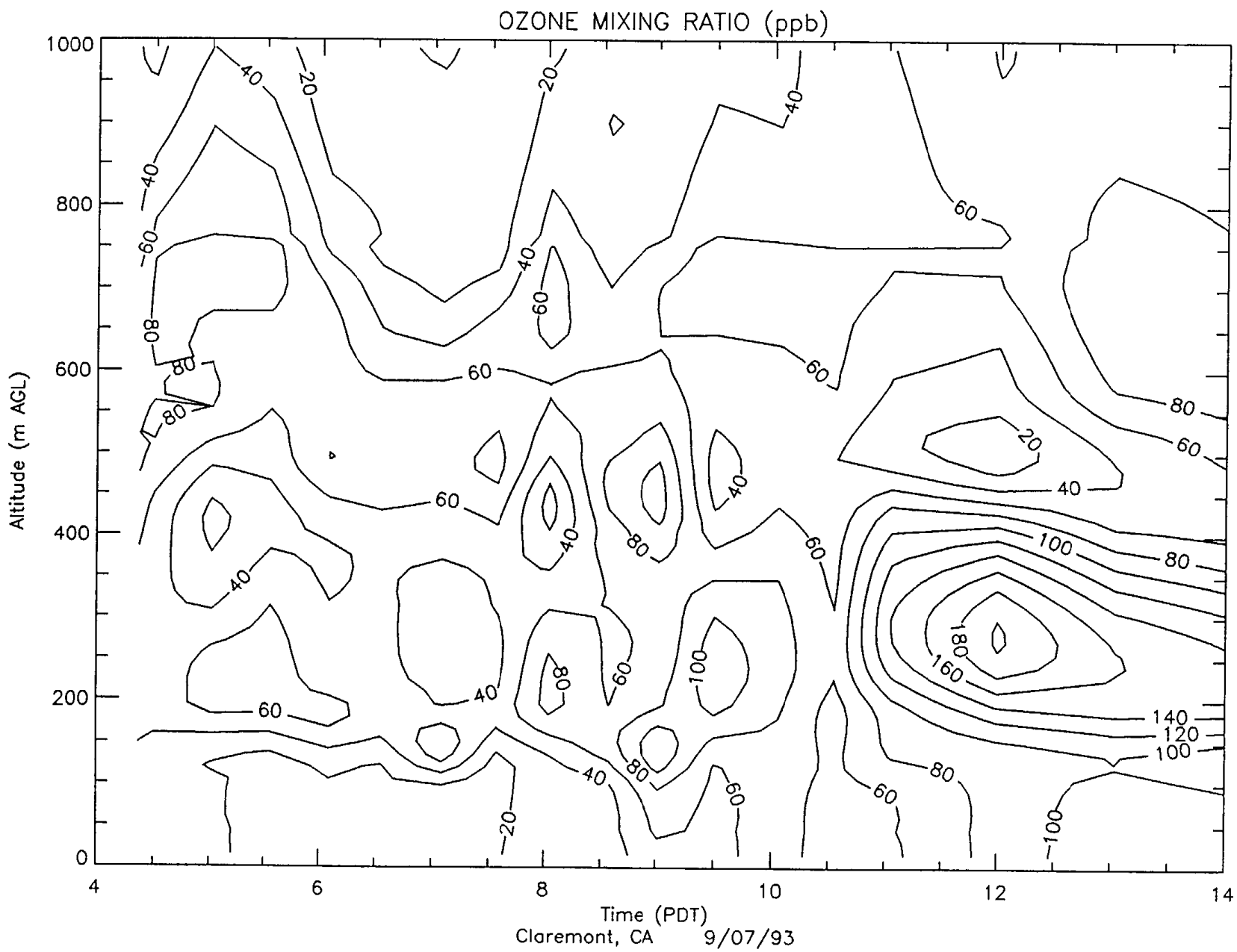
OZONE MIXING RATIO (ppb)
Altitude (m AGL)
1000
800
600
400
200
0
4
6
8
10
12
14
Time (PDT)
Claremont, CA 9/07/93

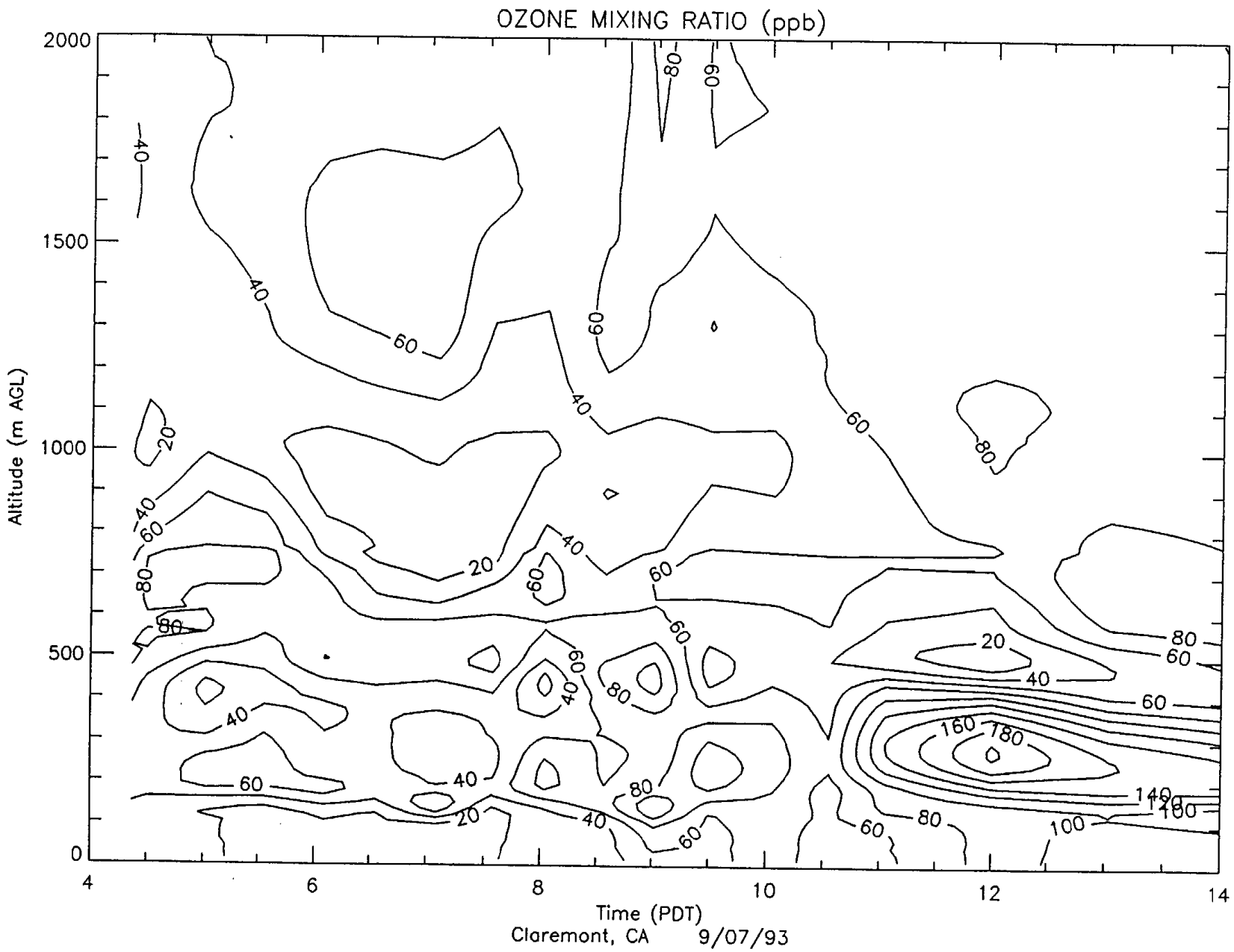
OZONE MIXING RATIO (ppb)
Altitude (m AGL)
2000
1500
1000
500
0
4
6
8
10
12
14
Time (PDT)
Claremont, CA 9/07/93

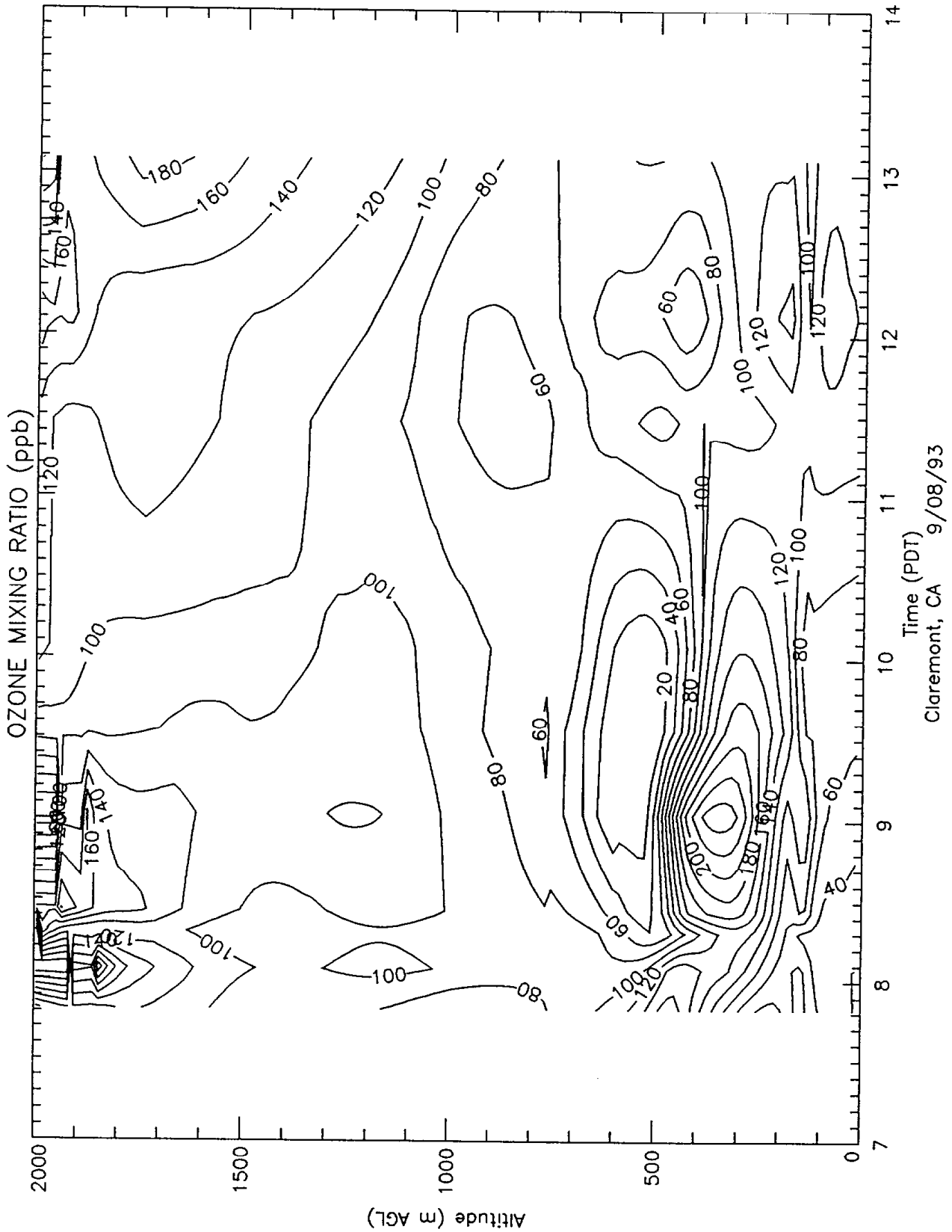
OZONE MIXING RATIO (ppb)
Altitude (m AGL)
Time (PDT)
Claremont, CA 9/08/93

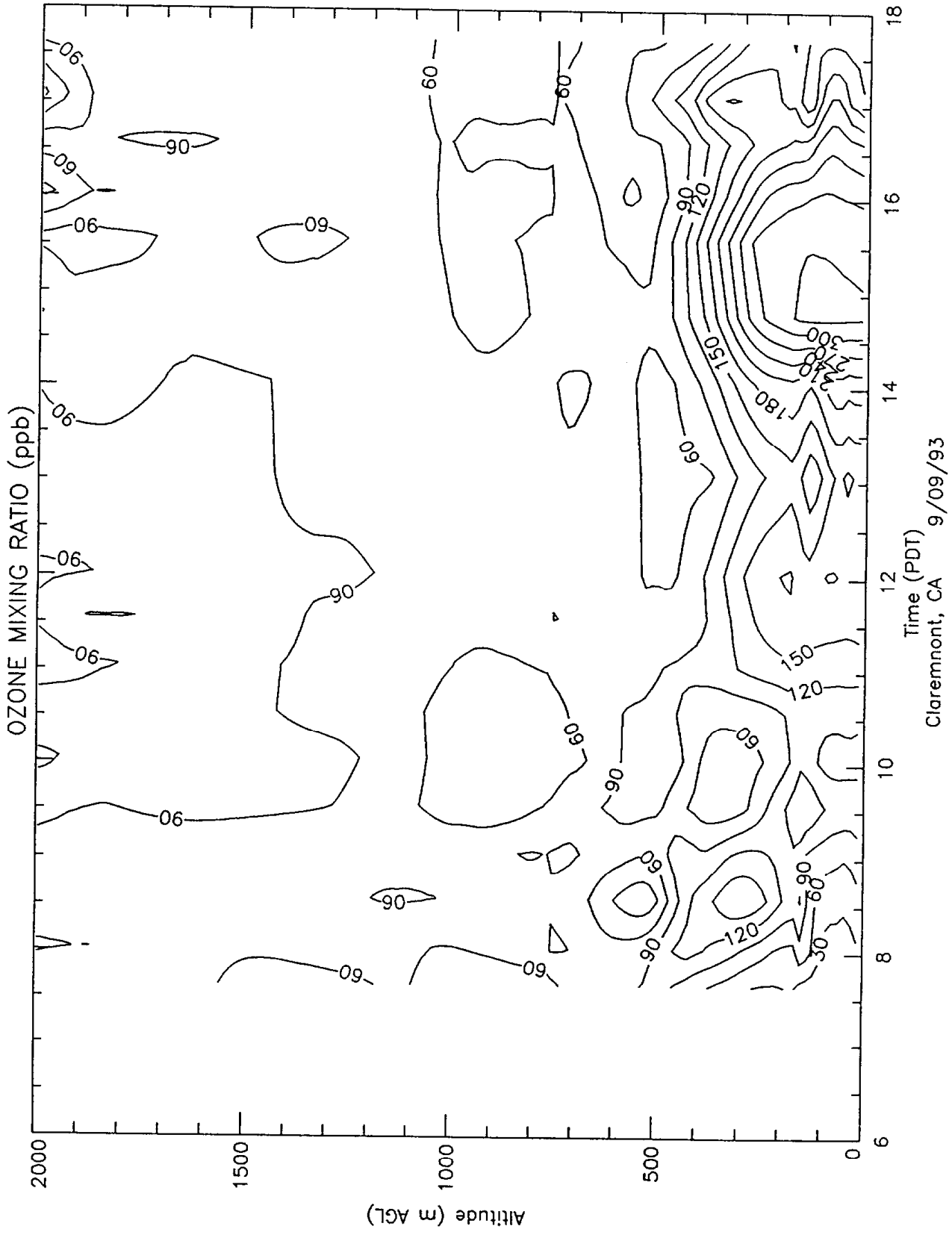
OZONE MIXING RATIO (ppb)
Altitude (m AGL)
2000
1500
1000
500
0
6
8
10
12
14
16
18
Time (PDT)
Claremnont, CA 9/09/93

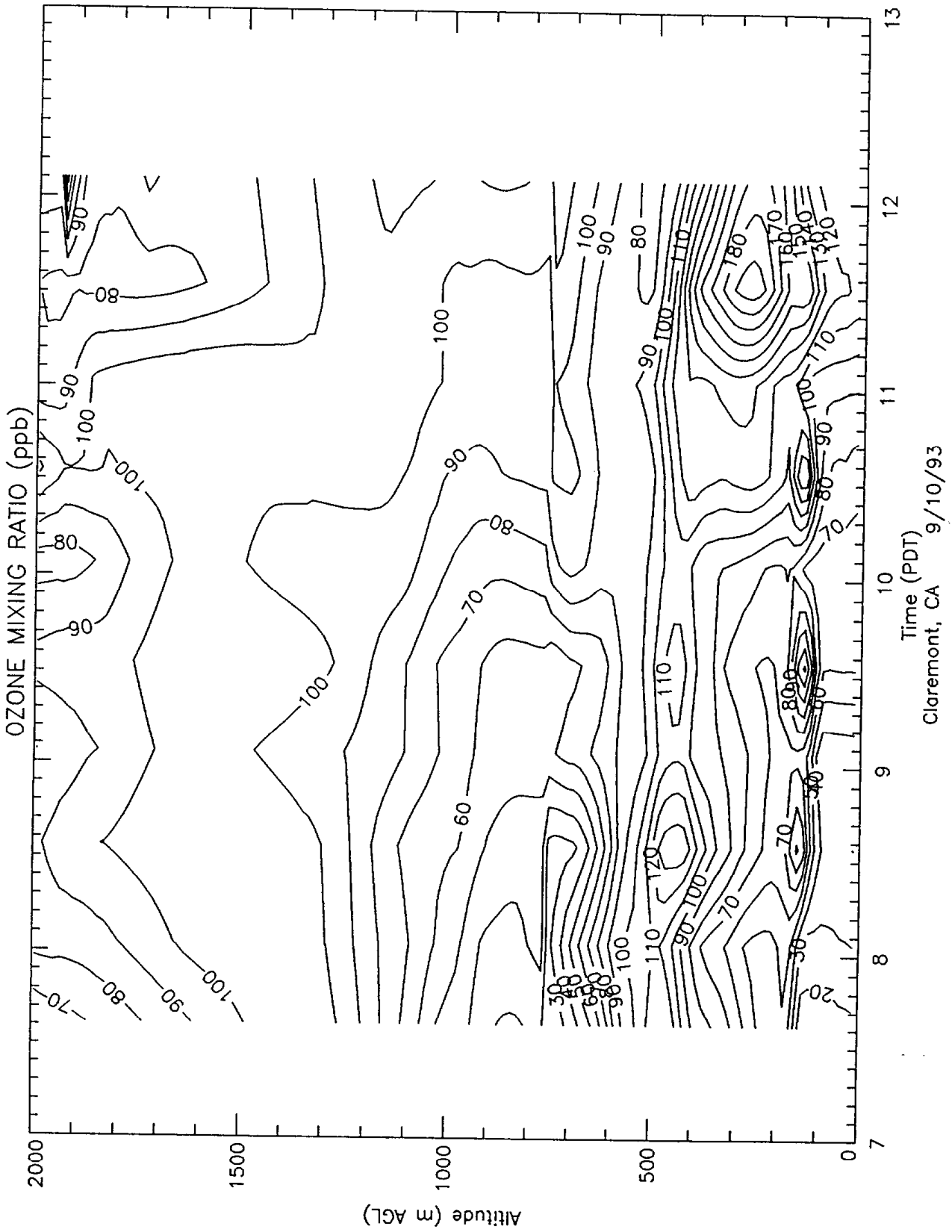
OZONE MIXING RATIO (ppb)
Altitude (m AGL)
Time (PDT)
Claremont, CA 9/10/93

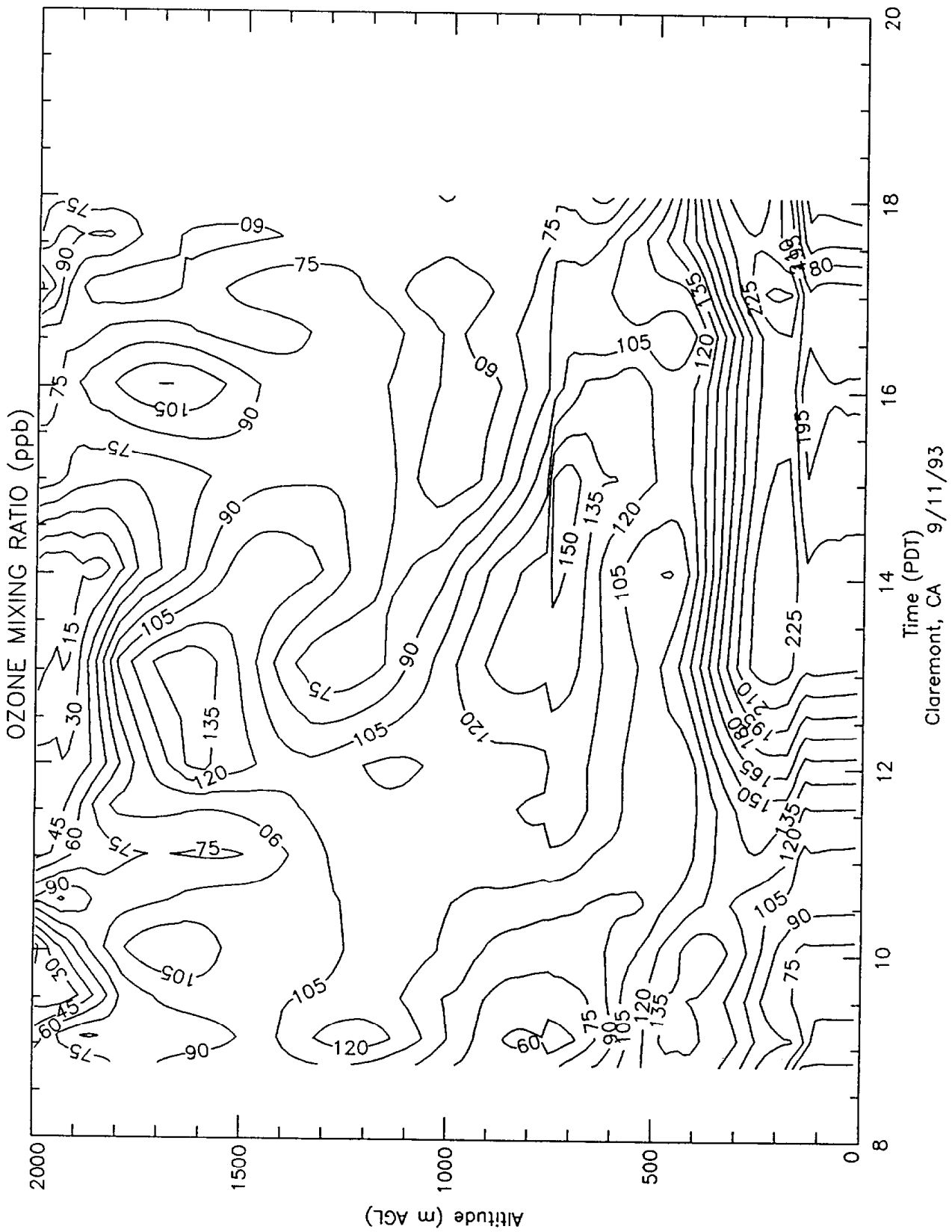
OZONE MIXING RATIO (ppb)
Altitude (m AGL)
2000
1500
1000
500
0
8
10
12
14
16
18
20
Time (PDT)
Claremont, CA 9/11/93

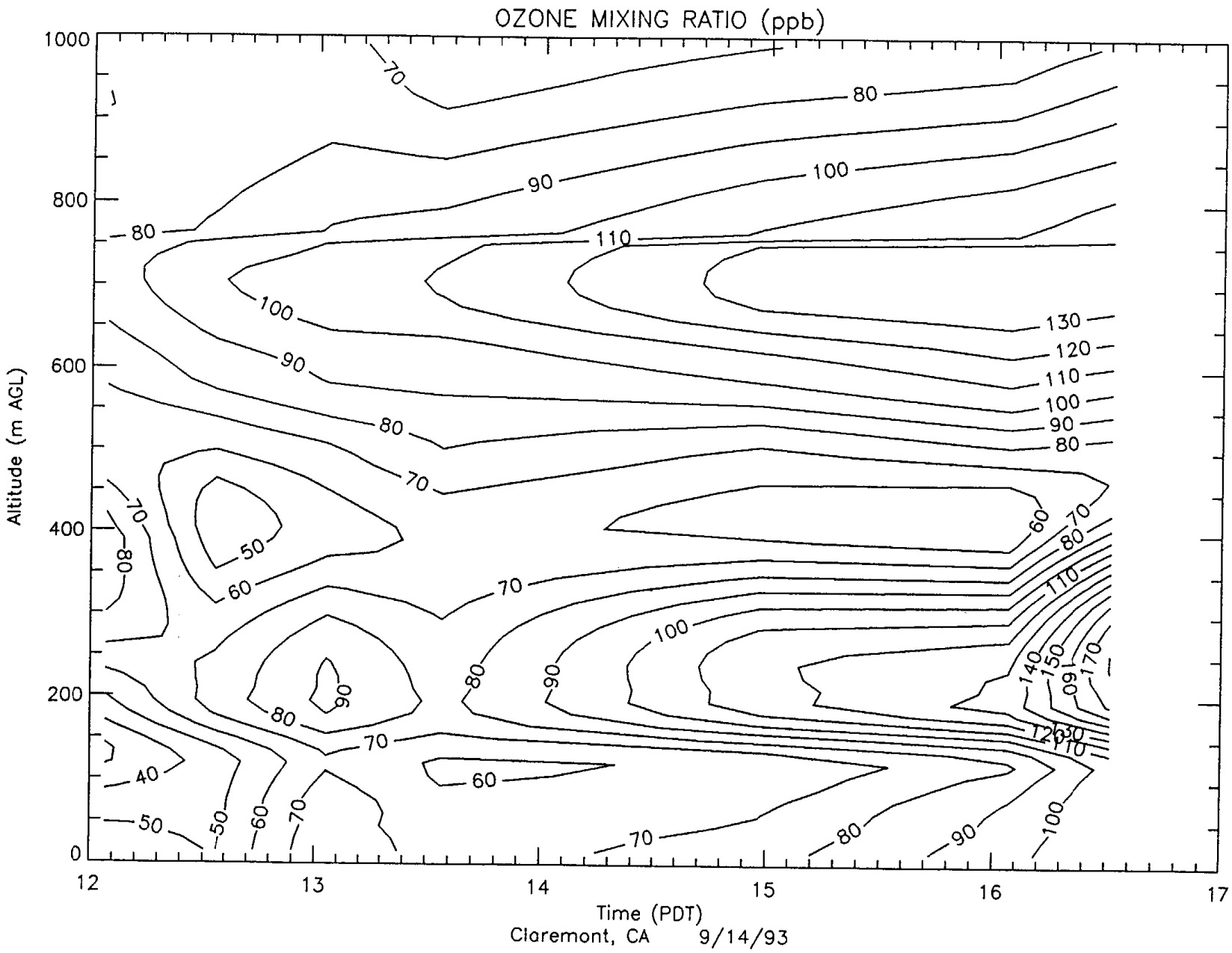
OZONE MIXING RATIO (ppb)
Altitude (m AGL)
1000
800
600
400
200
0
12
13
14
15
16
17
Time (PDT)
Claremont, CA 9/14/93

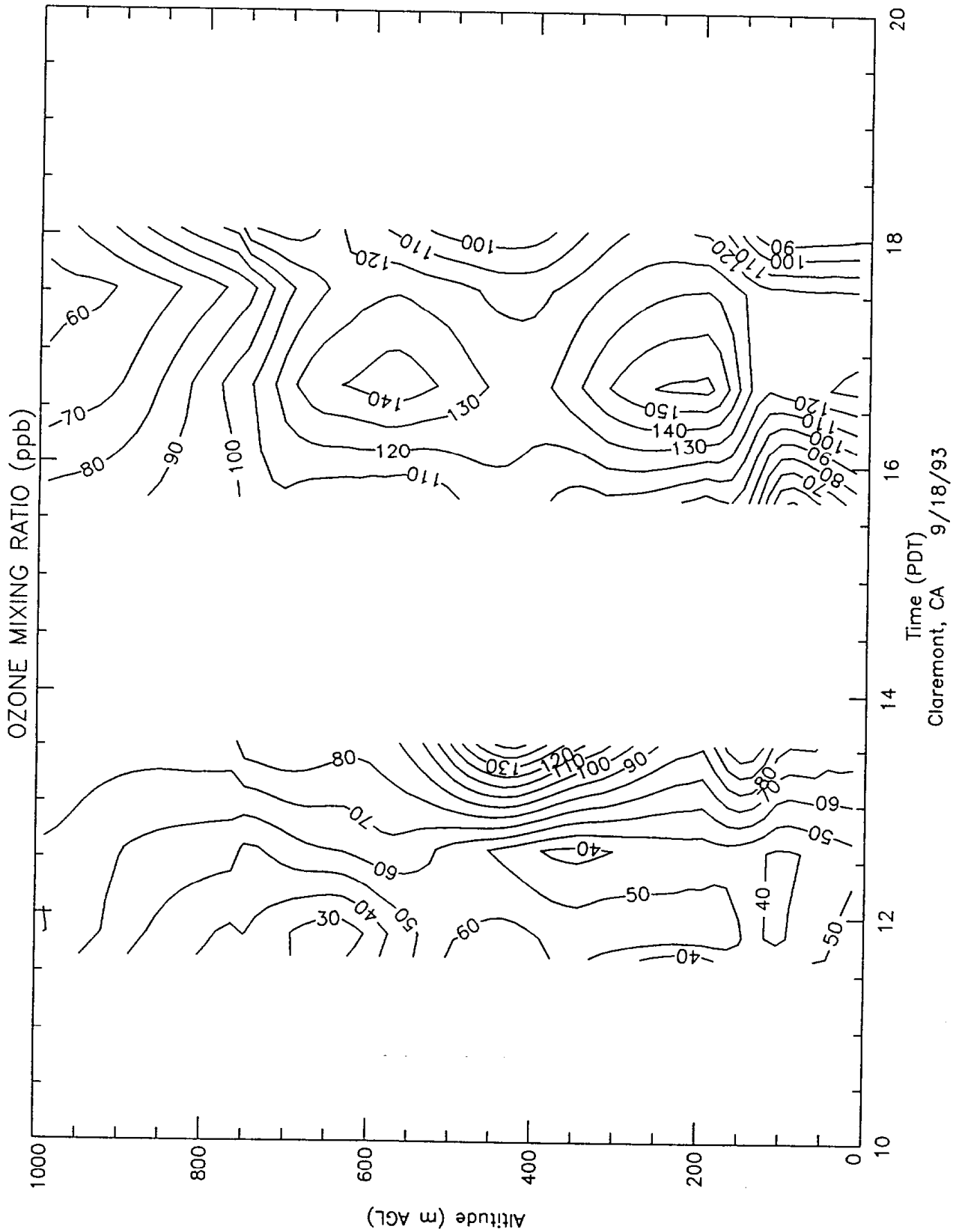
OZONE MIXING RATIO (ppb)
Altitude (m AGL)
Time (PDT)
Claremont, CA 9/18/93

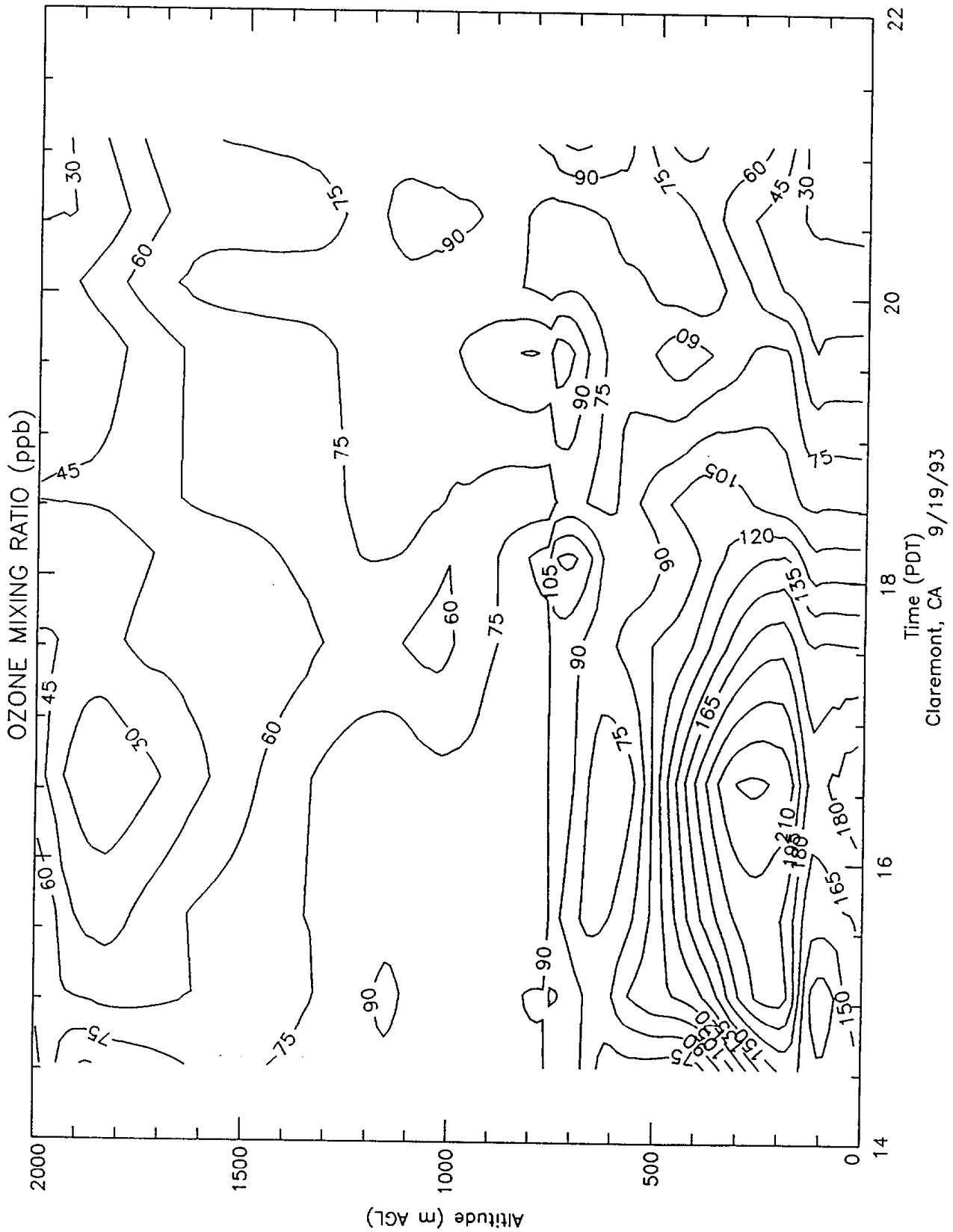
OZONE MIXING RATIO (ppb)
Altitude (m AGL)
2000
1500
1000
500
0
14
16
18
20
22
Time (PDT)
Claremont, CA 9/19/93

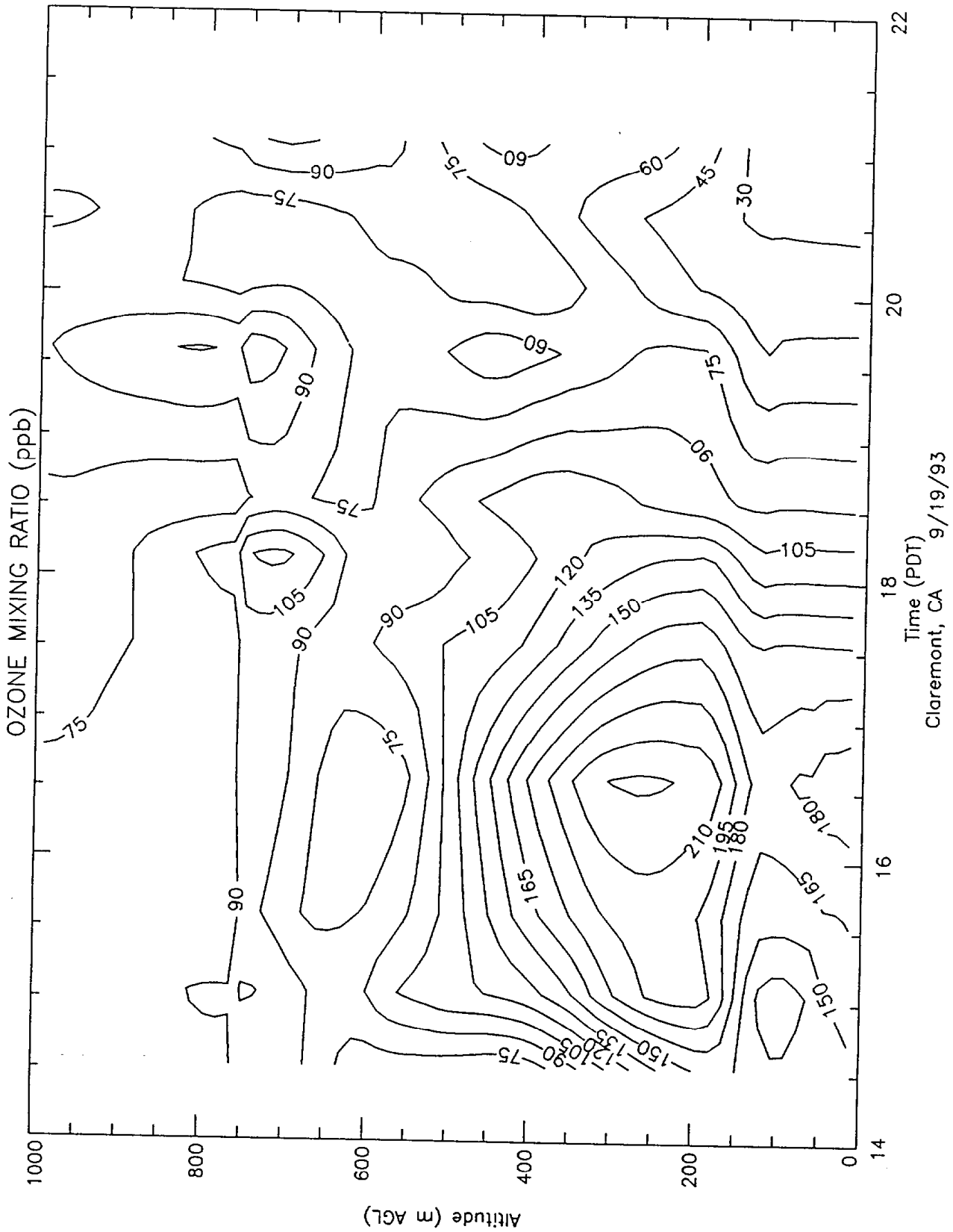
OZONE MIXING RATIO (ppb)
Altitude (m AGL)
Time (PDT)
Claremont, CA 9/19/93
1000
800
600
400
200
0
14
16
18
20
22
75
90
105
120
135
150
165
180
195
210
60
45
30